Optimising thin-film solar cells by computer simulations

Dissertation
zur Erlangung des Grades
"Doktor der Naturwissenschaften"
am Fachbereich Physik, Mathematik und Informatik
der Johannes Gutenberg-Universität in Mainz

vorgelegt von
Christian D. R. Ludwig
geboren in Frankfurt am Main

Mainz, 2011

Datum der mündlichen Prüfung: 15.6.2011

Erklärung

Hiermit versichere ich, dass ich die vorliegende Arbeit selbständig verfasst und keine anderen, als die angegebenen Quellen und Hilfsmittel benutzt habe. Alle Stellen, die dem Wortlaut oder Sinn nach anderen Werken entnommen sind, habe ich durch die Angabe der Quelle kenntlich gemacht.

Mainz, den 8. Juni 2011

Christian Ludwig

Zusammenfassung

CIGS-Dünnschichtsolarzellen verbinden hohe Effizienz mit niedrigen Kosten und sind damit eine aussichtsreiche Photovoltaik-Technologie. Das Verständnis des Absorbermaterials CIGS ist allerdings noch lückenhaft und benötigt weitere Forschung. In dieser Dissertation werden Computersimulationen vorgestellt, die erheblich zum besseren Verständnis von CIGS beitragen.

Es wurden die beiden Systeme Cu(In,Ga)Se_2 und (Cu,In,Vac)Se betrachtet. Die Gesamtenergie der Systeme wurde in Clusterentwicklungen ausgedrückt, die auf der Basis von ab initio Dichtefunktionalrechnungen erstellt wurden. Damit war es möglich Monte Carlo (MC)-Simulationen durchzuführen.

Kanonische MC-Simulationen von Cu(In,Ga)Se_2 zeigen das temperaturabhängige Verhalten der In-Ga-Verteilung. In der Nähe der Raumtemperatur findet ein Übergang von einer geordneten zu einer ungeordneten Phase statt. Unterhalb separiert das System in $CuInSe_2$ und $CuGaSe_2$. Oberhalb existiert eine gemischte Phase mit inhomogen verteilten In- und Ga-Clustern. Mit steigender Temperatur verkleinern sich die Cluster und die Homogenität nimmt zu. Bei allen Temperaturen, bis hin zur Produktionstemperatur der Solarzellen (≈ 870 K), ist In-reiches CIGS homogener als Ga-reiches CIGS.

Das (Cu,In,Vac)Se-System wurde mit kanonischen und großkanonischen MC-Simulationen untersucht. Hier findet sich für das $CuIn_5Se_8$-Teilsystem ein Übergang von einer geordneten zu einer ungeordneten Phase bei $T_0 = 279$ K.

Großkanonische Simulationen mit vorgegebenen Werten für die chemischen Potentiale von Cu und In wurden verwendet, um die Konzentrations-Landschaft und damit die sich ergebenden Stöchiometrien zu bestimmen. Stabilitätsbereiche wurden für stöchiometrisches $CuInSe_2$ und für die Defektphasen $CuIn_5Se_8$ und $CuIn_3Se_5$ bei einer Temperatur von 174 K identifiziert. Die Bereiche für die Defektphasen sind bei $T = 696$ K verschwunden.

Die Konzentrations-Landschaft reproduziert auch die leicht Cu-armen Stöchiometrien, die bei Solarzellen mit guten Effizienzen experimentell beobachtet werden. Die Simulationsergebnisse können verwendet werden, um den industriellen CIGS-Produktionsprozess besser zu verstehen und zu optimieren.

Abstract

CIGS thin-film solar cells are a promising photovoltaic technology. They provide high efficiencies at comparably low production costs. However, the knowledge about CIGS is fragmentary and more research is necessary to better understand the material. This dissertation presents computer simulations that help to improve the comprehension of CIGS.

The two systems Cu(In,Ga)Se_2 and (Cu,In,Vac)Se were considered. The total energy of the systems was expanded into the contribution of clusters and the coefficients were determined by a fit to ab initio density functional calculations. This expression for the energy was used in Monte Carlo (MC) simulations.

Canonical MC simulations of Cu(In,Ga)Se_2 reveal the In-Ga distribution for various temperatures. An order-disorder transition takes place close to room temperature. Below this, the system separates into $CuInSe_2$ and $CuGaSe_2$. Above the transition, a mixed phase exhibits clusters of In and Ga that are distributed inhomogeneously. The clusters shrink with rising temperatures and the homogeneity increases. At all considered temperatures, up to the production temperature of solar cells ($\approx$ 870 K), In-rich CIGS exhibits a greater homogeneity than Ga-rich CIGS.

The (Cu,In,Vac)Se system was studied through canonical and grand-canonical MC simulations. The $CuIn_5Se_8$ subsystem shows an order-disorder transition at $T_0 = 279$ K.

Grand-canonical simulations were performed with given values for the chemical potentials of Cu and In to calculate the concentration landscape (i.e. a map of resulting stoichiometries). Stability regions for stoichiometric $CuInSe_2$ and the defect phases $CuIn_5Se_8$ and $CuIn_3Se_5$ were determined at a temperature of $T = 174$ K. At an elevated temperature of $T = 696$ K, the regions of stable defect phases vanish.

The concentration landscape reproduces the slightly Cu-deficient stoichiometries that are experimentally observed in solar cells with good efficiencies. The simulation results can be used to better understand and optimise the industrial CIGS production process.

This thesis is based on the following publications:

1. Christian D. R. Ludwig, Thomas Gruhn, Tanja Schilling, Peter Kratzer, Claudia Felser and Johannes Windeln.

   Indium-Gallium Segregation in $CuIn_xGa_{1-x}Se_2$: An Ab Initio-Based Monte Carlo Study

   Phys. Rev. Lett. 105, 025702 (2010)

2. Christian D. R. Ludwig, Thomas Gruhn, Claudia Felser and Johannes Windeln.

   Defect structures in $CuInSe_2$: A combination of Monte Carlo simulations and density functional theory

   Phys. Rev. B 83, 174112 (2011)

Scientists play with ideas so wild that often they seem to defy common sense - and then they insist that those ideas are right, and common sense isn't.

-Terry Pratchett

Abbreviations, Units, and Constants

Å	Ångström, 10^{-10} m
β	$\frac{1}{k_B T}$
CBM	conduction band minimum
Cd	cadmium
CE	cluster expansion
CIGS	$Cu(In,Ga)Se_2$
CIS	$CuInSe_2$
Cu	copper
CVS	cross-validation score
DFT	density functional theory
E	energy or electric field
ECI	effective cluster interaction
eV	electron volt, unit of energy
η	efficiency
FF	fillfactor
FWHM	full width at half maximum
Ga	gallium
GGA	generalised gradient approximation
Γ	phase space
I	electric current
In	indium
I_{SC}	short-circuit current
K	kelvin, unit of temperature
k	electron momentum
k_B	Boltzmann constant
LDA	local density approximation
m	metre, unit of length
MC	Monte Carlo, simulation technique
Mo	molybdenum
μ	chemical potential
N	number of particles
n	electron density
n	nano, 10^{-9}

Na	sodium
Ni	nickel
NN	nearest neighbour
p	probability
Ry	Rydberg, unit of energy, 13.6056923 eV
S	entropy
S	sulphur
Se	selenium
T	temperature
T	tera, 10^{12}
TCO	transparent conductive oxide
Te	tellurium
U	(configurational) energy or voltage
U_{OC}	open-circuit voltage
V	volume
Vac	vacancy
VBM	valence band maximum
W	watt, unit of power

Contents

Chapter 1

Introduction

1.1 Motivation

At the beginning of the 21^{st} century, numerous different energy sources are used to satisfy the world's need for electricity. The biggest contributions are made by fossil fuels (coal, oil, natural gas) and uranium. Regenerative energy sources (water, wind, solar) provide ca. 15% of the electricity in Germany.

Since the reserves of fossil fuels and uranium are limited, they cannot be used forever. Furthermore, their utilisation has detrimental effects on the environment. The combustion of carbon-based fuels produces carbon dioxide and promotes global warming through the green-house effect. Nuclear fission of uranium produces radioactive waste that has to be stored securely for thousands of years. It also leads to the continuous threat of a catastrophic failure of nuclear power plants. Due to emerging industrial nations like China, the need for electricity will increase dramatically during the next decades. If mankind continues to rely on fossil fuels and uranium, it will soon be left with depleted reserves and a polluted planet.

To avoid this scenario, it is imperative to promote the usage of regenerative energy sources, like water power, wind power, and solar energy. Further sources, such as geothermal and biomass, will most likely make only a small contribution to the energy mix of the future.

Solar energy has the greatest potential of all regenerative sources. The power of global incident sunlight is about 125000 TW, whereas the global energy consumption in the year 2050 is projected to be a mere 30 TW [1]. Only a small fraction of the incident sunlight would have to be converted to electricity to satisfy global demand.

However, solar cells are still more expensive than other sources of energy. Crystalline silicon absorbers need thick layers (300 nm) to absorb the

incident light. Thin-film technologies use amorphous silicon or other materials, such as $CuInSe_2$ (chalcopyrite) or CdTe. Due to better absorption, the layer thickness can be reduced, which directly decreases the production costs. These technologies do not achieve the high conversion efficiency of crystalline silicon, but a lot of effort is being put into improving the efficiency, further decreasing the layer thickness, and transferring gained knowledge to industrial processes. However, chalcopyrites seem to be better positioned for diffuse light, whereas silicon based cells perform better under direct irradiation.

1.2 Cu(In,Ga)(S,Se)$_2$ Solar Cells

During the past years, chalcopyrites such as $Cu(In,Ga)(S,Se)_2$ (CIGS) have been shown to be promising absorber materials for thin-film solar cells with high conversion efficiencies and low production costs. These attractive prospects motivated big international companies like IBM to conduct research in the field [2, 3]. A conversion efficiency of 20.3% has been achieved on a lab scale [4] and commercial modules reach $10 - 12\%$.

For many years, our knowledge of the material has been gained almost exclusively by trial-and-error experiments. Empirical recipes for good CIGS solar cells are known, but the theoretical understanding is fragmentary. For instance, Na at the CIGS-CdS heterojunction is beneficial for cell performance, but the reason for that is not yet known.

Today, there is a growing interest in investigating the properties of the material through computer simulation and theoretical methods. The goal is to achieve a fundamental understanding of the material. This knowledge can then be used in several ways.

Firstly, with comprehensive knowledge of the processes that take place in a CIGS solar cell, one can identify those properties that have to be optimised to achieve greater efficiency. More importantly, it is possible to find ways to optimise these properties without changing others that need to be kept constant. In computer simulations, parameters can be controlled independently, whereas in experiments, the parameters are hardly ever independent from each other.

Secondly, comprehensive knowledge enables us to find substitutes for materials that need to be replaced. One example for such a material is CdS. This is used as a buffer layer in the CIGS solar cell, but Cd is toxic and its use will certainly soon be prohibited. All efforts to find a suitable replacement have failed up to now because it is not understood why CdS is such a good buffer material.

This thesis presents computer simulation studies of CIGS absorber material are presented. A combination of Monte Carlo simulations and ab initio density functional electronic structure calculations is used to investigate structural properties. The connection between the two methods is made by a cluster expansion of the configurational energy. The results are interpreted with a focus on the implications for industrial CIGS solar cell production processes.

The first theoretical investigation of chalcopyrite semiconductors was published by Jaffe and Zunger in 1983 [5]. They calculated lattice parameters, tetragonal distortions, anion displacements and band-structures of $CuGaS_2$, $CuInS_2$, $CuGaSe_2$, and $CuInSe_2$. Their paper established the foundations for all subsequent computer simulations of CIGS material, but it took a while for computational studies to gain momentum.

In 1992, Wei, Ferreira, and Zunger used ab initio electronic structure calculations, the cluster expansion technique, and Monte Carlo simulations to calculate the order-disorder transition temperature for $CuInSe_2$ [6]. Their results agree well with experiments and prove that this particular combination of methods can accurately describe the complex behaviour of solids.

In the mid-1990s, the simulations were extended beyond the absorber material. Wei, Zhang, and Zunger looked at the $CuInSe_2$/CdS heterojunction of CIGS solar cells [7]. They calculated the band offsets for this essential part of the cell. Subsequently, Wei and Zunger added the investigation of optical bowing parameters [8]. In 2005, Gloeckler and Sites found in numerical studies that band gap grading can have a beneficial effect on the solar cell [9].

In 1997 and 1998, Zhang, Wei, and Zunger published fundamental papers on defects in $CuInSe_2$ [10, 11]. They contain the calculation of defect levels and formation energies of defect complexes. The defect complex $2Vac_{Cu} + In_{Cu}$ is found to have an exceptionally low formation energy and to stabilise the Cu-poor $CuIn_5Se_8$ material. A subsequent study by the same authors focused on the influence of Na on the electrical and structural properties of $CuInSe_2$ [12].

In 1998, Wei, Zhang, and Zunger dealt with the issue of Ga addition to $CuInSe_2$ [13], providing a comprehensive picture of how Ga influences the band gap. The topic was recently revisited and extended by Huang [14]. He used computer simulations to show that a band gap of 1.5 eV should lead to the greatest efficiency and explains why record efficiency CIGS solar cells have a much lower band gap of about 1.15 eV. The reason is that the open-circuit voltage does not increase with increasing Ga content above a gap of 1.15 eV.

After the year 2000, the interest in defects increased and more phenomena were studied. Jaffe and Zunger investigated how a surface reconstruction in chalcopyrite semiconductors leads to the polar (112) surface being more stable than nonpolar surfaces [15]. Their prediction is today's predominant opinion amongst experts in the field. Subsequently, Lany and Zunger investigated the influence of anion vacancies on photoconductivity, a crucial factor for solar cell performance [16].

A crucial question for all semiconductor material is: how can it be doped? This question is of course closely related to the question of defects. CIGS is intrinsically p-type. Persson et al. explain why $CuInSe_2$ can readily be doped n-type, and $CuGaSe_2$ cannot [17].

The fact that the absorber material of high-efficiency solar cells is Cu-poor and In-rich has led to a recent interest in Cu-poor phases, such as $CuIn_3Se_5$ or $CuIn_5Se_8$. These phases are suspected of playing a role at the CIGS/CdS interface. Chang et al. calculated several low-energy structures for the 1-3-5 and 1-5-8 stoichiometries and compared their simulation results with X-ray absorption data [18]. They find experimental evidence that $CuIn_3Se_5$ can best be described by structures containing 20% ($2\,\mathrm{Cu} + 2\,\mathrm{In}$) tetrahedra and 40% each of ($\mathrm{Vac_{Cu}} + \mathrm{Cu} + 2\,\mathrm{In}$) and ($\mathrm{Vac_{Cu}} + 3\,\mathrm{In}$) tetrahedra. This is consistent with the suggestions of Zhang, Wei, and Zunger [11].

Lately, a lot of studies have been dedicated to grain boundaries. They seem to be important for good solar cells, because cells made from monocrystalline CIGS perform less well than polycrystalline cells [19]. In 2005, Gloeckler et al. studied the recombination of charge carriers at grain boundaries with two-dimensional simulations [20]. Based on their calculations, they explain how record efficiencies of 20% are possible despite the abundant presence of grain boundaries in CIGS.

An important step towards cheaper solar cells would be the replacement of In and Ga by cheaper materials. In 2005, Raulot, Domain, and Guillemoles studied potential In- and Ga-free absorbers with ab initio methods [21]. They investigated In-isoelectric couples, such as (Zn,Sn), and explored the most important point defects and defect complexes. Compounds such as $Cu_2ZnSnSe_4$ exhibit striking similarities to $CuInSe_2$.

All the aforementioned studies focused on limited aspects of the solar cell. The complete description of a cell through ab initio methods is not feasible, but there are device simulators that can predict the approximate behaviour of solar cells. For instance, Bouloufa, Djessas, and Zegadi used this type of simulator to determine key parameters such as U_{OC} or I_{SC} [22], for CIGS with an In_2S_3 buffer layer.

Of course, there are limits to the optimisation efforts. The efficiency of solar cells is limited first and foremost by the Carnot-efficiency, but also

by other factors that were investigated by Werner, Mattheis, and Rau in 2005 [23]. They conclude that for an increase in efficiency above 20%, it will be necessary to focus on decreasing electronic inhomogeneities. The upper efficiency limit of 33% for an ideal black body cell with infinitely large mobility and only radiative recombination [23] is still far away.

1.3 Numerical Methods for Studying CIGS

1.3.1 Computational Materials Science

The term "computational materials science" was coined to describe the process of developing new materials, not in a laboratory, but with numerical calculations and theoretical studies. The advantages are numerous.

First of all, candidate materials do not have to be synthesised. This saves money for expensive elements, but also a lot of time. It becomes unnecessary to find good synthesis recipes and temper and characterise the samples, only to find out that the compound does not have the desired properties. Computer simulations make it possible to scan hundreds of compounds for their suitability. One example for this type of investigation is the study of the band gaps and lattice parameters of 648 half-Heusler compounds with the objective of finding a suitable buffer material for CIGS solar cells [24].

Beside the abovementioned advantage of not having to synthesise a material in computer simulations, one has perfect control over all parameters. Stoichiometry, lattice constants, atomic positions, interaction potentials, and many more can be varied independently. This allows a highly systematic approach to materials science. The influence of variations can be observed directly and very accurately. Certain types of defects can be completely excluded from or specifically introduced into the material. The stoichiometry can be adjusted perfectly. Even contributions to the interaction energy such as spin-orbit coupling can be switched on and off at will.

Additionally, the theoretical approach to materials science allows the investigation of compounds in unlikely or even unphysical regions of phase space. These compounds might not occur in nature or might not be producable in the lab, but their investigation can help to gain fundamental understanding. For instance, it is possible to displace an atom in a crystal and calculate the resulting force.

In the following, some examples are given to illustrate the work that has been done in the field of computational materials science. The focus is on contributions of IBM, who supported this thesis.

One incentive for studies in the field of condensed matter was and still is the investigation and development of materials for the next generation of IBM computers. Even though the semiconductor technology is still largly based on silicon, many other semiconducting elements and compounds are used nowadays (e.g. Ge, GaAs, AlN, ZnO, CdTe, just to name a few). The combinatorial possibilities are endless and many compounds have desirable properties.

An early example for the investigation of a semiconductor heterostructure by IBM is the work of Andreoni, Baldereschi, and Car from the year 1978 on GaAs–AlAs [25]. They performed electronic structure calculations to study the effects of cation order in GaAs–AlAs heterostructures. It should be mentioned that both, ordering of elements and heterojunctions between different semiconductor materials, are important in CIGS solar cells.

Further examples for condensed matter studies by IBM are the calculation of self-diffusion constants in silicon [26] and the determination of the Al-Li interaction in organic light-emitting diodes by means of molecular dynamics [27].

A very hot topic that was acknowledged with the Nobel Prize in Physics in 2010 is graphene. These planar sheets of carbon with a thickness of only one atom motivated computational studies at the IBM Thomas J. Watson Research Center in Yorktown Heights, New York [28, 29].

Some investigations of IBM go beyond condensed matter systems. For instance, a study with relevance more towards engineering dealt with the numerical simulation of aircraft wakes at high Reynolds numbers [30]. And other studies, residing in the field of biophysics, deal with fullerenes (C_{60} molecules) and their derivatives [31].

One basic question in materials science, which is also relevant for the fullerene studies, is: which crystal structures of a material with a given stoichiometry are possible? Experimentally, the answer to that question may depend on the sample preparation process. Different approaches could lead to different crystal structures. Computer simulations can give the total energy of all possible structures and thus find the ground state.

The computational effort for simulations can be very high, depending on the degrees of freedom and the number of atoms involved. Fast computers are essential for this task. A lot of different machines are available and only a few can be highlighted here.

The IBM System p series (e.g. IBM System p5 590) is based on POWER architecture. Its strengths are dynamic logical partitioning and micro-partitioning, which means that hardware ressources (CPUs and memory) can be reallocated while the machine is up and running. It is possible to create partitions with any amount of memory, which makes the p series suit-

able for memory-intensive calculations. A SuSE linux operating system can be installed to enable the compilation of established electronic structure calculation software packages. A p590 was used for the ABINIT calculations in this thesis.

The flagship of IBM is the Blue Gene series. Blue Gene machines are regularly ranked at the top of the TOP500 list of supercomputers. They provide a huge number of processors for massively parallelised calculations. However, the amount of memory per processor is limited. For this reason, Blue Gene machines are best suited for the electronic structure calculation of a large number of k-points (in the case of k-point parallelisation, e.g. one k-point per core) or a large number of atoms (in the case of parallelisation over atoms, e.g. one atom per core). A Blue Gene/p was used for the PWSCFcalculations in this thesis.

The requirements for calculations can be very different. A modular architecture has the advantage that it can be adapted to the specific needs. One such modular architecture is the IBM BladeCenter. Arbitrary numbers of blades can be combined in racks to form an integrated supercomputer that fits exactly the specified needs and budget.

It is very expensive to purchase and operate a supercomputer. Cooperation between universities and industry can help to make such machines available to the scientists who need them. For instance, the Johannes Gutenberg university was awarded the IBM Shared University Research Grant in 2010, consisting of a BladeCenter that is now used in the field of computational materials science.

Another noteworthy cooperation is the development of the Car-Parrinello molecular dynamics (CPMD) programme by IBM and the MPI Stuttgart. Programming a reliable and accurate electronic structure software costs a lot of time and money. For the development of a programme that is optimised for a certain computer type, a profound knowledge of that computer type is necessary. CPMD is an established standard programme for molecular dynamics simulations that is optimised for massive parallelisation and Blue Gene machines. It is used not only by IBM and the MPI Stuttgart, but all over the world.

1.3.2 Tools of Computational Materials Science

All computer programmes in materials science use one of two different approaches: they either make use of variable, experimentally determined input parameters or they do not do so. Nowadays, practically all simulations of solids and molecules are undertaken from first principles (ab initio). This

means that the Schrödinger equation is solved without making use of variable parameters which influence the result of the calculation.

Tool: Density Functional Theory

The year 1964 was the beginning of a new era for computational materials science, as Hohenberg and Kohn published their paper on density functional theory (DFT) [32]. Their theorems made it possible to treat complex systems with a functional that depends only on the electron density and not on the positions and momenta of all electrons individually. For the development of DFT, Walter Kohn was awarded the Nobel Prize for Chemistry in 1998.

DFT tells us that a universal functional of the electron density exists, but not how it looks. In 1965, Kohn and Sham developed a method of approximating the functional and solving the Schrödinger equation in a rigorous, self-consistent way [33]. Their method is the basis for all current DFT computer programmes.

Tool: Monte Carlo Simulations

The electronic properties of a system can be predicted by DFT, but the computational cost of studying a large system with more than a couple of 100 atoms is immense and makes such studies very time-consuming or even impossible. For the investigation of large systems and great length scales, as is necessary for homogeneity studies, other methods have to be used.

The Monte Carlo (MC) method can be utilised to treat systems with thousands of atoms. The term was introduced by John von Neumann, in reference to the Monte Carlo casinos, because of the random nature of the method. One special kind of MC simulation samples the phase space of a system by randomly exchanging particles in the simulation volume. These particles can for instance be atoms, colloids, or spins.

Metropolis et al. invented a criterion that ensures that the ensemble follows a Boltzmann distribution [34]. The exchanges are accepted with a probability that depends on the energy difference between the configurations (before and after the exchange) and the temperature.

Tool: Cluster Expansions

MC simulations are widely used in the fields of soft matter and solids. The combination with ab initio electronic structure calculations is problematic as the energy calculations for the configurations before and after the exchange

are very time consuming. An ab initio energy calculation at every MC step is impossible.

A way around this problem is the cluster expansion (CE) technique [35, 36]. The total energy of a configuration is expanded into contributions of cluster figures. The coefficients of this expansion are determined by a fit to the energies of a small number of configurations. These configurations contain only a few atoms and have to be calculated ab initio. The expansion can then be used to calculate the total energies of arbitrary configurations in MC simulations.

In addition to configurational energy, other energy contributions may be relevant. Volume deformation and relaxation of atomic positions and lattice parameters contribute to the total energy [37] and have to be included in the CE if they cannot be neglected.

1.3.3 Investigating Structure and Homogeneity

Of all the endless possibilities that computational materials science offers, two will be highlighted in the following: i) finding the ground state crystal structure of a compound and ii) investigating the homogeneity of a material.

i) When dealing with new compounds, at first, the crystal structure has to be determined. Only if the symmetry of the structure is known, properties can be calculated and experimental data can be interpreted accurately. The crystal structure of an arbitrary combination of elements is a priori unknown. Furthermore, multiple crystal structures could be possible, depending on temperature, pressure, or other parameters.

The task becomes a lot easier if the search is restricted to ground states on a predefined lattice. Now only the distribution of the atoms on the lattice sites has to be considered.

The CE method can be used to find the ground state configuration. After the creation of the CE, the total energy of all possible configurations can be calculated. The ground state is the structure with the lowest energy. Other configurations with comparably low energies could be relevant at finite temperatures.

ii) The homogeneity of a material is a crucial parameter in many applications. One example is multinary absorber materials for solar cells. Only a homogeneous material has a constant band gap. Inhomogeneities lead to band gap fluctuations that decrease cell efficiency [23]. Other areas in which homogeneity is important include thermoelectrics, batteries, micro- and nanoelectronics, and many others.

Materials in batteries need to be homogeneous, because the capacity of NiCd batteries is decreased through the crystallisation of the constituents.

On the other hand, in thermoelectrics, a certain degree of inhomogeneity is desirable to minimise the phonon conductivity.

Homogeneity studies can be performed with MC simulation. It is possible to identify clusters of atoms, regular patterns, and regions with an excess of one atomic species. The time-consuming part of these MC simulations is the energy calculation, for which a CE can be used.

A limiting factor for this kind of investigation is the number of participating species. To this day, most studies considered two atom types and only a few considered three. The calculation of CIGS properties, taking into account Cu, In, Ga, Se, S, vacancies and doping with Na, Cd, and others is not feasible. The corresponding CE would need a large number of cluster figures and a forbidingly great number of huge ab initio calculations.

The structure of the thesis is as follows:

Chapter 2 explains the theoretical concepts that have been used throughout this thesis. It covers DFT, MC simulations, and the CE formalism, in addition to a description of solar cells in general and CIGS cells in particular.

Chapter 3 introduces the software that has been used. This includes the ab initio electronic structure programmes ABINIT and QUANTUM ESPRESSO, the programme package ATAT for the creation of CEs, and the MC code written in C++.

Chapter 4 includes the results of all simulations that have been performed. The focus is on the MC simulations of two different systems: $Cu(In,Ga)Se_2$ and (Cu,In,Vac)Se.

Chapter 5 provides a summary of this thesis and illustrates the relevance of the results for industry. Additionally, an outlook is given on what needs to be undertaken in the future to achieve a greater efficiency of thin-film solar cells.

Chapter 2

Theory

2.1 The Working Principle of Solar Cells

A photovoltaic cell (solar cell) is a device that creates electrical power from sunlight. Figure 2.1 shows a schematic overview. Like in a photo-diode, a p-n junction is used to create a space charge region and thus an electric field E. When sunlight is absorbed and creates electron-hole pairs, the electric field separates the charges and drives the electrons to the anode and the holes to the cathode. The result is a current I.

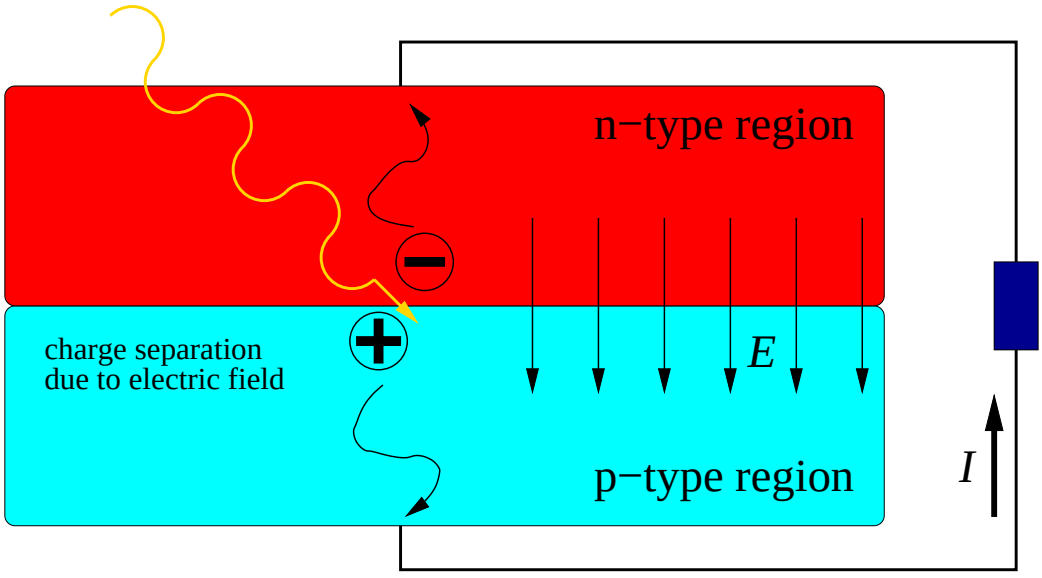

Figure 2.1: The working principle of a solar cell.

2.2 Structure of Cu(In,Ga)(S,Se)$_2$ Solar Cells

CIGS is the leading technology for thin-film solar cells. It reaches high efficiencies of over 20% [4] and has the potential to become cheaper than silicon-based photovoltaic technology. In this section, the structure and the properties of CIGS thin-film solar cells will be discussed in detail.

The CIGS solar cell is made of several layers as can be seen in Figure 2.2. Sunlight is absorbed in the CIGS layer. The overall Cu content of high-efficiency absorber material is usually lower than stoichiometric and the In:Ga ratio is 7:3. Ga increases the band gap, leading to better utilisation of the solar spectrum, but too much Ga is detrimental [13, 14]. A contribution to this effect is discussed in Section 4.1.

CIGS can be grown monocrystalline [19], but polycrystalline absorbers yield more efficient cells. This shows that a certain amount of grain boundaries and defects is crucial for cell operation [20, 38]. Results of defect simulations with a focus on Cu-poor structures are presented in Section 2.3.

The absorber of CIGS solar cells is grown on a layer of Mo. This layer creates a good bonding to the glass substrate and serves as the back side electric contact. It also serves as a diffusion barrier that controls the diffusion of elements from the glass into the absorber.

The front side electric contact is formed by a transparent conductive oxide (TCO), usually ZnO. Obviously, it needs to be transparent to allow the sunlight to reach the absorber and has to be a good conductor to minimise ohmic losses.

A buffer layer aligns the conduction band minimum (CBM) of the TCO and the absorber. A substantial misalignment of the two reduces the solar cell performance [39]. The most efficient CIGS cells use CdS as a buffer material.

The interface between the CdS buffer layer and the CIGS absorber is of particular importance [7, 40]. It forms the p-n junction of the solar cell. Despite its importance, knowledge about the interface is fragmentary and mostly qualitative. It is known that Na at the interface increases the solar cell efficiency [12], but the reason for this is unknown. The glass substrate usually contains Na which diffuses through the Mo and CIGS layers to the CdS–CIGS interface. It is also known that the CIGS at the interface to CdS is Cu-poor or even Cu-free [41, 42], but the structure of this Cu-poor CIGS is unknown. Finally, it is suspected that Cd diffuses from the CdS into the CIGS, but this hypothesis could not yet be proven.

Computer simulation can shed light on these open questions. Cd and Na diffusion can be investigated with ab initio molecular dynamics simulations

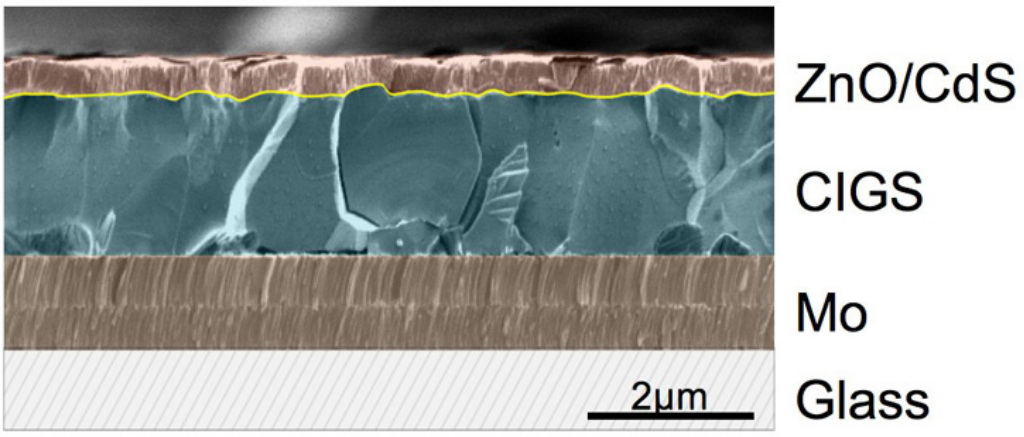

Figure 2.2: Scanning electron microscope image of a CIGS solar cell (source: Helmholtz-Zentrum für Materialien und Energie, Berlin). The different layers are clearly distinguishable, as are the grains in the CIGS layer.

and static calculations can find Cu-poor structures that are candidates for the Cu-poor CIGS at the interface.

2.3 $CuInSe_2$ and Defects

$CuInSe_2$ (CIS) crystallises in the chalcopyrite space group 122 with symmetry $I\bar{4}2d$ [5, 43]. Cu occupies the lattice sites $4a$, In $4b$, and Se $8d$. Figure 2.3 displays the tetragonal unit cell and Table 2.1 lists the positions of all atoms. The tetragonal unit cell has 16 symmetry operations, whereas the primitive cell has 8.

Ga is added to the system to increase the band gap [13, 14]. It replaces parts of the In on lattice site $4b$ ($CuIn_xGa_{1-x}Se_2$). The distribution of In and Ga on the four $4b$ sites is random. The sites are still equivalent and the symmetry is not changed. The addition of S leads to S and Se sharing the lattice site $8d$ in a similar way. For the sake of simplicity, the following discussion will focus on CIS.

$CuInSe_2$ is a direct semiconductor with a band gap of 1.0 eV [5]. The experimental lattice parameters are $a = 0.57840$ nm for the two short axes and $c = 1.16142$ nm for the long axis [43]. The tetragonal distortion is thus $\frac{c}{2a} = 1.004$.

The Se atoms are closer to the Cu atoms than to the In atoms. This is due to the larger size of In compared to Cu. The displacement is characterised by the anion displacement parameter x. It is equal to the first reduced

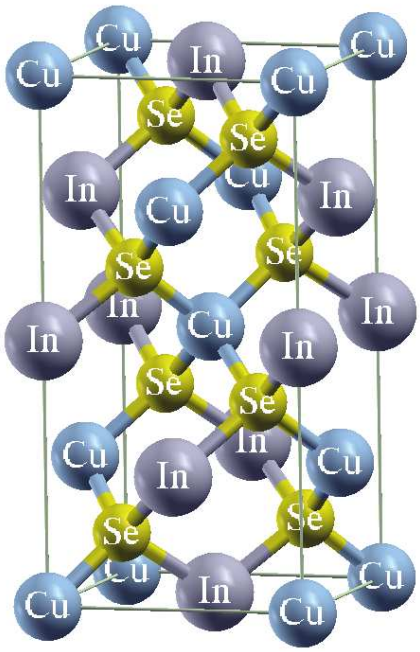

Figure 2.3: Tetragonal unit cell of $CuInSe_2$

coordinate of the Se closest to the origin $(x, 0.25, 0.125)$. The positions of the other Se atoms are determined through symmetry. The experimental value for the displacement is $x = 0.224$ [43] for $CuInSe_2$, where a value of $x = 0.25$ would corresponds to a central position between Cu and In.

The anion displacement and tetragonal distortion are free parameters in the space group 122. These can be varied without changing the symmetry. The values for $CuInSe_2$ are given above, but those values change with the addition of Ga and S. For instance, $CuGaSe_2$ has a tetragonal distortion of 0.9825 and an anion displacement of 0.250 [43]. Furthermore, the lattice parameter a is reduced to 0.56140 nm and the band gap is 1.7 eV [5].

Investigations of the CdS–CIS interface indicate that CIS close to the interface has a $CuIn_3Se_5$ stoichiometry [44]. This observation can be explained by a $CuIn_3Se_5$ surface phase with a thickness of some unit cells. However, recent results by Souilah et al. from the year 2010 point towards a continuous evolution of the stoichiometry without distinct phases [45]. Other experiments and calculations suggest that the Cu-poor region at the interface is a very thin, completely Cu-depleted surface reconstruction [15, 41, 46, 47]. The true nature of the Cu-poor region is still unclear and a subject for debate. Cu depletion can also be observed at grain boundaries in the bulk material of CIGS [38].

Table 2.1: Positions of all atoms in the tetragonal unit cell of $CuInSe_2$, given in reduced coordinates. Cartesian coordinates are retrieved by multiplying the reduced coordinates with the lattice constants. x is the anion displacement parameter.

Element	Reduced coordinates	
Cu	$(0,\ 0,\ 0)$,	$(0.5,\ 0.5,\ 0.5)$,
	$(0,\ 0.5,\ 0.25)$,	$(0.5,\ 0,\ 0.75)$
In	$(0.5,\ 0.5,\ 0)$,	$(0,\ 0,\ 0.5)$,
	$(0,\ 0.5,\ 0.75)$,	$(0.5,\ 0,\ 0.25)$
Se	$(x,\ 0.25,\ 0.125)$,	$(1-x,\ 0.75,\ 0.125)$,
	$(0.25,\ 0.5+x,\ 0.375)$,	$(0.75,\ 0.5-x,\ 0.375)$
	$(0.25,\ 1-x,\ 0.875)$,	$(0.75,\ x,\ 0.875)$,
	$(0.5-x,\ 0.25,\ 0.625)$,	$(0.5+x,\ 0.75,\ 0.625)$

The observation of Cu-poor CIS has raised a lot of interest. The most significant theoretical studies were published by Zhang, Wei, and Zunger in 1997 and 1998 [10, 11] who investigated defect levels and formation energies of defect complexes in $CuInSe_2$. The building block for the considered defect compounds is the defect complex $2Vac_{Cu} + In_{Cu}$. It consists of two Cu vacancies and one In on a Cu site. The complex has an exceptionally low formation energy. By adding j defect complexes to i $CuInSe_2$ unit cells, all stoichiometries along the Cu_2Se–In_2Se_3 tie-line are accessible. For instance, $i = 1$, $j = 1$ leads to $CuIn_5Se_8$ and $i = 5$, $j = 4$ leads to $CuIn_3Se_5$. The structures can be described by a weighted distribution of three different types of local tetrahedra around the Se atoms: 2 Cu + 2 In (denoted as $k = 8$), Vac_{Cu} + Cu + 2 In ($k = 7$), and Vac_{Cu} + 3 In ($k = 9$). Here, k is the sum of valence electrons of nearest neighbour cations around Se. $CuIn_3Se_5$ can be described as having 20% of $k = 8$ and 40% each of $k = 7$ and $k = 9$ clusters, $CuIn_5Se_8$ has 50% $k = 7$ and 50% $k = 9$ clusters.

$CuIn_3Se_5$ and $CuIn_5Se_8$ are the two stoichiometries on the Cu_2Se–In_2Se_3 tie-line that have been investigated most frequently. A great number of experiments have been performed to find their ground state structures under normal conditions. Most of them find that Cu-poor CIS forms a stannite structure with $I\bar{4}2m$ symmetry [48–54]. This structure features the same lattice positions as the chalcopyrite structure, but the occupation of lattice sites is different. However, some experiments come to different conclusions, including thiogallate (for $CuIn_3Se_5$) and hexagonal (for $CuIn_3Se_5$ and $CuIn_5Se_8$) lattices [55–57]. Obviously, the observed structure depends on the

sample preparation and measurement technique. Computer simulation can shed light on this issue due to the perfect control over all parameters.

2.4 Density Functional Theory

Density functional theory (DFT) [32] is a method that can be applied to calculate the electronic properties of solids. It is very popular in computational materials science due to its accuracy and simplicity.

To solve a quantum mechanical problem, it is necessary to solve the Schrödinger equation $\hat{H}\Psi = E\Psi$. All electronic structure methods apply the Born-Oppenheimer approximation [58] to simplify the problem. In this approximation, the location of the nuclei is kept fixed while the electronic Schrödinger equation is solved. This is an acceptable simplification because the electrons are more than a thousand times lighter and thus much faster than the nuclei. They respond almost instantly to any change of the atomic positions. The Schrödinger equation can then be written as

$$\begin{aligned} \hat{H}\Psi(\mathbf{r}, \mathbf{r}_2, \mathbf{r}_3, ..., \mathbf{r}_N) &= [\hat{T}_e + \hat{V}_{eN} + \hat{V}_{ee}]\Psi(\mathbf{r}, \mathbf{r}_2, \mathbf{r}_3, ..., \mathbf{r}_N) \\ &= E\Psi(\mathbf{r}, \mathbf{r}_2, \mathbf{r}_3, ..., \mathbf{r}_N), \end{aligned} \tag{2.1}$$

with the kinetic energy of the electrons $\hat{T}_e$, the Coulomb interaction between electrons and nuclei $\hat{V}_{eN}$, and the electron-electron interaction $\hat{V}_{ee}$. $\hat{\Psi}$ is the stationary electronic wave function and N the number of electrons.

The central quantity in DFT is the electron density

$$n(\mathbf{r}) = N \int \mathrm{d}\mathbf{r}_2 \int \mathrm{d}\mathbf{r}_3 \ \ldots \int \mathrm{d}\mathbf{r}_N \ |\Psi(\mathbf{r}, \mathbf{r}_2, \mathbf{r}_3, ..., \mathbf{r}_N)|^2, \tag{2.2}$$

which is much easier to handle than the full many-body wave function.

2.4.1 Hohenberg-Kohn Theorems

Hohenberg and Kohn proved two important theorems [32].

1. The ground state electronic density $n_0(\mathbf{r})$ of an electronic system is a unique functional of the external potential $v(\mathbf{r})$.

2. For a given electronic system, the lowest energy is obtained with the ground state electronic density $n_0(\mathbf{r})$. Minimising $E[n(\mathbf{r})]$ with respect to $n(\mathbf{r})$ yields $n_0(\mathbf{r})$, which can be used to obtain all properties of the system.

The external potential $v(\mathbf{r})$ includes the effect of the nuclei on the electrons. Hohenberg and Kohn also derived the general form of the functional which will be discussed in Section 2.4.3.

2.4.2 Kohn-Sham Equations

In 1965, Kohn and Sham developed a self-consistent scheme to solve the Schrödinger equation [33]. They replaced the system of interacting electrons by a system of non-interacting quasi-particles in an effective potential $\hat{v}_{eff}$, which includes all quantum mechanical many-body interactions. This leads to a set of single particle equations of the form

$$[-\frac{1}{2m}\nabla^2 + \hat{v}_{eff}(\mathbf{r})]\ \ \psi_i(\mathbf{r}) = \varepsilon_i\ \ \psi_i(\mathbf{r}). \tag{2.3}$$

$\psi_i(\mathbf{r})$ are the wave functions of the non-interacting quasi-particles and ε_i the corresponding energies. The effective potential is given by

$$v_{eff}(\mathbf{r}) = v_{eN} + \int \frac{n(\mathbf{r}')}{|\mathbf{r} - \mathbf{r}'|}\mathrm{d}\mathbf{r}' + v_{\mathrm{XC}}(\mathbf{r}). \tag{2.4}$$

The first term is the previously mentioned electron-nuclei interaction. The second term is the Hartree potential which is the mean-field Coulomb interaction of a single electron with the charge of all other electrons. The last term is the exchange-correlation potential. It includes all many-body interactions, such as exchange interaction and correlation effects.

Equation 2.3 can be rewritten in terms of the electron density $n(\mathbf{r})$. This is stated by the first Hohenberg-Kohn theorem. Combining this with a single-particle version of Equation 2.2 yields the coupled Kohn-Sham equation system

$$[-\frac{1}{2m}\nabla^2 + \hat{v}_{eff}(n(\mathbf{r}))]\ \ \psi_i(\mathbf{r}) \ = \ \varepsilon_i\ \ \psi_i(\mathbf{r}) \tag{2.5}$$

$$n(\mathbf{r}) \ = \ \sum_{i=1}^{N} |\psi_i(\mathbf{r})|^2. \tag{2.6}$$

This system can be solved iteratively. Starting with an educated guess for the electron density $n_1(\mathbf{r})$, the single-particle wave functions $\psi_i^1(\mathbf{r})$ are calculated with Equation 2.5. Then Equation 2.6 is used to calculate the electron density $n_2(\mathbf{r})$ from the wave functions $\psi_i^1(\mathbf{r})$. The new electron density is in turn used to calculate new wave functions and the process is repeated until self-consistency is achieved (i.e. $|n_{j-1}(\mathbf{r}) - n_j(\mathbf{r})| \leq \delta$, where δ is the convergence criterion).

No experimental parameters are needed to solve the Kohn-Sham equations. Any such method is called ab initio or first-principles method. In practice however, to solve the Kohn-Sham equations on a computer, a number of calculation parameters are needed.

Firstly, a basis set has to be chosen. Common choices are plane waves or atomic orbitals. Plane waves are suitable for periodic systems and atomic orbitals can accurately describe wave functions close to the atoms. For these reasons, some methods combine both basis sets.

All of the established electronic structure programmes work in the reciprocal k-space. In this case, not the positions x of the electrons but their momenta k are used as variables. The k-points, for which the Kohn-Sham equations should be solved, have to be chosen.

Furthermore, for crystalline solids, the unit cell of the structure has to be defined and periodic boundary conditions are used to find a solution.

Some programmes do not use the full-potential of the Schrödinger equation, but work with pseudopotentials. These pseudopotentials are created to reproduce the physical behaviour of the system, but avoiding strong fluctuations of the wave function close to the nuclei which makes them computationally easier to handle.

One other thing that has to be chosen is the explicit form of the exchange-correlation potential v_{XC}, which is discussed in the following section.

2.4.3 Exchange-Correlation Potential

The Kohn-Sham equations yield exact solutions for the electronic Schrödinger equation, assuming that the exchange-correlation potential v_{XC} is exactly known. Unfortunately, this is not the case.

Common approximations for v_{XC} are the local density approximation (LDA) and the generalised gradient approximation (GGA), which are both included in the original works of Hohenberg and Kohn [32].

LDA

LDA approximates the local electron density by the density of the homogeneous interacting electron gas. If the exchange-correlation potential is written as

$$v_{\mathrm{XC}}(\mathbf{r}) = \frac{\delta E[n(\mathbf{r})]}{\delta n(\mathbf{r})}, \tag{2.7}$$

the corresponding energy functional is

$$E_{XC}[n(\mathbf{r})] = \int n(\mathbf{r})\ \epsilon_{\mathrm{XC}}(n(\mathbf{r}))\ \mathrm{d}\mathbf{r}. \tag{2.8}$$

$\epsilon_{\mathrm{XC}}(\mathbf{r})$ is the exchange-correlation energy of the homogeneous interacting electron gas with density $n(\mathbf{r})$. It can be split into contributions from exchange and from correlation.

$$\epsilon_{\mathrm{XC}} = \epsilon_{\mathrm{X}} + \epsilon_{\mathrm{C}} \tag{2.9}$$

The exchange part is equal to

$$\epsilon_{\mathrm{X}}(n(\mathbf{r})) = -\frac{3}{4}\left(\frac{3}{\pi}n(\mathbf{r})\right)^{1/3} \tag{2.10}$$

and can be derived analytically (e.g. see [59]). For the correlation part, accurate values have been calculated by Ceperley and Alder using quantum Monte Carlo simulations [60].

GGA

LDA only takes into account the local density $n(\mathbf{r})$. GGA is an extension of LDA that also uses the gradient of the local density $\nabla n(\mathbf{r})$. This slightly changes the exchange-correlation energy in Equation 2.8.

$$E_{XC}[n(\mathbf{r})] = \int n(\mathbf{r})\ \epsilon_{\mathrm{XC}}(n(\mathbf{r}),\, \nabla n(\mathbf{r}))\ \mathrm{d}\mathbf{r}. \tag{2.11}$$

Nowadays, even higher derivatives $[\nabla^2 n(\mathbf{r})]$ are used in so-called meta-GGA functionals.

2.5 Monte Carlo Simulations

Monte Carlo (MC) simulation is an integration technique based on the drawing of random numbers. It is used in cases where analytical solutions are complicated or impossible to achieve. Due to the law of large numbers, MC simulation can be very accurate. Various MC variants that are used in condensed matter physics will be described in the following.

2.5.1 Canonical and Grand-Canonical Ensemble

In statistical mechanics, a variety of different ensembles is used to describe the properties of systems. Each ensemble corresponds to a specific physical situation.

In the canonical ensemble, the number of particles N, the volume V, and the temperature T are constant. For this reason, this is also called NVT-ensemble. The corresponding physical situation is a box of a fixed size that is coupled to a heat bath. No particles can enter or exit the box, but heat can be exchanged and the heat bath keeps the temperature of the box constant.

Another important ensemble is the grand-canonical ensemble. Here, the particle number is no longer constant, but is regulated by the fixed chemical potential μ of the particle reservoir. Volume and temperature are kept constant, as in the canonical ensemble. Accordingly, the grand-canonical ensemble is also called μVT-ensemble.

A state that is characterised by the exact positions (and momenta) of all particles in the system is called a microstate γ. A macrostate on the other hand is only characterised by the parameters of the ensemble. For instance, in the canonical ensemble a system could be in a macrostate with $N = N_0$, $V = V_0$, and $T = T_0$. All microstates that result in these parameter values contribute to the macrostate.

The central quantity in statistical mechanics is the partition function Z which can be used to derive all other thermodynamic quantities. The partition function of the canonical ensemble is

$$Z_c = \sum_i \exp[-\beta U(\gamma_i)], \tag{2.12}$$

which is the total number of microstates with a fixed stoichiometry D, each weighted with a Boltzmann factor. $U(\gamma_i)$ is the energy of microstate γ_i and β is equal to $\frac{1}{k_B T}$, with $k_B = 8.617 \cdot 10^{-5} \frac{\mathrm{eV}}{\mathrm{K}}$ being the Boltzmann constant and T the temperature. The sum is over all possible microstates of the system that exhibit stoichiometry D (the total phase space Γ). On a lattice, the set of all microstates γ_i is given by all possible permutations of N_A atoms of type A, N_B atoms of type B,... on $N = N_A + N_B + ...$ lattice sites.

The partition function includes only the potential energy term. The kinetic energy term drops out.

In the partition function of the grand-canonical ensemble, the Boltzmann factor gains an additional term $-\mu_j N_j$.

$$Z_{gc} = \sum_i \exp\{-\beta[U(\gamma_i) - \sum_j \mu_j N_j(\gamma_i)]\}. \tag{2.13}$$

μ_j is the chemical potential and $N_j(\gamma_i)$ is the number of particles of type j in microstate γ_i. The sum is over all microstates with all possible stoichiometries. In the grand-canonical case, the set of all microstates on a

lattice is given by the abovementioned permutation, with the extension that N_A, N_B,... can be between 0 and N and $N \geqq N_A + N_B + ...$

Usually, the partition function of a system is a priori unknown and the summation cannot be carried out explicitly.

2.5.2 Detailed Balance and Metropolis Criterion

Expectation values of observables can be calculated by sampling the phase space Γ. In the canonical ensemble, the expectation value of an observable is

$$\langle O \rangle_c = \frac{\sum_i \exp[-\beta U(\gamma_i)] O(\gamma_i)}{Z_c}, \tag{2.14}$$

In principal, the sum in the numerator has to be evaluated for the complete phase space Γ, but the sampling usually focuses on the relevant regions with non-negligible contributions to the expectation value. The task can be performed with MC simulations. This is done by setting up the system in an arbitrary state and starting the simulation. With a suitable algorithm, the system will move through the accessible phase space Γ and sample the regions $\Delta\Gamma$ according to the probability density of Γ. A suitable algorithm is described in the following.

A MC step (also called MC move) in condensed matter physics is usually the addition, removal, or displacement of one or more particles of random choice. The moves are accepted or rejected with a certain probability by drawing a random number. The probabilities only depend on the current state and not on the history of the system. Hence, the moves form a Markov chain.

The probability of finding the system in microstate γ_i is given by

$$p_c(\gamma_i) = \frac{1}{Z_c} \mathrm{e}^{-\beta[U(\gamma_i)]}. \tag{2.15}$$

The Markov chain needs to follow a Boltzmann distribution to create a series of states in thermal equilibrium. A common way of achieving this is to use the Metropolis algorithm [34]. The probability of the system moving from a microstate γ_i to a microstate γ_j and the probability of the reverse process are then interrelated by

$$\frac{p_c(\gamma_i \rightarrow \gamma_j)}{p_c(\gamma_j \rightarrow \gamma_i)} = \mathrm{e}^{-\beta[U(\gamma_j) - U(\gamma_i)]}. \tag{2.16}$$

The metropolis algorithm fulfils detailed balance which means that the probability of finding the system in microstate γ_i times the transition prob-

ability from γ_i to γ_j is equal to the probability of finding the system in microstate γ_j times the transition probability from γ_j to γ_i. A derivation of the Metropolis algorithm can be found in [61].

In the grand-canonical ensemble, the particle number is no longer fixed. This gives rise to an additional term μN in the Boltzmann factor in Equation 2.15. If the system contains several different types of particles, the term $\mu_m N_m$ is added for every type of particle. The probability for a microstate γ_i is then

$$p_{gc}(\gamma_i) = \frac{1}{Z_{gc}} \mathrm{e}^{-\beta[U(\gamma_i) - \sum_m \mu_m N_m]} \tag{2.17}$$

and the ratio of transition probabilities is

$$\frac{p_{gc}(\gamma_i \rightarrow \gamma_j)}{p_{gc}(\gamma_j \rightarrow \gamma_i)} = \mathrm{e}^{-\beta[U(\gamma_j) - U(\gamma_i) - \sum_m \mu_m \Delta N_m]}. \tag{2.18}$$

The energy gain for adding one atom of type m is given by the chemical potential μ_m and ΔN_m is $+1(-1)$ for adding (removing) one atom of type m.

When adding an atom to the system, the energy gain will vary depending on the environment in which the atom is placed. Therefore, the chemical potential is the average energy gain of all possible environments, weighted by their probability.

It is important to note that the calculation of chemical potentials via DFT yields values that correspond to the chemical potentials measured in experiment up to a constant. This constant depends on the DFT method[62].

2.5.3 Multi-Histogram Simulations

For any system, the stable macrostate for a certain temperature T is the state with the lowest free energy F. The free energy not only takes into account the configurational energy, but also the entropy of the system ($F = U - TS$). Alternatively, the free energy can be written as the partition function of the microstates contributing to a macrostate. Let λ be a quantity that is chosen as an order parameter of the system. The Landau free energy of a macrostate, characterised by λ, is

$$F(\lambda) = -k_B T \ln Z(\lambda). \tag{2.19}$$

$Z(\lambda)$ is the partition function of all states with an order parameter λ. For a countable number of microstates γ_i, it is

$$Z(\lambda) = \sum_i \delta[\lambda - \lambda(\gamma_i)] \; e^{-\beta U(\gamma_i)}. \tag{2.20}$$

$\lambda(\gamma_i)$ is the order parameter value of microstate γ_i.

The Landau free energy $F(\lambda)$ is closely related to the probability to find the system in a macrostate with a specific λ.

$$p(\lambda) = \frac{Z(\lambda)}{\sum_i Z[\lambda(\gamma_i)]}. \tag{2.21}$$

Figure 2.4 shows a typical free energy landscape and the corresponding probability distribution for a system with two (meta)stable states that are characterised by the order parameter λ. Maxima in the probability distribution $p(\lambda)$ coincide with minima in the free energy $F(\lambda)$. Sampling the phase space will lead to numerous data points within the regions of the two minima of $F(\lambda)$ and only few data points within the region of the free energy barrier between them. The barrier will not be sampled sufficiently. In addition, λ will vary only slightly between two consecutive data points in the Markov chain, thus it is very unlikely for the system to move from one minimum over the barrier to the other minimum.

Figure 2.5 shows schematic free energy landscapes for different temperatures. At the critical temperature T_0 (transition temperature), both minima are equally low (the corresponding peaks in the probability distribution are equally high) and the two macrostates are equally likely. Below T_0, the state corresponding to the left minimum in $F(\lambda)$ is more likely and above T_0 the right one is more likely.

If the system is in the low-temperature state and the temperature is increased to $T = T_0$, the system will remain in the low-temperature state if the free energy barrier is too high. In general, a temperature $T > T_0$ is necessary to enable the system to overcome the barrier and reach the high-temperature state. On the other hand, a temperature $T < T_0$ is necessary to bring the system from the high-temperature to the low-temperature state. This effect is called hysteresis.

In addition to these two issues—the sufficient sampling of unlikely configurations and the overcoming of potential barriers—a further aspect must be considered. In general, absolute values of free energy cannot be measured directly. All of these issues can be resolved through multi-histogram simulations [63] which will be introduced below.

To calculate the free energy landscape $F(\lambda)$ at a fixed temperature T, a bias potential $U_{\text{bias}}(\lambda, \lambda_i)$ is introduced for a set of supporting points $\{\lambda_i\}$. For each supporting point, a system is simulated whose biased free energy

a)

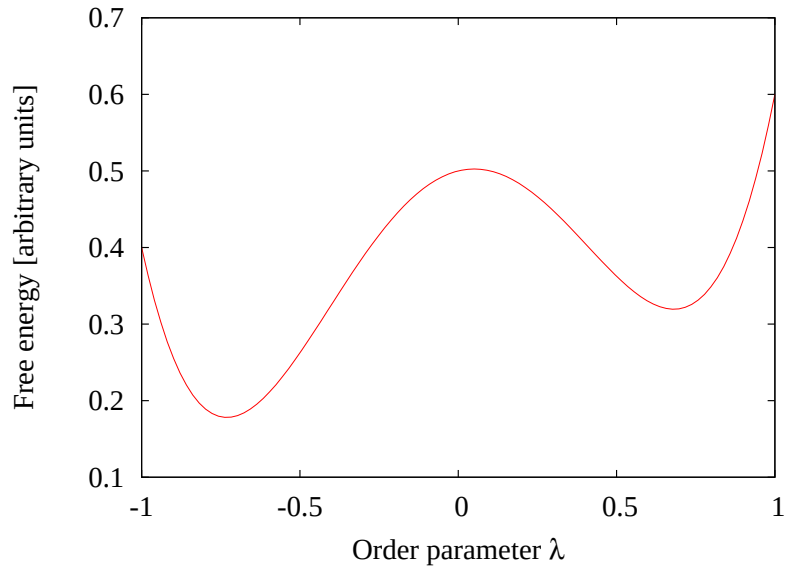

b)

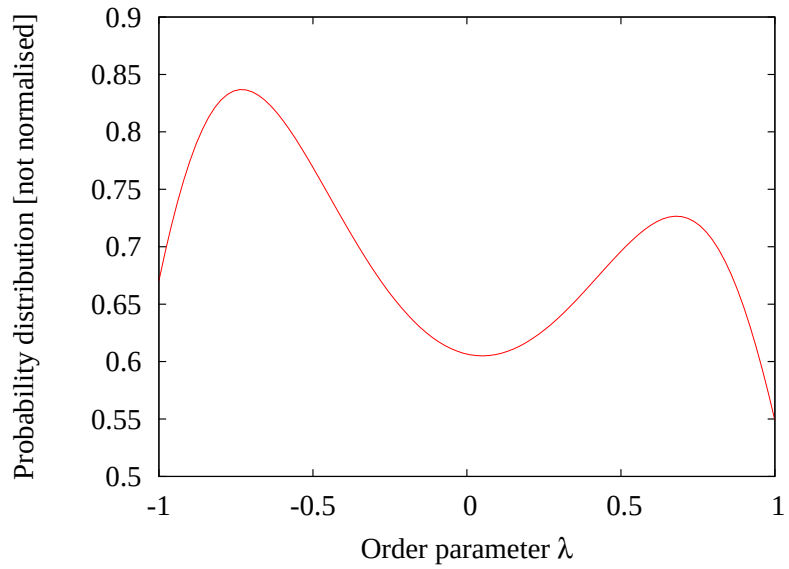

Figure 2.4: a) Schematic free energy landscape. b) Corresponding probability distribution.

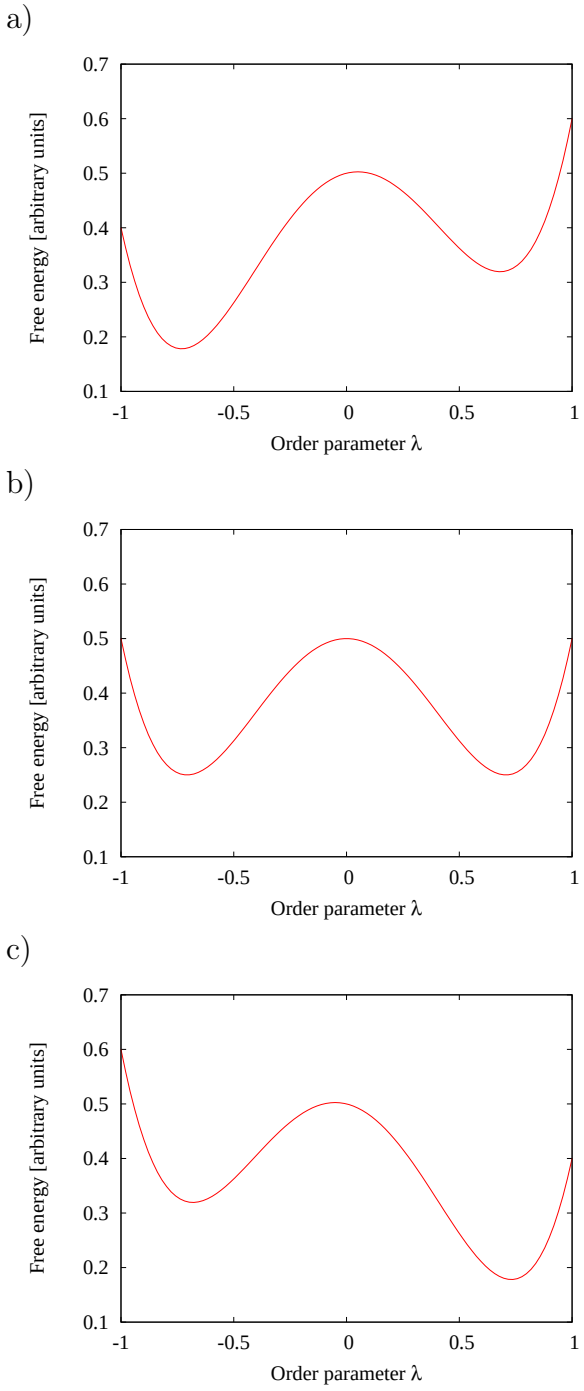

Figure 2.5: Schematic free energy landscape for a temperature a) below, b) equal to, and c) above the critical temperature T_0.

a)

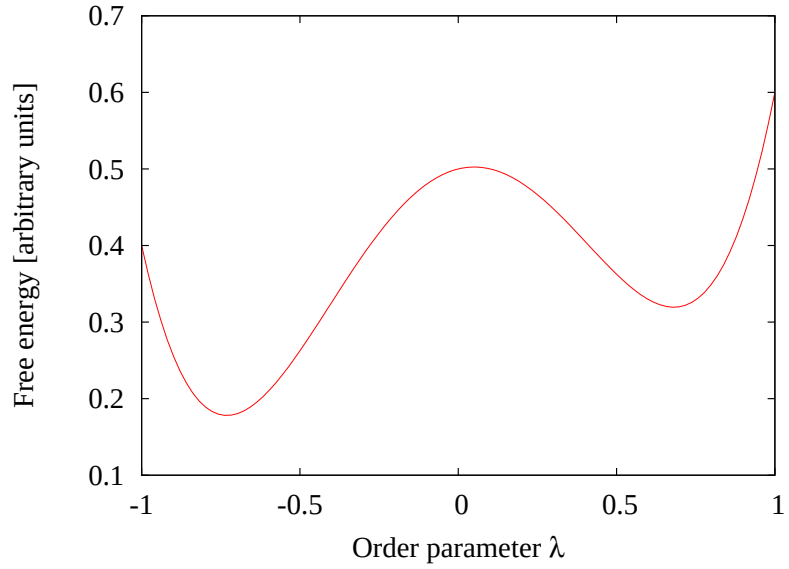

b)

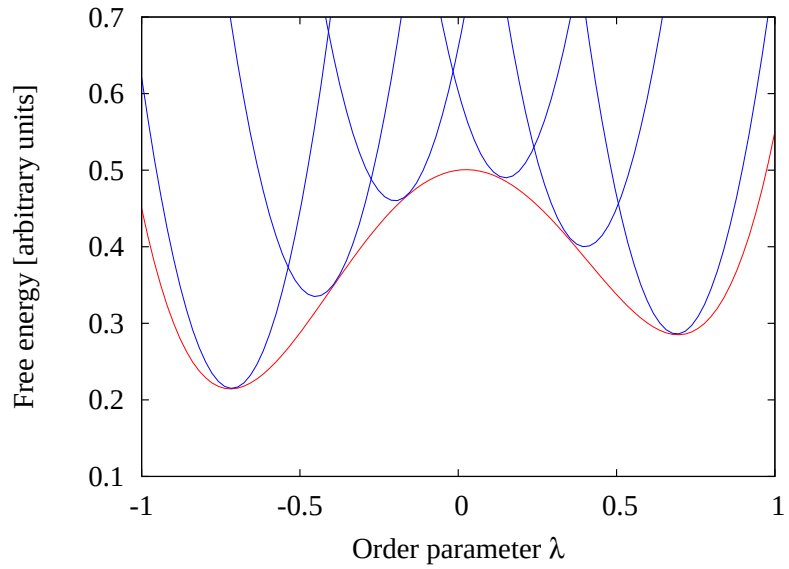

Figure 2.6: a) Schematic free energy landscape. b) Free energy landscape and parabolic bias potentials for multi-histogram sampling.

$F_i(\lambda)$ differs from the free energy of the original system by $U_{\text{bias}}(\lambda, \lambda_i)$. The bias potential is chosen in such a way that a minimum of the free energy arises in the vicinity of λ_i and the simulation windows for neighbouring λ_i overlap [Figure 2.6 b)].

For every supporting point, $F_i(\lambda)$ can be constructed from a histogram $h_i(\lambda)$. The number of entries in the histogram bins is proportional to the probability distribution

$$p_i(\lambda) = \frac{Z_i(\lambda)}{\sum_j Z_i(\lambda_j)} = \frac{h_i(\lambda)}{\sum_j h_i(\lambda_j)}. \tag{2.22}$$

The biased partition function is

$$Z_i(\lambda) = \sum_j \delta[\lambda - \lambda(\gamma_j)] \; \mathrm{e}^{-\beta\{U(\gamma_j)+U_{\text{bias}}[\lambda(\gamma_j),\lambda_i]\}}. \tag{2.23}$$

The sum $\sum_j \delta[\lambda-\lambda(\gamma_j)]$ is over all microstates γ_j with an order parameter value $\lambda(\gamma_j)$ which is equal to λ.

The biased free energy is

$$F_i(\lambda) = -k_B T \ln Z_i(\lambda) = -k_B T \ln h_i(\lambda) + C_i. \tag{2.24}$$

The free energy profile $F(\lambda)$ can be constructed piecewise from the probability distributions around the supporting points by subtracting $U_{\text{bias}}(\lambda, \lambda_i)$ from $F_i(\lambda)$. The constant contributions C_i are not determined explicitly, but from vertical adjustments of the free energy parts to obtain a smooth function in λ.

In this thesis, the configurational energy U is used as an order parameter and the parabolic bias potential is

$$U_{\text{bias}} = a(U - U_i)^2. \tag{2.25}$$

The free energy $F(U)$ without bias potential can be recovered piecewise for all free energy parts $F_i(U)$ as follows:

$$\begin{aligned} F(U) &= -k_B T \ln Z(U) \\ &= -k_B T \ln \sum_j \delta[U(\gamma_j) - U] \exp\{-\beta[U + a(U-U_i)^2 - a(U-U_i)^2]\} \\ &= -k_B T \ln Z_i(U) - k_B T \ln \{\exp[+\beta a(U-U_i)^2]\} \\ &= -k_B T \ln(h_i(U)) + C_i - a(U-U_i)^2. \end{aligned} \tag{2.26}$$

2.6 Cluster Expansions

To perform a MC simulation, the energies of atomic configurations must be calculated. Configurational energies can be calculated ab initio with electronic structure methods, but this is a time-consuming process. The energy is needed in every MC step and typically millions of steps are required for a single calculation. A solution is to expand the energy in a power series.

Cluster expansions (CEs) for condensed matter systems were first proposed by Mayer and Montroll in 1941 [64]. The configurational energy (or any other extensive quantity) can be written as a sum of cluster figure contributions

$$\begin{aligned} E(\mathbf{s}) &= J_0 + \sum_i J_i\, s_i + \sum_{i_1<i_2} J_{i_1 i_2}\, s_{i_1} s_{i_2} + ... \\ &\quad + \sum_{i_1<i_2<...<i_m} J_{i_1 i_2 ... i_m}\, s_{i_1} s_{i_2} ... s_{i_m} + ... \end{aligned} \tag{2.27}$$

This is very similar to the energy of an Ising-spin system [65]. J are the coefficients of the cluster figures and are called effective cluster interactions (ECI). The indices i run over all lattice sites and thus tuples of indices form all possible cluster figures (single atoms, pairs, triples,...). The vector $\mathbf{s}$ contains one entry per lattice site of the system. The value of s_i depends on the atom type on lattice site i. For instance, in a system with two components, the usual convention is that $s_i = \pm 1$ for the two possible occupations of lattice site i. Detailed descriptions of the two-species CE method can be found in [36].

The CE technique can be generalised for systems with more than two components [35]. This results in the following equation.

$$E(\mathbf{s}) = J_0 + \sum_{i,\alpha} J_{i\alpha} \Theta_\alpha(s_i) + \sum_{i_1<i_2,\alpha} J_{i_1 i_2 \alpha} \Theta_\alpha(s_{i_1}) \Theta_\alpha(s_{i_2}) + ... \tag{2.28}$$

The products of s_i are now replaced by products of the cluster functions $\Theta_\alpha(s_i)$. The parameter α can assume integer values within the interval $[0, n-2]$, where n is the number of components.

For a three-component system, the possible values of s_i can for instance be chosen as $-1, 0, +1$ to denote the three possible occupations of lattice site i. The two cluster functions $\Theta_1(s_i)$ and $\Theta_2(s_i)$ form a unit vector, where $\vec{\Theta}(s_i)$ and $\vec{\Theta}(s_j)$ are at an angle of 120° for $i \neq j$.

The expansions in Equations 2.27 and 2.28 are exact. However, for an implementation, it is necessary to reduce the enormous number of terms.

Negligible cluster figures are those with a low associated value of J. These usually contain a high number of member atoms or a big distance between cluster members. CEs commonly include cluster figures with up to four member atoms that have a maximum distance of no more than the third-nearest neighbour distance.

For the implementation of a CE into MC simulations, the relevant cluster figures have to be chosen and the coefficients J must be determined. To this end, a least-squares fit of the coefficients J to a limited number of ab initio calculated configurational energies is performed. If more than two components are considered in the CE, the number of energies needed increases strongly. Additionally, bigger unit cells have to be taken into account. The reason for this is the increased number and complexity of possible configurations.

Ultimately, the goal is to apply the CE to unknown structures and determine their energy. A common criterion for the measurement of the predictive power of a set X of structural energies is the cross-validation score (CVS) which is defined as

$$C_{\mathrm{CVS}}^2 = \frac{1}{N}\sum_{i=1}^{N}(E_i^{\mathrm{DFT}} - E_{(i)}^{\mathrm{CE}})^2. \tag{2.29}$$

N is the number of ab initio calculated energies and E_i^{DFT} is the ab initio energy of structure i. $E_{(i)}^{\mathrm{CE}}$ is calculated by a CE that is created without structure i, using the $N-1$ other structures of set X. The CVS is an estimation of the error made when predicting the energies of unknown structures.

Frequently, instead of the total configurational energy, the formation energy per atom is used. For a binary $A-B$ system, this is defined as

$$E_f(\mathbf{s}^m) = E(\mathbf{s}^m) - xE(\mathbf{s}^a) - (1-x)E(\mathbf{s}^b). \tag{2.30}$$

$\mathbf{s}^m$ gives the lattice occupations of configuration m, for which the formation energy per atom is to be calculated. The configurations $\mathbf{s}^a$ and $\mathbf{s}^b$ are the pure A and B compounds. The concentrations x and $(1-x)$ are the fractions of compounds A and B that are needed to achieve the stoichiometry of the structure $\mathbf{s}^m$. All energies in Equation 2.30 are per atom.

For instance, let the stoichiometry of $\mathbf{s}^m$ be $A_{0.5}B_{0.5}$. The formation energies of $\mathbf{s}^a$ and $\mathbf{s}^b$ are both zero (in all cases) and $x = (1-x) = 0.5$. If the formation energy $E_f(\mathbf{s}^m)$ is negative, then energy is gained by forming $\mathbf{s}^m$ and the configuration is stable. If $E_f(\mathbf{s}^m)$ is positive, then energy has to be spent to form $\mathbf{s}^m$ and, at low temperatures, spontaneous decomposition into an A phase and a B phase is expected.

For ternary systems, the formation energy per atom is

$$E_f(\mathbf{s}^m) = E(\mathbf{s}^m) - xE(\mathbf{s}^a) - yE(\mathbf{s}^b) - (1-x-y)E(\mathbf{s}^c), \tag{2.31}$$

and this can easily be generalised for any number of components.

In addition to the configurational energy, there are a few other effects that also contribute to the formation energy of a solid. The subsequent discussion of these effects follows [37].

The system in this discussion is a pseudo-binary $AC-BC$ system. Atoms A and B can swap their positions, while atoms C are fixed. An example for this type of system is InAs, GaAs, and the mixture $In_xGa_{1-x}As$.

One possible decomposition of the complete formation energy of a binary $AC - BC$ system would be

$$\begin{aligned} E_f(\mathbf{s}^m, V) &= \Delta E_{VD}(x, V) + \delta E_{UR}(\mathbf{s}^m, V) + \delta E_C(\mathbf{s}^m, V) \\ &\quad + \delta E^{int}_{A,B}(\mathbf{s}^m, V) + \delta E^{ext}(\mathbf{s}^m, V). \end{aligned} \tag{2.32}$$

The first term $\Delta E_{VD}(x, V)$ is the volume deformation energy that is needed to change the volume of AC from V_{AC} to V, and that of BC from V_{BC} to V. This directly depends on the concentration parameter x. The contribution is big for systems where the lattice constants of AC are very different from the lattice constants of BC. It is calculated by

$$\begin{aligned} \Delta E_{VD}(x, V) &= x[E(AC, V) - E(AC, V_{AC})] \\ &\quad + (1-x)[E(BC, V) - E(BC, V_{BC})]. \end{aligned} \tag{2.33}$$

The second term in Equation 2.32, $\delta E_{UR}(\mathbf{s}^m, V)$, is the configurational formation energy from Equation 2.30 with all atoms sitting on the ideal lattice sites which can be handled with the CE approach.

The third term $\delta E_C(\mathbf{s}^m, V)$ is the energy gain from the relaxation of the C atoms, while holding A and B fixed at the ideal lattice sites. Reference [37] states that δE_C is the dominant relaxation in $AC - BC$ semiconductor alloys.

The fourth term $\delta E^{int}_{A,B}(\mathbf{s}^m, V)$ is the energy gained when all A and B atoms are allowed to relax, but the unit cell vectors are kept constant. The last term $\delta E^{ext}(\mathbf{s}^m, V)$ gives the energy gain from the relaxation of the unit cell vectors.

The CEs in this thesis are created by using fully relaxed structures (positions of all atoms, angle and length of unit cell vectors). Consequently, they include all energy contributions, except $\Delta E_{VD}(x, V)$.

Chapter 3

Software

3.1 ATAT

The Alloy Theoretic Automated Toolkit (ATAT) is a software package that was developed by Axel van de Walle [66, 67]. It runs on Linux systems and allows the automated generation of CEs.

ATAT uses a collection of programmes and bash-scripts to perform the necessary steps towards the creation of a CE. Firstly, input files have to be provided that define the lattice and the possible site occupations. From these input files, the MAPS-script which is part of ATATautomatically creates structures.

In the next step, an electronic structure programme (DFT-code) has to be chosen. The communication between the DFT-code and ATAT is managed by bash-scripts. A variety of different scripts exists for different codes. For this thesis, the DFT-codes ABINIT and QUANTUM ESPRESSO were used. The existing communication scripts for these had to be modified for the specific needs of the investigation.

The communication script translates the MAPS-generated structures into input files that are readable by the chosen DFT code. This is performed using an additional user-generated input file which contains necessary input parameters such as the number of k-points.

After the DFT code has calculated the energy (and other necessary properties), the MAPS script generates a CE from all the energies of structures that have been calculated so far. It also calculates the CVS. Then it systematically creates new structures that are expected to improve the CE and reduce the CVS. MAPS continues to improve the CE until the user is satisfied and stops the procedure. A good CE not only needs a low CVS, but more importantly, the structures that are predicted by ATAT to be ground states

have to have the lowest energies for the specific stoichiometry. Otherwise the CE needs more improvement.

The information for the CE is written into a number of output files. The file clusters.out contains all cluster figures that are not neglected, eci.out contains the corresponding coefficients, and sym.out contains the symmetry operations that have to be applied to a cluster figure to obtain all symmetrically equivalent cluster figures. The file fit.out includes the calculated ab initio formation energies for all configurations and the corresponding CE energies.

3.2 ABINIT

ABINIT [68–70] is an ab initio electronic structure programme that uses plane waves as a basis set and pseudopotentials. It was run on a p590 machine that was provided by IBM. In the following, the tests are described that were performed to find a suitable parameter set for the ABINIT calculations.

In MC simulations, only the energy differences are relevant. The task for ABINIT is thus to calculate accurate configurational energy differences. In a first step, it was tested whether the pseudopotentials yield reasonable results. This was done by calculating the energy difference of two typical CIGS structures with ABINIT and the electronic structure programme WIEN2K [71]. WIEN2K serves as a full-potential high-accuracy reference. Table 3.1 summarises the results (and includes PWSCF results that are discussed in Section 3.3). Two typical cases for an atom-swap are considered. In both cases the programmes yield comparable energy differences. More importantly, the corresponding Boltzmann factors $e^{-\beta\Delta E}$ are in good agreement at $T = 300$ K. These factors are the acceptance probability according to the Metropolis criterion, which is used in the MC simulations.

The energy differences between regular $CuInSe_2$ and $CuInSe_2$ with one Cu and one In swapped lead to a probability of over 99% that the MC move is rejected and the energetically more favourable structure is preserved. The three programmes agree on this. In the case of $Cu(In,Ga)Se_2$, the energy differences are much smaller. The ABINIT and the WIEN2K values differ by only 0.8 meV per atom, which is a reasonable accuracy for DFT calculations.

The chosen pseudopotentials are of the Troullier-Martins-type (norm-conserving) [72] and use the generalised gradient approximation of Perdew, Burke, and Ernzerhof [73].

Table 3.1: Converged energy differences for ABINIT, PWSCF, and WIEN2K. The $CuInSe_2$-difference is the energy difference between the usual $CuInSe_2$ unit cell and a cell where a Cu and an In atom are exchanged. The $Cu(In,Ga)Se_2$-difference is for a relaxed $CuIn_{0.5}Ga_{0.5}Se_2$ cell and a relaxed cell where an In and a Ga atom are exchanged. The exponential is the probability of accepting a MC move (Metropolis criterion) from the low-energy structure to the structure with higher energy at a temperature of $T = 300$ K.

Programme	$CuInSe_2$-difference [meV/atom]	$e^{-\beta\Delta E}$	$Cu(In,Ga)Se_2$-difference [meV/atom]	$e^{-\beta\Delta E}$
WIEN2K	123.5	0.008	1.8	0.933
ABINIT	129.4	0.007	2.6	0.904
PWSCF	130.5	0.006		

3.3 QUANTUM ESPRESSO

Like ABINIT , QUANTUM ESPRESSO [74] is an ab initio electronic structure programme that uses plane waves as a basis set and pseudopotentials. It is also referred to as PWSCF after its main executable. The programme was run on a Blue Gene/p machine at the IBM T.J. Watson Research Center in Yorktown Heights, New York, USA. Up to 1024 processors could be utilised at the same time.

Ultra-soft Vanderbilt-type pseudopotentials [75] were chosen and tested against WIEN2K and ABINIT (cf. Table 3.1). All three programmes yield comparable energy differences.

3.4 Monte Carlo Code

The code for the MC simulations was developed within the scope of this thesis. It is written in C++ and runs in serial mode on ordinary Linux systems. The random number generator that was used is a Mersenne twister which was developed by Makoto Matsumoto and Takuji Nishimura [76]. In all simulations, periodic boundary conditions are used.

In a first step, the programme reads the ATAT files clusters.out, eci.out, and sym.out. All symmetrically equivalent cluster figures are created by applying the symmetry operations from sym.out to the figures in clusters.out. After that, all duplicate figures are removed.

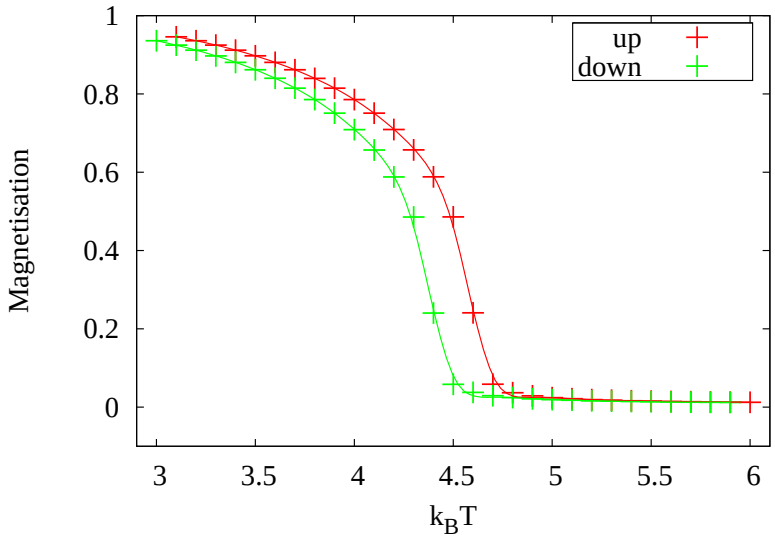

Figure 3.1: Magnetisation M versus temperature k_BT for a system of $30 \times 30 \times 30$ Ising-spins. MC runs with increasing temperature (red) and decreasing temperature (green) show a hysteresis. Cubic splines have been fitted to the data to guide the eye.

In the next step, every lattice site is associated with a list of cluster figures that include this site and the respective ECIs. This guarantees quick access to all relevant figures when the site occupation is changed. The energy is calculated according to Equation 2.27 or 2.28 respectively.

The correctness of the code was tested thoroughly. Configurations were chosen from the ATAT configuration set and their energy was calculated with the MC code. The MC-calculated energies and the energies given by ATAT match exactly. This proves the correct implementation of the energy calculation.

Furthermore, the code was used to simulate an Ising-spin system [65]. This system has been thoroughly investigated before and the results can easily be compared with literature to validate the MC code. The only relevant cluster figures are nearest-neighbour pair-interactions with an equal value for the ECIs. Figure 3.1 shows the temperature dependence of the magnetisation for a system of $30 \times 30 \times 30$ Ising-spins.

At low temperatures, all spins point in the same direction and the magnetisation is 1. At the phase transition temperature, the magnetisation decreases strongly and above $k_BT = 5$, the direction of the spins is equally distributed ($M = 0$). The transition point for a run with a decreasing tem-

perature is slightly shifted, compared to a run with an increasing temperature, due to hysteresis.

The exact transition point was determined using the Binder cumulant [77]

$$U_4 = 1 - \frac{\langle M^4 \rangle}{3\langle M^2 \rangle^2}. \tag{3.1}$$

This is calculated for various system sizes. According to theory, the plots of U_4 for these different system sizes intersect at the transition point. Due to the hysteresis effect, the transition points for increasing and decreasing temperatures are slightly different as can be seen in Figure 3.2.

The arithmetic mean of the two transition points is an estimate for the equilibrium transition temperature. It is at $k_B T = 4.50$ which is in good agreement with the literature value of $k_B T = 4.51$ [78]. Hence, the MC code runs properly and can be used to investigate CIGS based on a CE.

a)

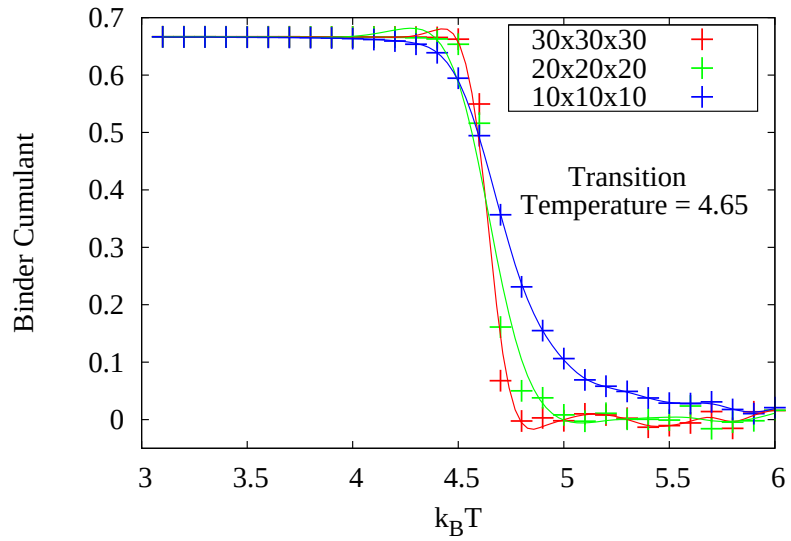

b)

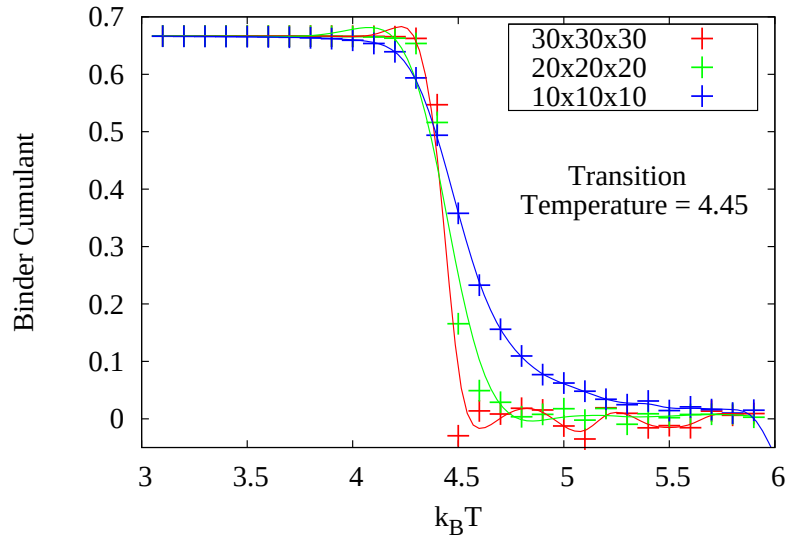

Figure 3.2: Binder cumulant U_4 versus temperature k_BT for a) increasing and for b) decreasing temperature and for system sizes of $30 \times 30 \times 30$, $20 \times 20 \times 20$, and $10 \times 10 \times 10$. The transition temperature is at the intersection of the data sets. Cubic splines have been fitted to the data to guide the eye.

Chapter 4

Simulations

In this chapter, the results of the DFT and MC simulations will be discussed.

4.1 In-Ga Cluster Expansion

The following results were published in Physical Review Letters [79].

A Cu(In,Ga)Se_2 CE was created to investigate the spatial distribution of In and Ga in CIGS. ATAT (cf. Section 3.1) was used to create 32 structures. The structures are up to two unit cells big (the unit cell structure is described in Section 2.3). Cu and Se are kept fixed. In and Ga are distributed on the remaining lattice sites.

The total energies of all structures were calculated with the ab initio electronic structure programme ABINIT (cf. Section 3.2). The cut-off energy for the plane waves was set to 140 Ry and a k-point grid of $3 \times 3 \times 3$ or bigger was used. The positions of all atoms were relaxed until the maximum force on atoms was less than 10^{-3} hartree/bohr and all three lattice parameters were relaxed until the stress was less than 10^{-5} hartree/bohr^3.

The first studied structures are the $CuInSe_2$ structure (cf. Figure 2.3) and the $CuGaSe_2$ structure. Table 4.1 lists some parameters of the structures and compares them with experimental values and other calculations. The table also includes the $CuInSe_2$ values that were obtained with QUANTUM ESPRESSO (Section 4.2).

The calculations reproduce the experimental $\frac{c}{a}$ ratio and the anion displacement very well. The lattice constant a is 2.2% ($CuInSe_2$) and 1.5% ($CuGaSe_2$) bigger than the experimental value. These deviations are still within a reasonable range. The calculated parameter values from Reference [80] are better (closer to experiment) in the case of the lattice constant and worse in the case of $\frac{c}{a}$ ratio and anion displacement. Their smaller lattice

Table 4.1: Comparison of calculated parameters of $CuInSe_2$ and $CuGaSe_2$ with literature values.

	Lattice constant a [Å]	$\frac{c}{a}$ ratio	Anion displacement
$CuInSe_2$			
ABINIT calculations	5.9109	2.011	0.220
PWSCF calculations (Section 4.2)	5.8612	2.009	0.217
Reference [43] (experiments)	5.7841	2.008	0.224
Reference [80] (calculations)	5.733	1.988	0.250
$CuGaSe_2$			
ABINIT calculations	5.6967	1.977	0.247
Reference [43] (experiments)	5.6141	1.965	0.250
Reference [80] (calculations)	5.542	1.957	0.260

constant is due to the use of LDA potentials. The ABINIT calculations used GGA potentials which typically yield bigger lattice constants (e.g. see [81]).

The formation energies, calculated ab initio and with the CE that was fitted to the 32 ABINIT energies, are given in Figure 4.1. The agreement is very good which is reflected by the low CVS of $C_{\text{CVS}} = 1.3$ meV. The representative cluster figures of the CE are given in Table 4.2.

The multiplicity is the number of distinct cluster figures that result from the representative by applying the 16 symmetry operations of the unit cell ($I\bar{4}2d$) to it. The total number of distinct cluster figures is 137.

The In-Ga CE not only includes the configurational energy $\delta E_{UR}(\mathbf{s}^m, V)$ of Equation 2.32, but also includes the relaxation terms $\delta E_C(\mathbf{s}^m, V)$, $\delta E^{int}_{A,B}(\mathbf{s}^m, V)$, and $\delta E^{ext}(\mathbf{s}^m, V)$. This is due to the fact that all atoms and lattice vectors were relaxed in the ABINIT calculations.

The only energy contribution that is not taken into account is the volume deformation energy $\Delta E_{VD}(x, \mathbf{s}^m)$. However, this term only plays a role if the concentration x (stoichiometry) is changed during a MC run. For a fixed concentration, $\Delta E_{VD}(x, \mathbf{s}^m)$ is just a constant (under the reasonable assumption that the effect of the configuration $\mathbf{s}^m$ is negligible). All simulations that used the In-Ga CE were canonical (fixed concentration).

Canonical MC simulations were performed for In-rich CIGS ($CuIn_{0.75}Ga_{0.25}Se_2$) and for Ga-rich CIGS ($CuIn_{0.25}Ga_{0.75}Se_2$). One MC move consists of exchanging the position of two active atoms (In/Ga). The simulation box contains 16×16×8 tetragonal CIGS unit cells (8192 active atoms). Simulations were run at fixed temperatures between 290 K (corresponding to a energy of 25 meV) and 870 K (corresponding to 75 meV,

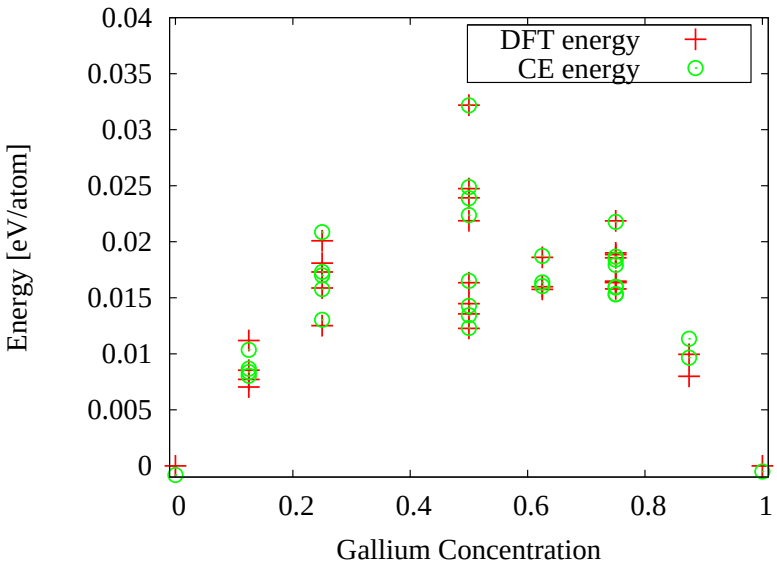

Figure 4.1: Formation energies of 32 Cu(In,Ga)Se_2 structures, calculated with ABINIT and the CE.

approximately the production temperature of CIGS solar cells) for 10^6 MC sweeps. Relaxation to the equilibrium state took fewer than 10^5 MC sweeps.

For data analysis, the simulation box was divided into cubic segments of 16 active lattice sites (occupied by In or Ga). The number of In (Ga) atoms b in each segment was counted and histograms were plotted. A schematic explanation of how the histograms are created is given in Figure 4.2.

Figure 4.3 shows the simulation data for various temperatures. The histograms display the number of Ga atoms (yellow) in In-rich CIGS and the number of In atoms (blue) in Ga-rich CIGS. The arithmetic mean for the distributions is always 4. The standard deviation σ of the histograms can be computed to have a measure for the homogeneity. σ increases with decreasing homogeneity. All computed values are compiled in Table 4.3.

At 290 K [Figure 4.3 a)], the histograms have two maxima: one at the lower and one at the higher end of the scale. The majority of the segments contain very few or no In (Ga) atoms, but the small maximum indicates that a certain fraction of segments contain a large fraction of In (Ga) atoms. This means that there are two phases: an In phase and a Ga phase. The snapshots in Figure 4.4 a) and b) illustrate this conclusion.

Both maxima in Figure 4.3 a) are higher for Ga-rich CIGS. Close to the mean value of 4, the values for In-rich CIGS are higher, therefore the distribution is narrower. This is reflected by the standard deviation σ which

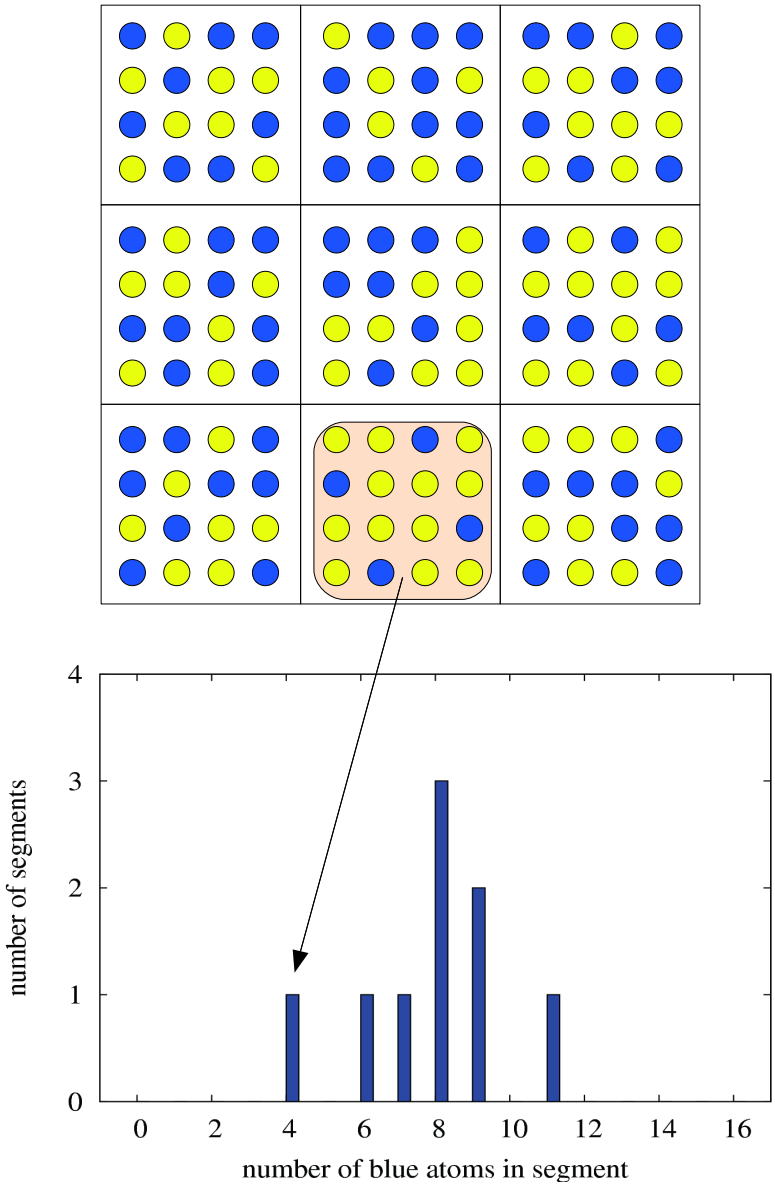

Figure 4.2: Scheme for the creation of histograms. The simulation volume is divided into segments with 16 atoms each. The number of blue atoms b in each segment is counted and the histogram reflects the frequency of all possible values of b. The arrow indicates that a segment with 4 blue atoms leads to an entry in bin 4 of the histogram.

Table 4.2: Representatives of cluster figures and ECIs for the In-Ga CE. Figures with an ECI of zero are not listed.

	Reduced coordinates	Multiplicity	ECI [meV]
Empty figure	–	1	78.985
Point figure	(0.5, 0.5, 1)	4	0.909
Pair figures	(1, 1, 0.5), (1, 0.5, 0.75)	8	0.650
	(0.5, 1, 0.25), (1.5, 1, 0.25)	8	−4.412
	(0.5, 1, 0.25), (1.5, 1.5, 0)	16	−2.238
	(0.5, 0.5, 1), (0, 0, 1.5)	16	−2.258
	(0.5, 1, 0.25), (1.5, 0, 0.25)	8	−0.295
	(0.5, 1, 0.25), (0, 1, −0.5)	8	0.091
	(1, 1, 0.5), (1, 1, 1.5)	4	0.658
	(1, 1, 0.5), (1, 0, 1.5)	16	1.006
Triple figures	(0.5, 1, 0.25), (1, 1, 0.5), (0.5, 1, 0.25)	8	−0.607
	(0.5, 1, 0.25), (0.5, 1.5, 0), (1.5, 1.5, 0)	16	0.114
Quadruple figures	(0.5, 1, 0.25), (0.5, 1.5, 0), (1.5, 1, 0.25), (1.5, 1.5, 0)	8	−0.377
	(0.5, 1, 0.25), (0.5, 1.5, 0), (0.5, 2, 0.25), (1.5, 1.5, 0)	16	0.395

is 3.8% higher for Ga-rich CIGS, indicating a lower homogeneity (higher disorder).

At a temperature of 406 K [Figure 4.3 b)], the system has undergone a phase transition to a mixed, disordered phase. The histograms have changed drastically and show one broad peak with a long tail towards higher atom numbers. This is accompanied by a big change of σ to smaller values for both systems. Snapshots are shown in Figure 4.4 c) and d). The difference in homogeneity is very pronounced; σ is 9.2% higher for Ga-rich CIGS, the largest difference for all considered temperatures.

At higher temperatures [Figures 4.3 c) and d)] the shape of both histograms becomes narrower and the difference between In-rich and Ga-rich CIGS becomes smaller.

Table 4.3 contains the σ values for more temperatures. It can be seen that σ is smaller for In-rich CIGS at all temperatures and σ decreases with temperature for In-rich and Ga-rich CIGS. The relative difference in σ between the two is largest at 406 K, close to the phase transition.

a)

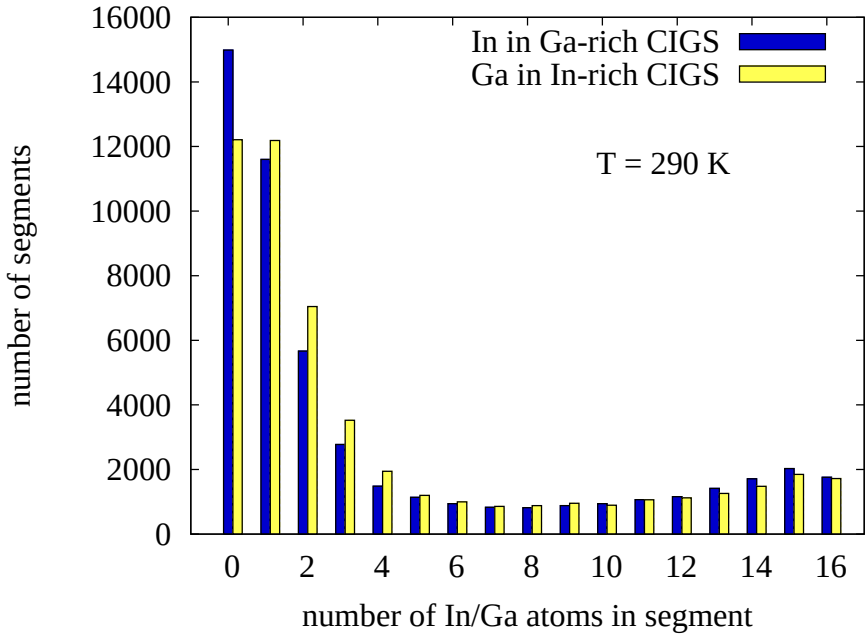

b)

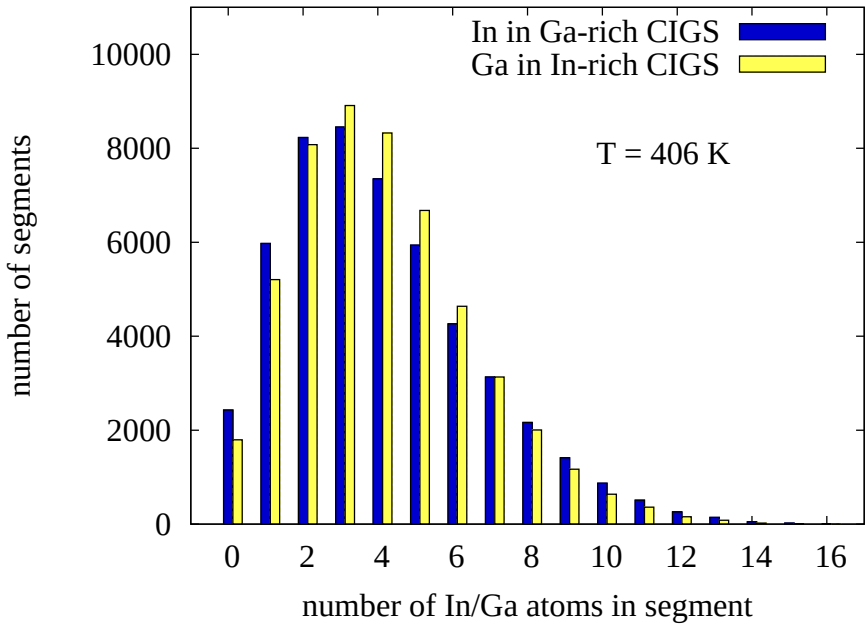

Figure 4.3: Histograms of the In distribution in Ga-rich CIGS (blue) and the Ga distribution in In-rich CIGS (yellow) at temperatures of a) 290 K, b) 406 K, c) 580 K, and d) 870 K.

c)

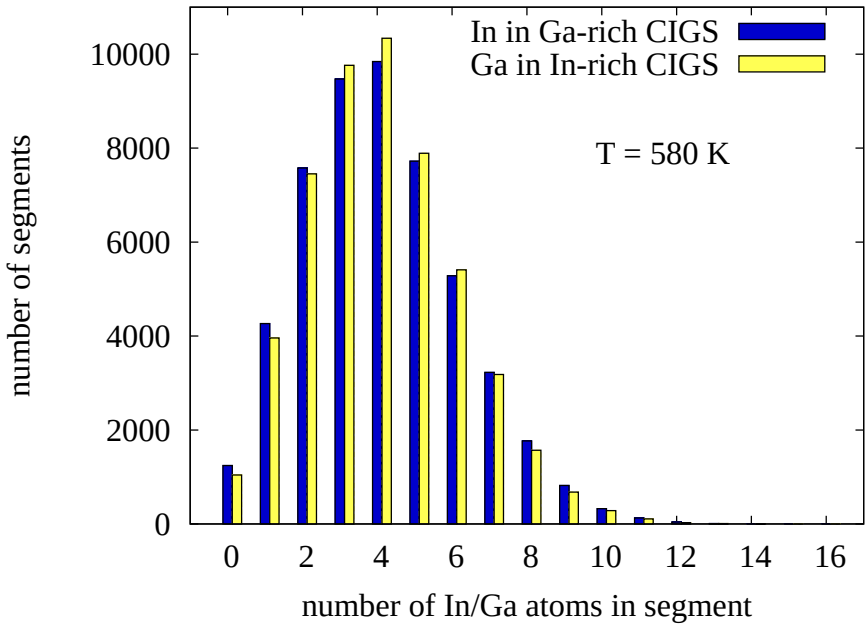
In in Ga-rich CIGS
Ga in In-rich CIGS
T = 580 K
number of segments
number of In/Ga atoms in segment
0
2000
4000
6000
8000
10000
0
2
4
6
8
10
12
14
16

d)

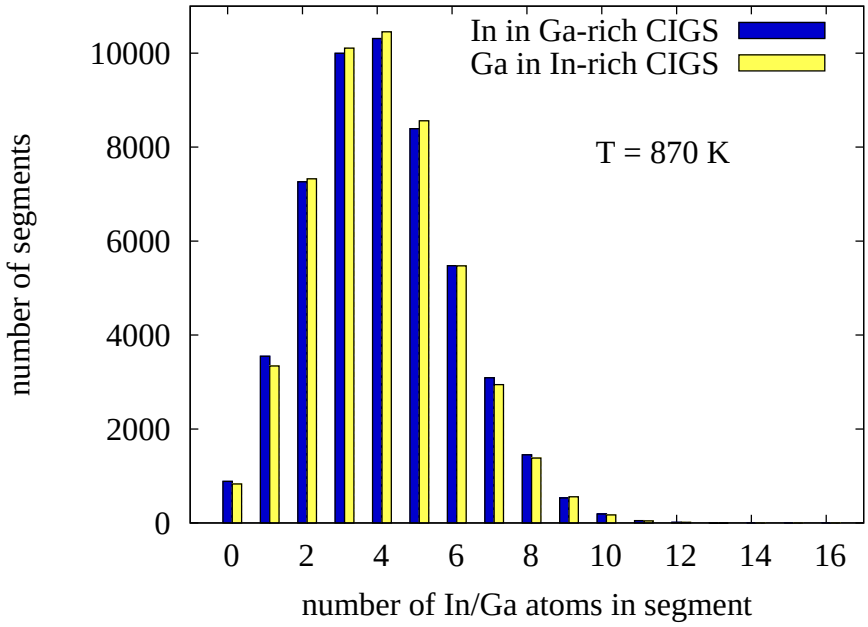
In in Ga-rich CIGS
Ga in In-rich CIGS
T = 870 K
number of segments
number of In/Ga atoms in segment
0
2000
4000
6000
8000
10000
0
2
4
6
8
10
12
14
16

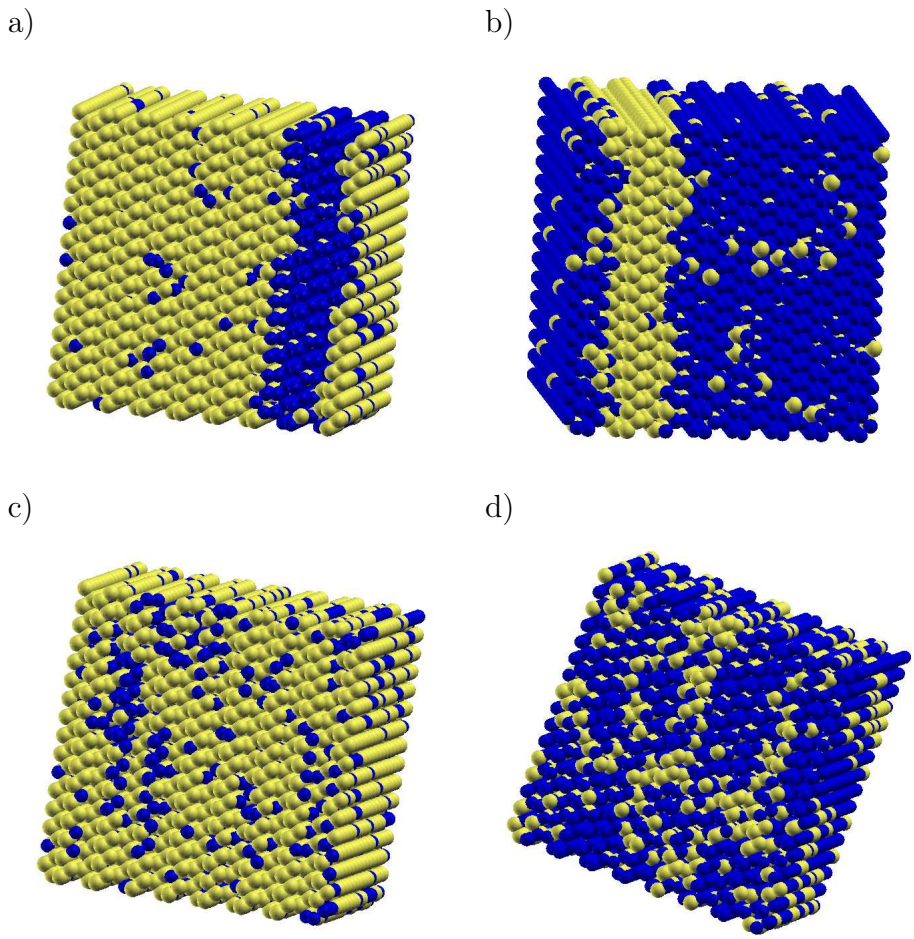

Figure 4.4: Snapshots of a) Ga-rich CIGS at 290 K, b) In-rich CIGS at 290 K, c) Ga-rich CIGS at 406 K, and d) In-rich CIGS at 406 K.

It is interesting to compare the simulation results with recent photoluminescence (PL) experiments by Gütay and Bauer, who measured the local band gaps on an In-rich CIGS surface. Scanning 40000 pixels of 200 nm width, they found a Gaussian-like distribution of band gaps with a FWHM (full width of half maximum) of 8 meV [82].

The histograms of the simulation data can be translated into band gap distributions using the band gaps of the respective Ga concentrations [8]. If the size of the segments (i.e. the number of atoms in it) is increased by a factor of N, the relative width w of the histograms decreases approximately as $1/\sqrt{N}$. To compare with the abovementioned experiment, the width from the

Table 4.3: σ (inhomogeneity) for In-rich and Ga-rich CIGS and relative difference.

Temperature	σ (In-rich)	σ (Ga-rich)	$\frac{\sigma(Ga-rich)}{\sigma(In-rich)} - 1$
290 K	4.97	5.16	3.8%
348 K	3.96	4.24	7.1%
406 K	2.39	2.61	9.2%
464 K	2.18	2.31	6.0%
522 K	2.07	2.19	5.8%
580 K	2.03	2.10	3.4%
638 K	1.99	2.06	3.5%
696 K	1.96	2.01	2.6%
754 K	1.93	1.97	2.1%
812 K	1.91	1.95	2.1%
870 K	1.90	1.93	1.6%

simulation results has to be extrapolated to a segment size that is comparable to the scan-pixels.

A length of 200 nm corresponds to roughly 346 CIGS unit cells in the direction of lattice constant a. The scan-pixels can be approximated by segments of $346 \times 346 \times 1$ unit cells which contain 478864 active lattice sites (occupied by In or Ga). The relative FWHM (full width at half maximum) of the histograms is determined for segment sizes of 16, 128, and 1024 active lattice sites. The relative FWHM is defined as the FWHM divided by number of bins in the histogram.

In-rich CIGS at 870 K has relative widths of 29.4% (16 active sites), 10.1% (128 active sites), and 3.4% (1024 active sites) respectively. Using the dependence of the relative width w on the segment size N, the data points can be fitted with the model function $w = AN^{-m}$. A simple least squares fit yields $A = 123$ and $m = 0.515$. For an infinitely large system, an exponent m of 0.5 would be expected. The fitted value is higher due to finite size effects.

Using the fitted parameters in the model function yields a relative width $w = 0.145\%$ for $N = 478864$ active sites. Applying this to the band gap range of 0.7 eV ($\mathrm{gap}_{\mathrm{CuGaSe_2}} - \mathrm{gap}_{\mathrm{CuInSe_2}}$) results in band gap fluctuations of 1.01 meV (FWHM).

In-rich CIGS at 406 K has relative widths of 35.3% (16 active sites), 14.0% (128 active sites), and 4.8% (1024 active sites) respectively. The same reasoning as for the 870 K case leads to band gap fluctuations of 2.20 meV (FWHM).

In the temperature region between 406 K and 870 K, the band gap fluctuations due to In-Ga disorder grow strongly with decreasing temperature. The experimental FWHM of 8 meV includes surface and volume defects that are not considered in the calculations. Nevertheless, the In-Ga disorder contributes significantly to band gap fluctuations.

For further analysis, clusters of In (Ga) are defined as a number of connected In (Ga) atoms. A low number of clusters with a high average cluster size is a sign for high disorder. Only clusters of the minority atom species are considered; Ga in In-rich CIGS and In in Ga-rich CIGS. Figure 4.5 shows the average number of clusters and cluster size for In-rich and Ga-rich CIGS. Data were taken at several temperatures between 290 K and 870 K. At all temperatures, the number of clusters is higher and the size of clusters is lower for In-rich CIGS, confirming the fact that Ga-rich CIGS is more disordered and inhomogeneous. The data show a continuous increase in the average number of clusters with temperature for both systems, apart from a small peak at 350 K (near the phase transition). The increase is rapid below 350 K and slower above 400 K. The average size of clusters shows the opposite trend: rapid decrease below 350 K, a dip at 350 K and a slower decrease above 400 K. The horizontal lines in both graphs mark the limits that were obtained in simulations with infinite temperature.

Calculations with larger simulation boxes ($24 \times 24 \times 12$ unit cells) show that finite size effects do not play a role for these results. The size of the clusters is independent of the volume, as is the ratio number of clusters : volume.

Conclusion

The MC simulations of $CuIn_xGa_{1-x}Se_2$ reveal strong fluctuations in the spatial In-Ga distribution, caused by a demixing transition near room temperature. The In-Ga disorder contributes significantly (up to 25%) to band gap fluctuations.

In-rich CIGS exhibits a higher homogeneity than Ga-rich CIGS at all considered temperatures between room temperature and the production temperature of solar cells. This is in agreement with the experiments of Gütay and Bauer [83]. The effect of cluster size dependence on Ga content provides a possible explanation for the relatively low efficiency of CIGS with high Ga content (low as compared to what could be excepted from their band-gap in the homogeneous case).

The results show that inhomogeneities become strongly pronounced as the material is slowly cooled down to room temperature, undergoing the demixing transition. The lack of phase separation in solar cells shows that

a)

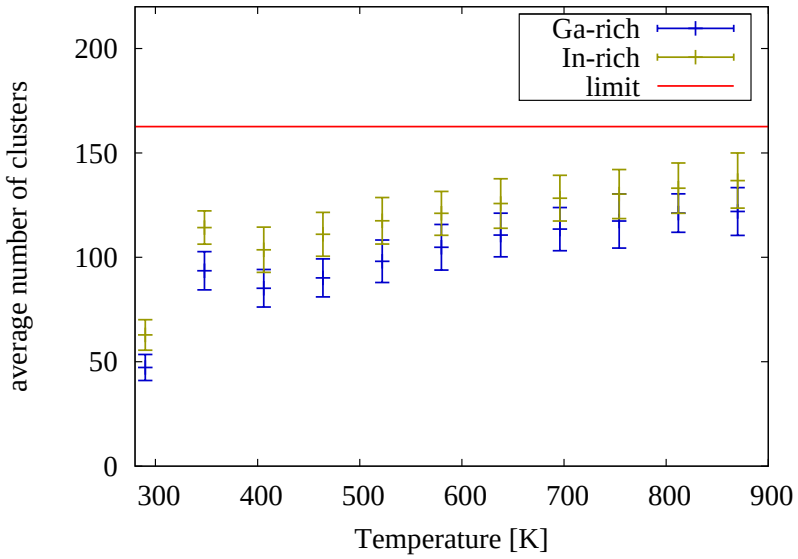

b)

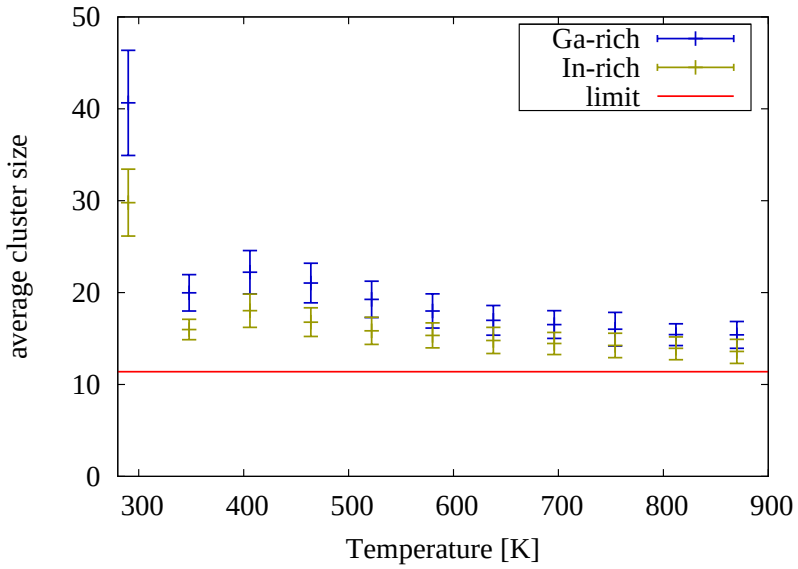

Figure 4.5: a) Average number of clusters and b) average cluster size for In-rich and Ga-rich CIGS for various temperatures. The red horizontal line marks the limit that was obtained in simulations with infinite temperature.

the In-Ga distribution is "frozen" in a high-temperature state. In order to minimise band gap fluctuations, a frozen state corresponding to a rather high temperature value is desirable. Thus, higher production temperatures and reasonably fast cooling will lead to better efficiencies which has recently been shown experimentally [84].

4.2 Cu-In-Vac Cluster Expansion

The following results were published in Physical Review B [85].

A (Cu,In,Vac)Se CE was created to investigate the Cu-poor stoichiometries of CIS. ATAT (cf. Section 3.1) was used to create 133 structures. The structures are up to two unit cells big (the unit cell structure is described in Section 2.3). In the following, unit cell always refers to the lattice sites of the 16-atom unit cell in Figure 2.3. Se is kept fixed and Ga is not considered. The remaining lattice sites can be occupied by Cu, In, or a vacancy. This changes the symmetry to $F\bar{4}3m$.

All generated structures lie on the Cu_2Se–In_2Se_3 tie-line and can be constructed from stoichiometric $CuInSe_2$ by removing n times three Cu atoms and adding n times one In atom. This defect complex is exceptionally stable, as was discussed in Section 2.3. More importantly, it keeps the number of valence electrons constant. This means that charges and the formation of dipoles do not have to be considered. The final CE includes 11 structures with $CuInSe_2$ stoichiometry, 63 structures with $Cu_5In_9Se_{16}$ stoichiometry, and 59 structures with $CuIn_5Se_8$ stoichiometry.

The total energies of all structures were calculated with the ab initio electronic structure programme QUANTUM ESPRESSO / PWSCF (cf. Section 3.3). The cut-off energy for the plane-waves was set to 70 Ry and a k-point grid of $3 \times 3 \times 3$ or bigger was used. The positions of all atoms were relaxed until the maximum force on atoms was less than $2 \cdot 10^{-3}$ rydberg/bohr and all three lattice parameters were relaxed until the pressure was less than 0.5 kbar.

The first structure studied is $CuInSe_2$ (cf. Figure 2.3). In Table 4.1, its calculated lattice constant (5.8612 Å), $\frac{c}{a}$ ratio (2.009), and anion displacement (0.217) are compared with values from literature and from ABINIT calculations. All values correspond favourably to literature.

The representative cluster figures of the CE fitted to the 133 PWSCF energies are given in Table 4.4. This CE is used for all MC simulations of Cu-poor CIS. For every representative, the clusters have to be created by applying the 64 symmetry operations of the 16-atom unit cell ($F\bar{4}3m$). The number of resulting clusters from one representative is equal to the multiplicity and the total number of distinct cluster figures is 841.

The cluster functions in Table 4.4 and Equation 2.28 are

$$\Theta_0(s_m) = -\cos(\frac{2}{3}\pi s_m) \tag{4.1}$$

$$\Theta_1(s_m) = -\sin(\frac{2}{3}\pi s_m), \tag{4.2}$$

Table 4.4: Representatives of cluster figures and ECIs for the (Cu,In,Vac)Se CE. Cluster functions are given for all coordinates in the respective line. Figures with an ECI of zero are not listed.

	Reduced coordinates	Multi-plicity	cluster functions	ECI [meV]
Empty figure	–	1	–	−546.827
Point figures	(1, 1, 1)	8	0	111.070
Pair figures	(1, 0.5, 0.75), (1.5, 0, 0.75)	16	0, 0	0.011117
	(1, 0.5, 0.75), (1.5, 0, 0.75)	32	1, 0	−0.058693
	(1, 0.5, 0.75), (1.5, 0, 0.75)	16	1, 1	0.182630
	(1, 1, 1), (1.5, 1, 1.25)	32	0, 0	−0.001612
	(1, 1, 1), (1.5, 1, 1.25)	64	1, 0	−0.059065
	(1, 1, 1), (1.5, 1, 1.25)	32	1, 1	0.183560
	(0.5, 1, 0.75), (1.5, 1, 0.75)	16	0, 0	6.399
	(0.5, 1, 0.75), (1.5, 1, 0.75)	32	1, 0	1.090
	(0.5, 1, 0.75), (1.5, 1, 0.75)	16	1, 1	52.347
	(1, 0.5, 0.75), (1, 0.5, 1.25)	8	0, 0	5.700
	(1, 0.5, 0.75), (1, 0.5, 1.25)	16	1, 0	−0.159
	(1, 0.5, 0.75), (1, 0.5, 1.25)	8	1, 1	49.034
	(1, 0.5, 0.25), (1.5, −0.5, 0)	64	0, 0	−1.826
	(1, 0.5, 0.25), (1.5, −0.5, 0)	64	1, 0	−3.774
	(1, 0.5, 0.25), (1.5, −0.5, 0)	64	1, 1	13.868
	(0.5, 1, 0.75), (1, 1.5, 0.25)	32	0, 0	−0.158
	(0.5, 1, 0.75), (1, 1.5, 0.25)	32	1, 0	−1.009
	(0.5, 1, 0.75), (1, 1.5, 0.25)	32	1, 1	11.234
Triple figures	(1, 1, 1), (1.5, 1.5, 1), (1.5, 1, 1.25)	32	0, 0 0	−3.026
	(1, 1, 1), (1.5, 1.5, 1), (1.5, 1, 1.25)	64	1, 0 0	−4.890
	(1, 1, 1), (1.5, 1.5, 1), (1.5, 1, 1.25)	32	1, 1 0	−26.996
	(1, 1, 1), (1.5, 1.5, 1), (1.5, 1, 1.25)	32	0, 0 1	6.230
	(1, 1, 1), (1.5, 1.5, 1), (1.5, 1, 1.25)	64	1, 0 1	−25.099
	(1, 1, 1), (1.5, 1.5, 1), (1.5, 1, 1.25)	32	1, 1 1	−47.214

with the lattice site occupation s_m being equal to 0 for Cu, 1 for In, and 2 for Vac.

The (Cu,In,Vac)Se CE not only includes the configurational energy $\delta E_{UR}(\mathbf{s}^m, V)$ of Equation 2.32, but also includes the relaxation terms $\delta E_C(\mathbf{s}^m, V)$, $\delta E^{int}_{A,B}(\mathbf{s}^m, V)$, and $\delta E^{ext}(\mathbf{s}^m, V)$. This is due to the fact that all atoms and lattice vectors were relaxed in the PWSCF calculations. The volume deformation energy $\Delta E_{VD}(x, \mathbf{s}^m)$ was neglected to keep the calculation time reasonable.

The generation of structures with ATAT was only possible up to a certain point. The generation of further structures took an unreasonably long time. Additional structures were created by hand.

For an accurate CE, it is especially important to correctly predict the energies of low energy structures because these structures will most likely occur in the MC simulations. Such structures were identified by simulated annealing with the MC method.

First, a preliminary CE is created from the structures generated by hand and with ATAT. Then for simulated annealing, a MC simulation is started with an arbitrary $6 \times 6 \times 6$ unit cell configuration and at a high temperature. The system is slowly cooled down and, at low temperatures, finds itself in a low-energy state. Local, low-energy structures that are compatible with the periodic boundary conditions are identified. They are subsequently calculated ab initio and used to improve the CE. With the improved CE, the process is repeated until no new low-energy structure can be identified.

By using the abovementioned iterative approach to create the CE, eight noteworthy $CuIn_5Se_8$ structures with low energies were found (cf. Figures 4.6 and 4.7). Six of these structures were mentioned before in [18], where they are denoted as Type-A - Type-F. Of these six—the one with the lowest energy (Type-D)—had already been discovered in 1997 by Zhang, Wei, and Zunger [10].

Table 4.5 shows the energies for the eight low-energy $CuIn_5Se_8$ structures. The ab initio energies agree well with the energies from [18] and the ordering with respect to the energy is correctly reproduced. An additional two structures with low energy are found. The first one (New-1) has the lowest energy of all eight structures and $P\bar{4}n2$ symmetry. The energy of New-1 is about 0.2 meV/atom lower than that of the Type-D structure.

The energies from the CE do not yield the same order as the ab initio energies, but the state with the lowest energy is correctly predicted and the structures Type-C, Type-D, New-1, and New-2 with particularly low energy are distinguished from the structures Type-A, Type-B, Type-E, and Type-F with higher energy.

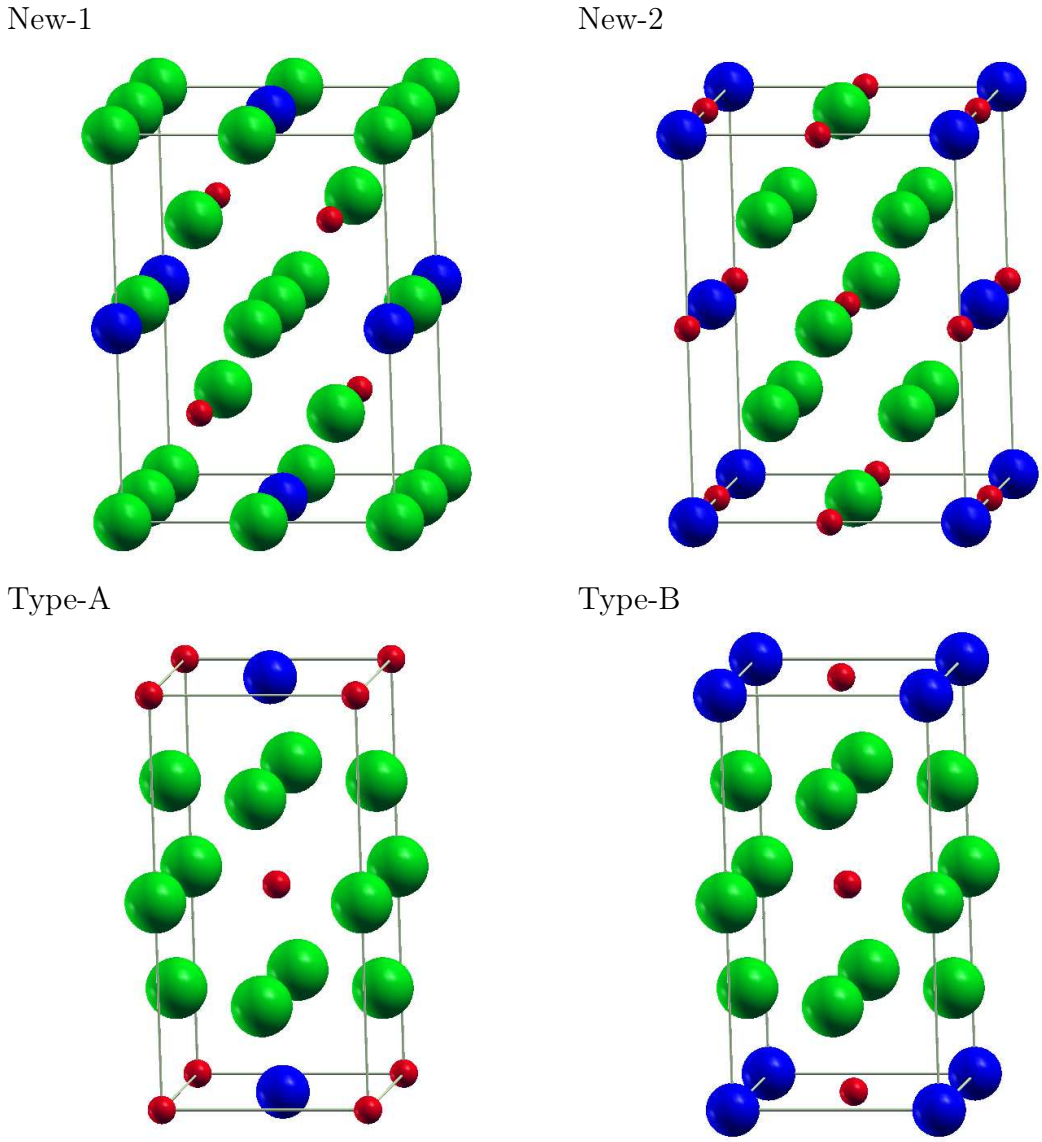

Figure 4.6: Low-energy crystal structures of $CuIn_5Se_8$. Cu atoms are blue spheres, In atoms are green spheres, and vacancies are small red spheres. Se atoms are not shown.

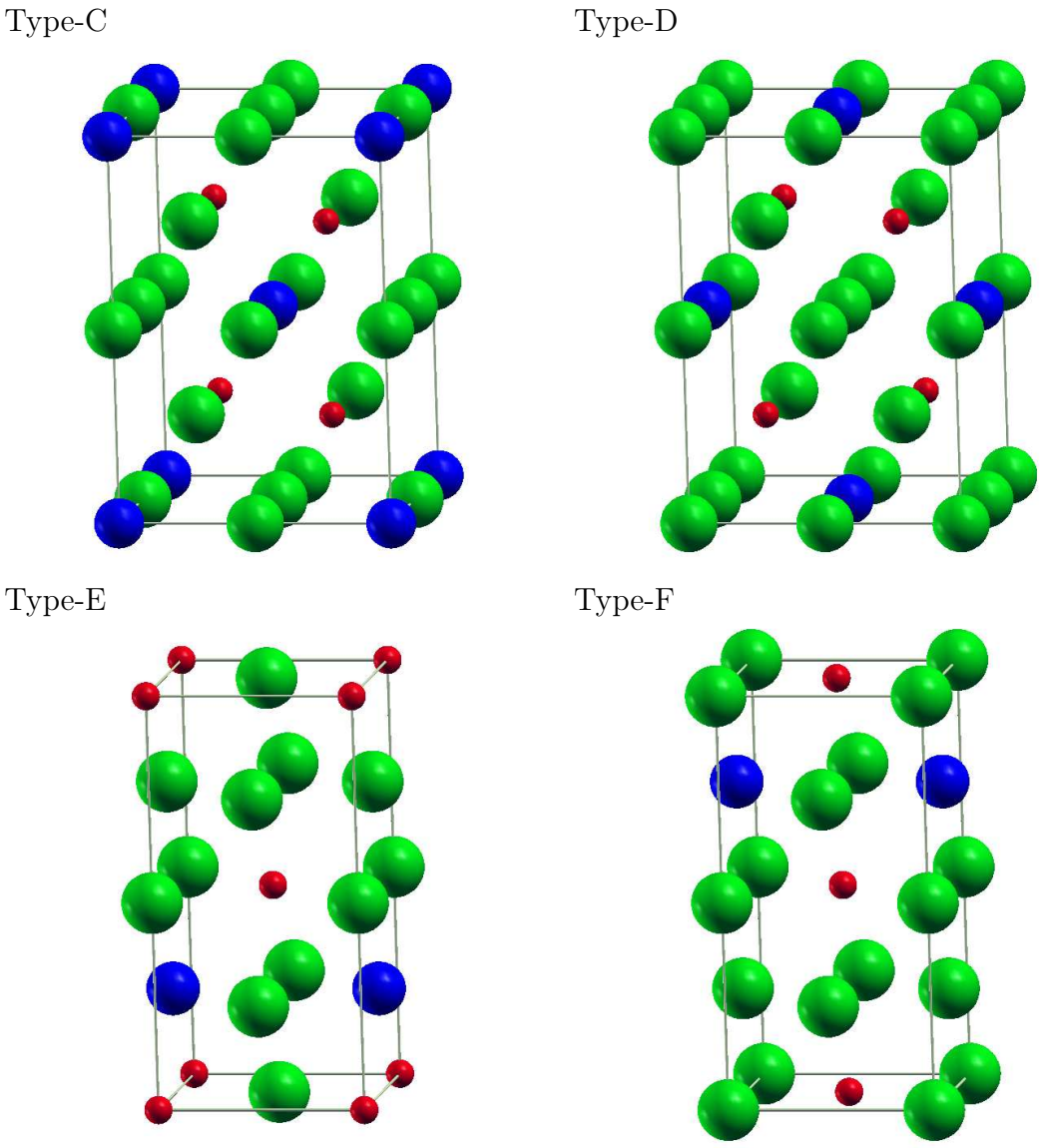

Figure 4.7: Low-energy crystal structures of $CuIn_5Se_8$. Cu atoms are blue spheres, In atoms are green spheres, and vacancies are small red spheres. Se atoms are not shown.

Table 4.5: Energies for eight low-energy $CuIn_5Se_8$ structures (cf. Figures 4.6 and 4.7). The energies are given relative to the energy of Type-D.

Structure	Energy in [18] [meV/atom]	Ab initio energy [meV/atom]	CE energy [meV/atom]
Type-A	4	4.7	5.7
Type-B	4	5.9	7.3
Type-C	1	2.9	0.4
Type-D	0	0.0	0.0
Type-E	6	10.1	5.9
Type-F	8	12.1	7.7
New-1	-	−0.2	−1.3
New-2	-	1.2	−0.2

4.2.1 Canonical Monte Carlo for $CuIn_5Se_8$

At low temperatures, $CuIn_5Se_8$ forms an ordered defect structure with a tetragonal unit cell. At high temperatures, the material becomes disordered. This is an important observation, because disorder will influence the electronic properties and thus the solar cell performance.

The order-disorder transition can be observed in several observables. In the following, the nearest neighbour (NN) pair correlations and the configurational energy of the system are discussed.

The z-axis of the coordinate system is parallel to the long axis of the tetragonal unit cell. A Cu atom in the CIS structure has 12 NNs, 4 in the x–y plane and 8 in the planes above and below. a_z is defined as the fraction of In atoms on the 8 NN sites in the planes above and below. The fraction of In atoms on the 4 NN sites in the x–y plane is denoted by a_{xy}.

The behaviour of a_{xy}, a_z, and the configurational energy U has been studied with MC simulations of $12 \times 12 \times 6$ tetragonal 16-atom unit cells at different temperatures (Figure 4.8). Starting with an ordered structure at $T = 220$ K, the temperature was increased stepwise to $T = 325$ K.

At low temperatures, a_{xy} is equal to 1, meaning that all Cu atoms are surrounded by four In atoms in the x–y plane. In the same temperature regime, a_z is equal to 0.5, which means that four of the eight corresponding NNs are In atoms. The energy U is approximately 20 eV.

At $T \approx 300$ K, the three quantities change rapidly as the system switches to a disordered phase. a_{xy} drops from 1 to about 0.6 and a_z increases from 0.5 to 0.7, indicating that the order around Cu atoms changes drastically. As the temperature is decreased, the system returns to the ordered state at $T \approx 250$ K, so that the system shows a strong hysteresis.

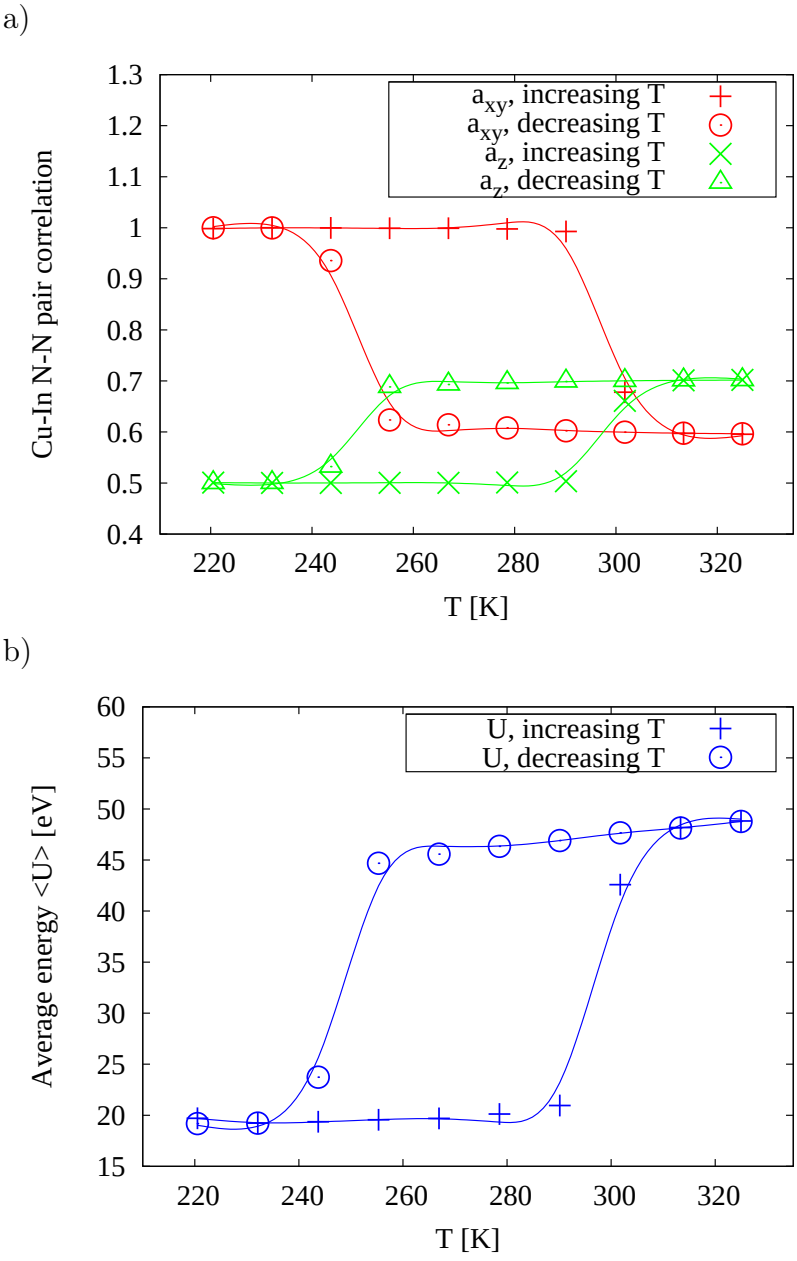

Figure 4.8: a) Average pair correlation functions a_{xy} and a_z, and b) average configurational energy $\langle U \rangle$ of $CuIn_5Se_8$ for increasing and decreasing temperature T. The low-temperature phase is ordered, the high-temperature phase is disordered. Cubic splines have been fitted to the data to guide the eye.

The order around the Cu atoms can be analysed more closely. Figure 4.9 shows the average number of Cu atoms in the simulation volume that have a very specific environment around them. They have four In atoms as NNs in the x–y plane and the remaining NN are four In atoms and four vacancies. The six atoms in the next-NN shell are all In atoms. This ordering is called environment I. It is the characteristic Cu environment of the low-energy structures Type-D and New-1 in Figures 4.6 and 4.7.

At low temperatures, all 864 Cu atoms in the simulation volume show the same ordering (environment I), which leads to a minimal configurational energy. The number decreases to approximately 300 at $T \approx 300$ K when increasing the temperature, and increases back up to 864 at $T \approx 250$ K when decreasing the temperature. In the disordered phase, a high number of Cu atoms is not surrounded by environment I, but by a mix of other environments that lead to higher energies.

The hysteresis prevents us from directly measuring the transition temperature T_0 of the ordered and the disordered phase. The exact T_0 can be determined by analysing the free energy of the system with multi-histogram simulations (cf. Section 2.5.3).

The multi-histogram simulations use 10^6 MC sweeps and a simulation volume of $6 \times 6 \times 6$ tetragonal 16-atom unit cells. The configurational energy U of the ordered phase is approximately 5 eV and that of the disordered phase is 11.5 eV. The value of U unambiguously determines the order of a configuration. For this reason, U was chosen as an order parameter. Simulations were carried out with the parabolic bias potential $U_{\text{bias}} = a(U - U_i)^2$. U_i was varied from 5 eV to 13 eV in steps of 0.5 eV. The parameter a was selected at 0.8 $\frac{1}{\text{eV}}$, which keeps the energy of the system within the vicinity of U_i and leads to an overlap of successive runs.

Figure 4.10 shows the results of the MC simulations. The curve fragments are from MC runs with different parabola minima U_i. Configurations with a lower energy than that of the ordered state are not possible which is why the plots end abruptly at $U = 5$ eV.

At a temperature of 267 K, the state with the lower configurational energy $U = 5$ eV (ordered state) has a lower free energy than the disordered state with $U = 11.5$ eV [Figure 4.10 a)]. The ordered state is stable and the disordered state is metastable. At a temperature of 290 K, the situation is reversed [Figure 4.10 c)]. The disordered state has a lower free energy than the ordered state and is thus stable, while the ordered state is metastable. At 279 K, both states have the same free energy and are equally likely [Figure 4.10 b)]. $T_0 = 279$ K is the order-disorder transition temperature.

It is noteworthy that $T_0 = 279$ K is below the typical temperature of solar cells in operation. Consequently, the absorber material of solar cells

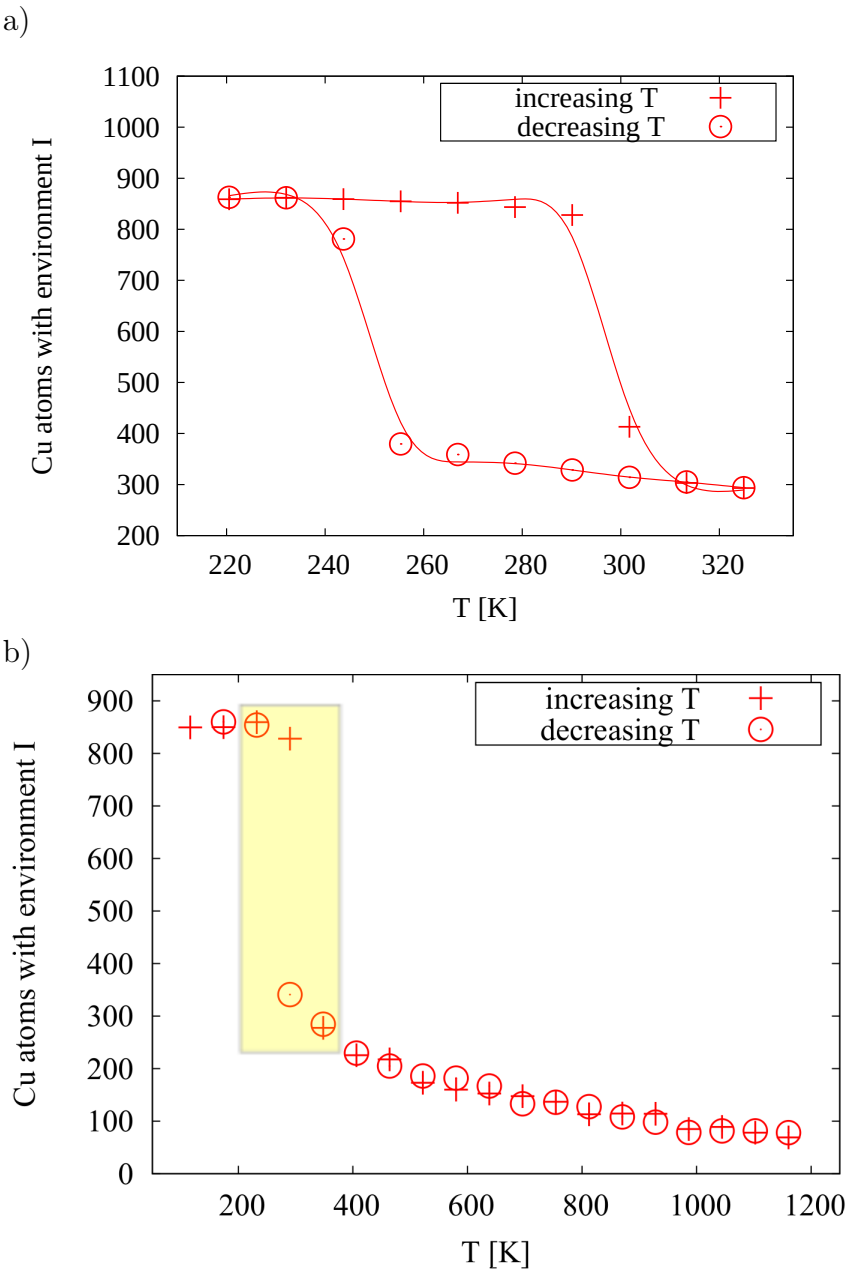

Figure 4.9: Average number of Cu atoms in $CuIn_5Se_8$ with environment I (see text for definition) for increasing and decreasing temperature T. a) Hysteresis region. The low-temperature phase is ordered and all 864 Cu atoms have the same environment. The high-temperature phase is disordered. Only some Cu atoms retain environment I. Cubic splines have been fitted to the data to guide the eye. b) The yellow area marks the hysteresis region. Above the transition temperature, the number of Cu atoms with environment I decreases continuously with temperature.

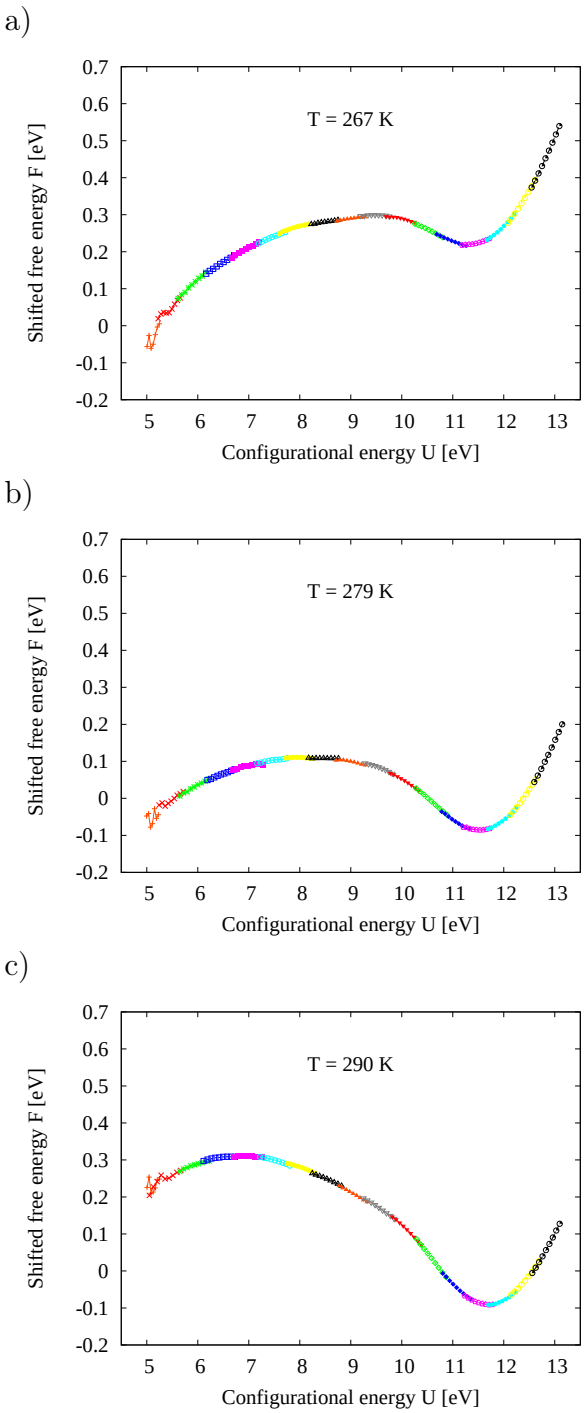

Figure 4.10: Results of multi-histogram simulations for the free energy F as a function of the configurational energy U. The curve fragments of F from different runs are shifted vertically to produce a smooth function. a) 267 K: Global minimum at low configurational energy. b) 279 K: Both minima are of equal depth and both states are equally likely. c) 290 K: Global minimum at high configurational energy.

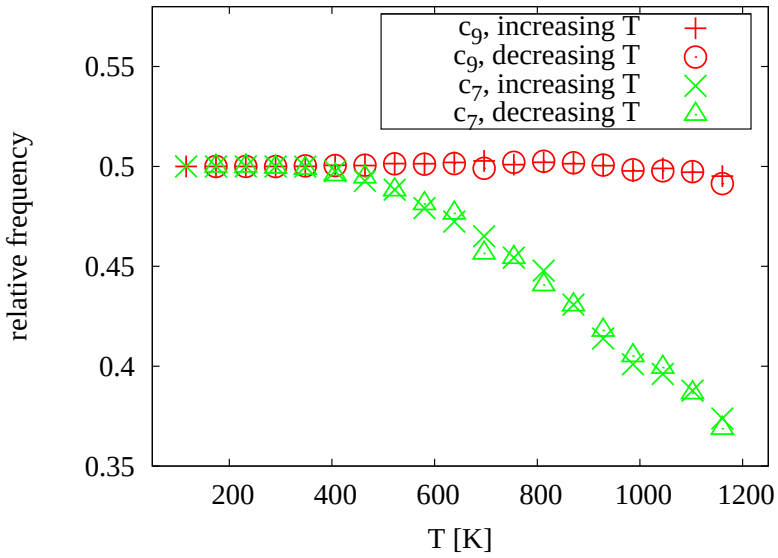

Figure 4.11: Average frequency of $k = 7$ tetrahedra (c_7) and $k = 9$ tetrahedra (c_9) for increasing and decreasing temperature. Above $T = 300$ K, c_7 decreases continuously with temperature, while c_9 stays almost constant.

will only contain disordered defect structures. However, interface and grain boundary effects are not included in the simulations. They might influence T_0 in experiment.

In the ordered $CuIn_5Se_8$ phase below the transition temperature T_0, the distribution of local tetrahedra around Se atoms (cf. Section 2.3) matches the results of Zhang, Wei, and Zunger [10]. The fraction of $k = 7$ clusters (Vac + Cu + 2 In) will be denoted as c_7 and the fraction of $k = 9$ clusters (Vac + 3 In) as c_9. In the ordered phase, $c_7 = 0.5$ and $c_9 = 0.5$.

Figure 4.11 shows results of simulations with $12 \times 12 \times 6$ tetragonal 16-atom unit cells. In the disordered state, c_7 becomes temperature dependent. At $T \approx 300$ K, c_7 and c_9 are 0.5. At higher temperatures, c_7 decreases continuously with temperature, while c_9 stays almost constant. When comparing the results for a run with increasing temperature and a run with decreasing temperature, no difference can be observed.

At the first order phase transition, the pair correlation functions a_{xy}, a_z, and the configurational energy U change discontinuously, while the tetrahedra frequencies c_7 and c_9 do not change notably. This indicates that the clusters of atoms around Se are more stable than the clusters of atoms around Cu and that the system retains a certain degree of order up to high temperatures.

The last conclusion is backed by data of the Cu environment from the same MC runs (Figure 4.9). At temperatures above the order-disorder transition, the number of Cu atoms with environment I decreases continuously with temperature from about 250 to below 100. This behaviour is similar to that of the tetrahedron frequency c_7.

Conclusion

The canonical MC simulations have revealed several interesting facts.

1. The first order phase transition temperature from ordered to disordered $CuIn_5Se_8$ is $T_0 = 279$ K. It has been determined through multi-histogram simulations.

2. Above the order-disorder transition the system retains a certain degree of order. This degree of order decreases continuously, as can be observed in the frequency of $k = 7$ tetrahedra around Se atoms and in the frequency of Cu environments corresponding to the $CuIn_5Se_8$ structure with the lowest energy.

3. When increasing/decreasing the temperature, the order-disorder transition shows a strong hysteresis between 250 K and 300 K.

4.2.2 Canonical Monte Carlo for $CuIn_3Se_5$

$CuIn_3Se_5$ is a compound that has been investigated experimentally [18, 48, 55], but ab initio computer simulations are difficult due to the necessity of a large unit cell with 80 atoms (cf. Section 2.3). MC simulations on the basis of a CE are however feasible.

Figure 4.12 displays the results of canonical MC simulations with a simulation volume of $10 \times 10 \times 5$ tetragonal 16-atom unit cells and a $CuIn_3Se_5$ stoichiometry. The two simulation runs started with the same configuration and differ only by the seed of the random number generator.

The red data points show a quick relaxation to an ordered state. This state can be characterised by the neighbours of the Cu atoms (pair correlations). Table 4.6 lists the Cu environments in ordered $CuIn_3Se_5$ and $CuIn_5Se_8$. The NNs in the x–y plane are 4 In atoms for both cases. In the planes above and below, both the 8 NNs and the 6 next-NNs are different.

The second MC simulation with the green data points in Figure 4.12 shows a different behaviour. Even though the energy fluctuates strongly at all considered temperatures, the system is stuck in a metastable state and

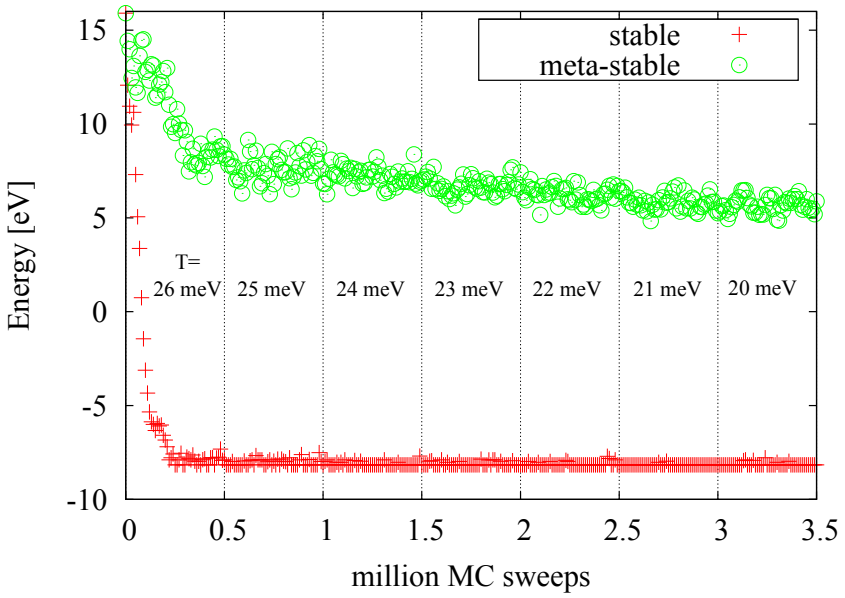

Figure 4.12: Configurational energy of $CuIn_3Se_5$ from two MC runs that differ only by the seed of the random number generator. The temperature was decreased every 10^5 MC sweeps.

does not reach the low-energy state. The types of neighbour atoms fluctuate and differ greatly from the ones in the low-energy simulation.

The frequencies of tetrahedra around Se atoms for $CuIn_3Se_5$ is $c_7 = 40\%$, $c_8 = 20\%$, and $c_9 = 40\%$ (cf. Section 2.3). c_8 is the frequency of $k = 8$ tetrahedra. This result is identical for the metastable high-energy state and for the low-energy state and it is in agreement with literature [11].

Table 4.6: Number and type of neighbours of Cu atoms in low-energy, ordered $CuIn_3Se_5$ and $CuIn_5Se_8$.

Type of neighbour	Number of Cu neighbours in	
	$CuIn_3Se_5$	$CuIn_5Se_8$
NNs in x–y plane	4 In	4 In
NNs below/above x–y plane	2 Cu, 4 In, 2 Vac	4 In, 4 Vac
next-NN	0.1 Cu, 3.95 In, 1.95 Vac	6 In

Conclusion

Configurations with $CuIn_3Se_5$ stoichiometry have not been included explicitly in the CE due to the required big size of the unit cell. This makes it difficult to find an ordered ground state and leads to non-ergodicity, a common problem in MC simulations. Therefore, all results of simulations with a $CuIn_3Se_5$ stoichiometry have to be interpreted with care.

4.2.3 Grand-Canonical Monte Carlo

The following section will answer the question under which conditions the $CuIn_3Se_5$ and the $CuIn_5Se_8$ stoichiometries are achieved. A method to determine the chemical potentials for a given stoichiometry is the particle insertion method (often referred to as the Widom method [86]). In this method, the energy gain for a particle insertion is sampled in thermal equilibrium.

When using the particle insertion method, a canonical MC simulation is run. In addition to the usual MC moves, test particles are added to the system. In this step, a random vacancy is chosen and either Cu or In is inserted temporarily. The energy before (U_0) and after the insertion (U_1) is calculated and the Boltzmann factor

$$w_i = \mathrm{e}^{-\beta(U_1-U_0)} \tag{4.3}$$

is calculated for test insertion i. w_i gives the acceptance probability of the insertion. Then, before the MC simulation continues, the test particle is removed. While sampling thermal equilibrium, the probabilities w_i are summed up for Cu and In independently.

$$W_{\mathrm{Cu}} = \sum_i w_i\,, \quad \text{sum over all } i \text{ where Cu was inserted and} \tag{4.4}$$

$$W_{\mathrm{In}} = \sum_i w_i\,, \quad \text{sum over all } i \text{ where In was inserted.} \tag{4.5}$$

If N_{Cu} is the number of Cu insertions and N_{In} is the number of In insertions, then the ratios $\frac{W_{\mathrm{Cu}}}{N_{\mathrm{Cu}}}$ and $\frac{W_{\mathrm{In}}}{N_{\mathrm{In}}}$ give the average acceptance probability of a Cu/In insertion. The following discussion will show how to relate the fraction $\frac{W}{N}$ to chemical potentials.

Let γ^N be a state with N particles. An insertion leads to γ^{N+1}, a state with $N+1$ particles. The total differential of the free energy is

$$\mathrm{d}F = -S\mathrm{d}T - p\mathrm{d}V + \mu\mathrm{d}N. \tag{4.6}$$

Accordingly, the chemical potential is given by

$$\mu = \frac{\mathrm{d}F}{\mathrm{d}N} \approx \frac{F(\gamma^{N+1}) - F(\gamma^N)}{\Delta N}. \tag{4.7}$$

$F(\gamma^N)$ is the free energy of the state with N particles and $\Delta N = +1$. In the case of high N, the difference quotient is a good approximation to the derivation. Using Equation 2.19 leads to

$$\begin{aligned} \mu &= F(\gamma^{N+1}) - F(\gamma^N) \\ &= -k_B T \ln Z(\gamma^{N+1}) + k_B T \ln Z(\gamma^N) \\ &= -k_B T \ln \frac{Z(\gamma^{N+1})}{Z(\gamma^N)} \\ \mathrm{e}^{-\beta\mu} &= \frac{Z(\gamma^{N+1})}{Z(\gamma^N)}, \end{aligned} \tag{4.8}$$

where $\beta = \frac{1}{k_B T}$ as usual.

Let Z_1^{id} be the partition function of one particle in an ideal gas reservoir. It follows

$$\begin{aligned} \mathrm{e}^{-\beta\mu} &= \frac{Z_1^{id} Z(\gamma^{N+1})}{Z_1^{id} Z(\gamma^N)} \\ \mathrm{e}^{-\beta(\mu + k_B T \ln Z_1^{id})} &= \frac{Z(\gamma^{N+1})}{Z_1^{id} Z(\gamma^N)}. \end{aligned} \tag{4.9}$$

$\mu_0 := -k_B T \ln Z_1^{id}$ is the ideal part of the chemical potential. It provides a constant shift of the chemical potential values.

The partition functions can be expressed as integrals

$$\begin{aligned} \mathrm{e}^{-\beta(\mu-\mu_0)} &= \frac{\int \mathrm{d}\mathbf{r}^{N+1}\, \mathrm{e}^{-\beta U(\gamma^{N+1})}}{\int \mathrm{d}\mathbf{r} \int \mathrm{d}\mathbf{r}^N\, \mathrm{e}^{-\beta U(\gamma^N)}} \\ &= \left\langle \frac{\int \mathrm{d}\mathbf{r}\, \mathrm{e}^{-\beta\Delta U}}{\int \mathrm{d}\mathbf{r}\, 1} \right\rangle_N. \end{aligned} \tag{4.10}$$

$U(\gamma^N)$ is the configurational energy of the system with N particles and ΔU is the energy gain due to the particle insertion. In a system with discrete lattice sites, the integrals become sums over all lattice sites. MC simulations do not evaluate the sum directly, but sample the lattice sites statistically.

The numerator of Equation 4.10 can be determined by simple sampling and is proportional to W in Equation 4.4 for large N and high numbers of MC

sweeps. The denominator is proportional to the number of test insertions. Hence, the fraction in Equation 4.10 is equal to $\frac{W_{\mathrm{Cu/In}}}{N_{\mathrm{Cu/In}}}$ and with $\mu_{\mathrm{Cu/In}} = (\mu - \mu_0)$, the chemical potentials can be calculated by

$$\beta\mu_{\mathrm{Cu}} = -\ln\frac{W_{\mathrm{Cu}}}{N_{\mathrm{Cu}}} \quad \text{and} \tag{4.11}$$

$$\beta\mu_{\mathrm{In}} = -\ln\frac{W_{\mathrm{In}}}{N_{\mathrm{In}}}. \tag{4.12}$$

In a grand-canonical MC simulation with these values for the chemical potentials, there is no preference for adding or removing a particle and the average stoichiometry will be constant.

The equilibrium chemical potentials in $CuIn_3Se_5$ and $CuIn_5Se_8$ have been determined after relaxing the system for 10^6 MC sweeps and averaging over the next $6 \cdot 10^5$ sweeps. The determined values are

$$CuIn_3Se_5 : \mu_{\mathrm{Cu}} = (0.73 \pm 0.01)\ \mathrm{eV} \quad \mu_{\mathrm{In}} = (2.21 \pm 0.01)\ \mathrm{eV}, \tag{4.13}$$

$$CuIn_5Se_8 : \mu_{\mathrm{Cu}} = (0.57 \pm 0.01)\ \mathrm{eV} \quad \mu_{\mathrm{In}} = (1.94 \pm 0.01)\ \mathrm{eV}. \tag{4.14}$$

The scheme can be modified to calculate the equilibrium chemical potentials for $CuInSe_2$. Due to the lack of vacancies in stoichiometric $CuInSe_2$, atom removals have to be used instead of insertions. The calculation yields

$$CuInSe_2 : \mu_{\mathrm{Cu}} = (0.79 \pm 0.01)\ \mathrm{eV} \quad \mu_{\mathrm{In}} = (2.36 \pm 0.01)\ \mathrm{eV}. \tag{4.15}$$

The chemical potentials measured in experiment correspond to those used in the MC calculations up to a constant that depends on the DFT method[62]. Thus, the positive values of the chemical potentials do not imply instability of the material.

To find other equilibrium stoichiometries for different chemical potentials, grand-canonical MC simulations were performed. During the simulations, the number of Cu and In atoms is changed independently. Accordingly, the number of vacancies in the system changes. The energy costs of removing a Cu (In) atom is given by the chemical potential μ_{Cu} (μ_{In}) and the configurational enerrgy difference. Se atoms are kept fixed at their lattice sites which corresponds to a high μ_{Se}. Since the number of Se atoms does not change throughout the simulations, values for atomic concentration refer only to the cation sites. For instance, c(Cu) denotes the fraction of cation sites occupied by Cu. The sum of c(Cu), c(In), and c(Vac) is equal to 1.

After choosing fixed chemical potential values for the reservoirs of Cu and In, the system assumes a stoichiometry that is in equilibrium with the reservoirs. In experiments (e.g. a physical vapor deposition process), the different chemical potentials can be realized by adjusting the partial vapor pressures for the elements. Dynamical effects in this type of process are neglected in our simulations.

In a first step, a fine μ-mesh of chemical potentials was defined. The range of this mesh is $\mu_{\mathrm{Cu}} \in [-0.7\ \mathrm{eV}, 1.8\ \mathrm{eV}]$ and $\mu_{\mathrm{In}} \in [-0.2\ \mathrm{eV}, 3.2\ \mathrm{eV}]$ and the step size is 0.02 eV. This produces a total of 21546 μ-mesh points. A grand-canonical MC simulation was performed for each of these points, using an ordered low-energy $CuIn_5Se_8$, $CuIn_3Se_5$, or $CuInSe_2$ structure as starting configuration. A simulation volume of $6 \times 6 \times 6$ tetragonal 16-atom unit cells was used for $CuIn_5Se_8$ and $CuInSe_2$ starting configurations. The $CuIn_3Se_5$ simulations use a volume of $10 \times 10 \times 5$ tetragonal 16-atom unit. The increased volume compared to the simulations with a $CuIn_5Se_8$ and $CuInSe_2$ starting configuration is necessary to allow an exact $CuIn_3Se_5$ stoichiometry.

The number of MC sweeps per run was chosen to be only 1000 which makes the total number of 21546000 MC sweeps for the whole μ-mesh feasible. An increase of the number of MC sweeps is desirable, but greatly increases the time needed for the calculations.

The simulations are suitable for determining the stoichiometry for a set of chemical potentials because the stoichiometry of a single grand-canonical simulation generally converges very rapidly. The MC runs are however too short to be used for sampling other observables in thermal equilibrium.

Figures 4.13 and 4.14 illustrate the quick convergence of the concentrations towards an equilibrium value for three different pairs of chemical potentials. The starting configuration was chosen to be $CuIn_5Se_8$ and the temperature was set to 174 K. The equilibrium stoichiometries are reached well within 1000 MC sweeps. No change of these stoichiometries was observed within the next 10^6 sweeps.

Exceptions to the quick convergence are the $CuIn_3Se_5$ and the $CuIn_5Se_8$ stoichiometries. The non-ergodicity of canonical $CuIn_3Se_5$ simulations was already discussed in Section 4.2.2. Further effects will be discussed in the following sections.

$CuIn_5Se_8$ Starting Configuration

Figure 4.15 a) shows the concentration landscape that was calculated with a $CuIn_5Se_8$ starting configuration for a section of the μ-mesh at a temperature

a)

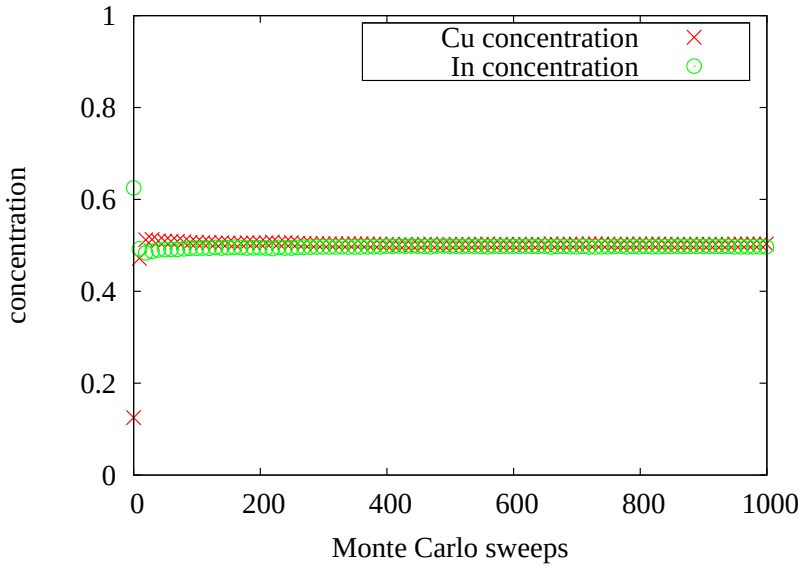

b)

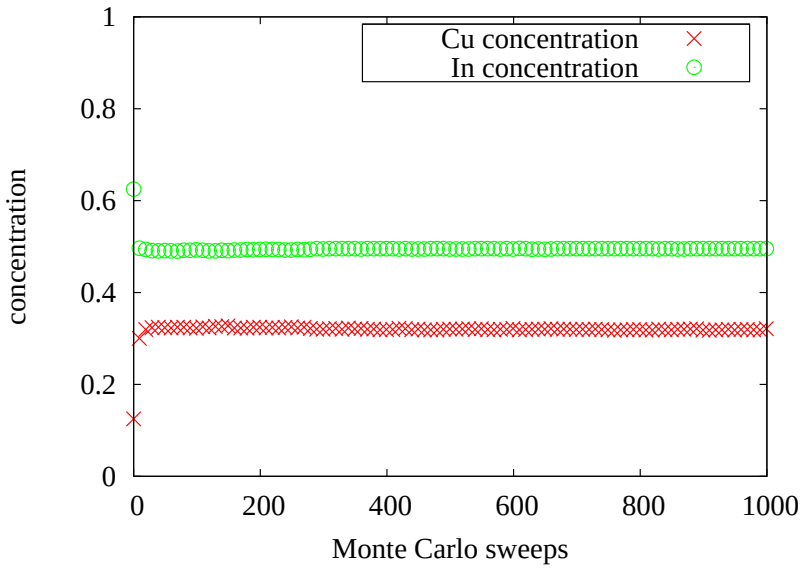

Figure 4.13: Cu and In concentration for typical chemical potentials resulting in a) $CuInSe_2$ ($\mu_{Cu} = 1.0$ eV, $\mu_{In} = 2.4$ eV) and b) $Cu_{0.31}In_{0.50}Se_{1.00}$ ($\mu_{Cu} = 0.5$ eV, $\mu_{In} = 1.5$ eV). The concentrations relax to an equilibrium value well within 1000 MC sweeps. The starting configuration was $CuIn_5Se_8$.

a)

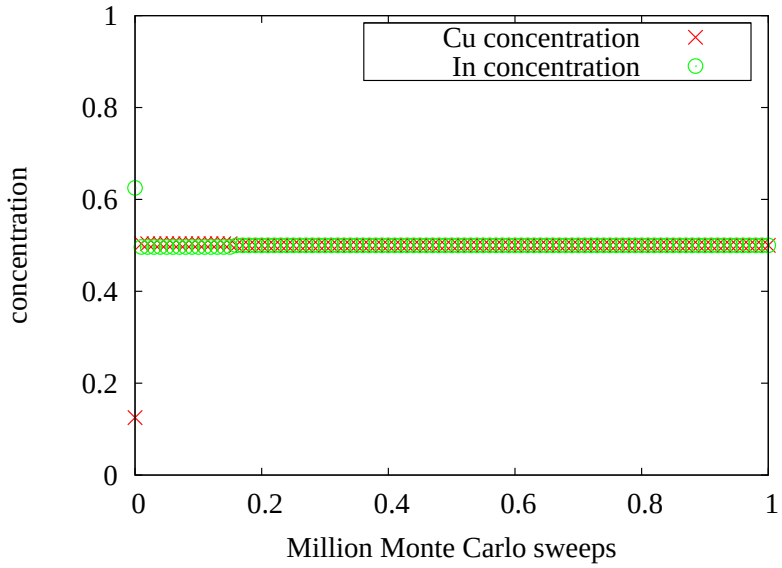

b)

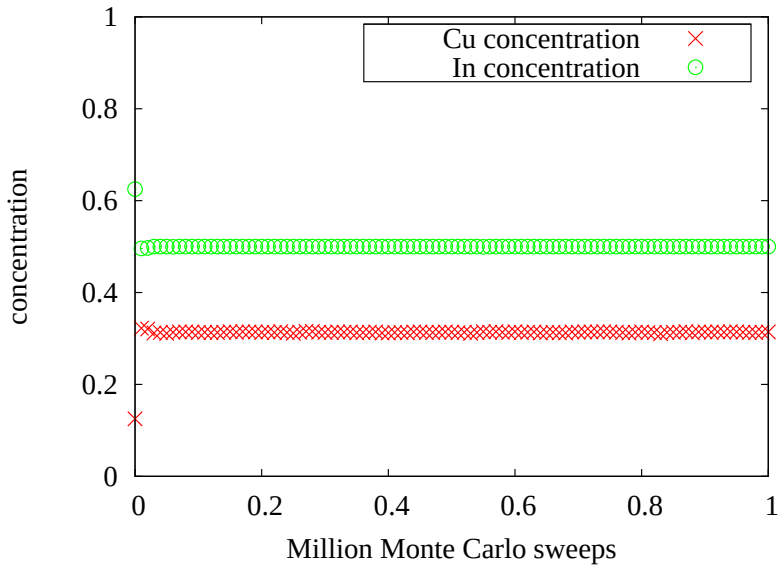

Figure 4.14: Cu and In concentration for typical chemical potentials resulting in a) $CuInSe_2$ ($\mu_{Cu} = 1.0$ eV, $\mu_{In} = 2.4$ eV) and b) $Cu_{0.31}In_{0.50}Se_{1.00}$ ($\mu_{Cu} = 0.5$ eV, $\mu_{In} = 1.5$ eV). No significant change in the concentrations is visible beyond 1000 MC sweeps. Only every 1000^{th} data point is plotted.

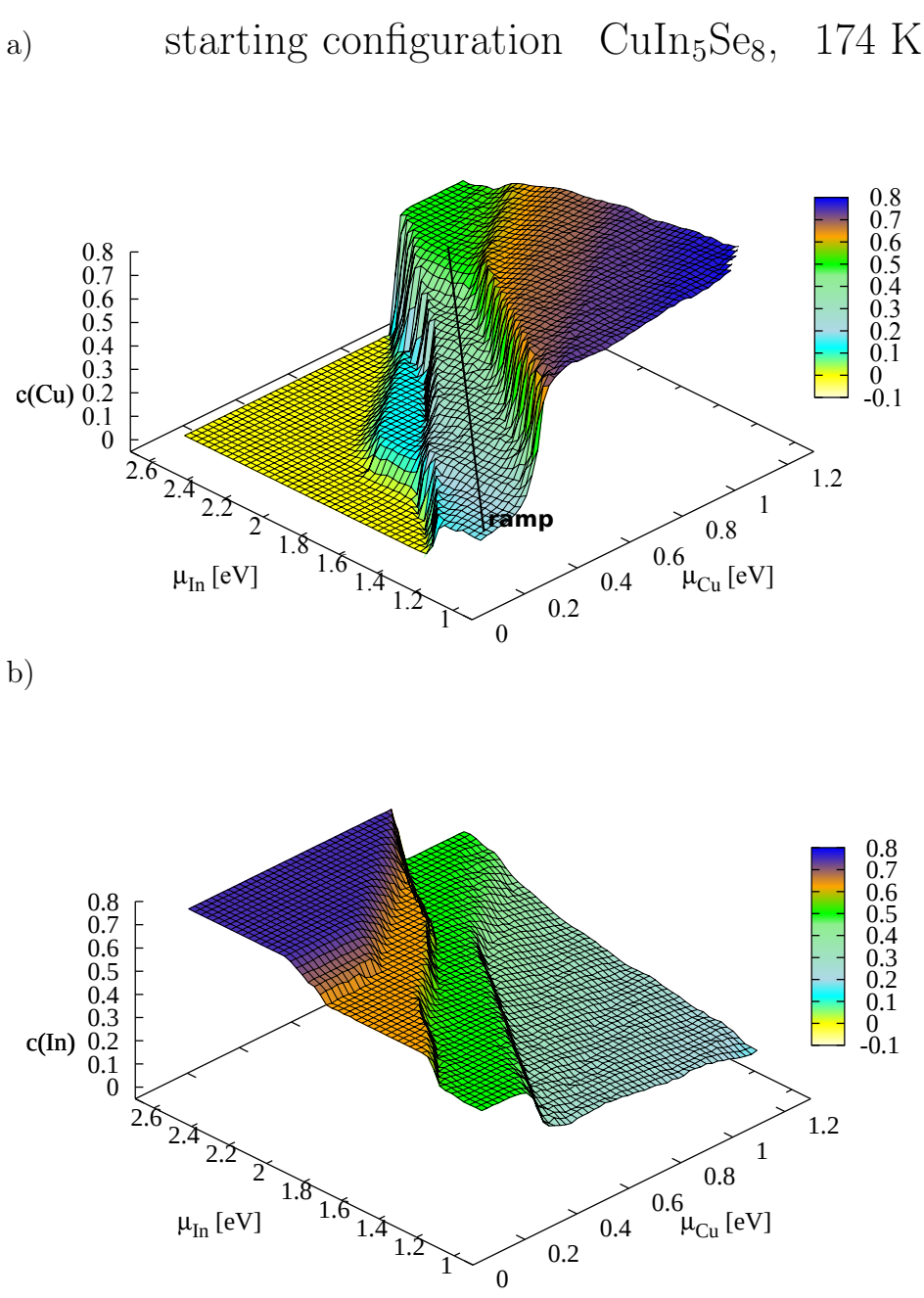

Figure 4.15: Landscape of the a) Cu concentration and b) In concentration versus the chemical potentials at $T = 174$ K with a $CuIn_5Se_8$ starting configuration. Chemical potential values from simulations correspond to the values measured in experiment up to a constant. Positive values do not imply instability.

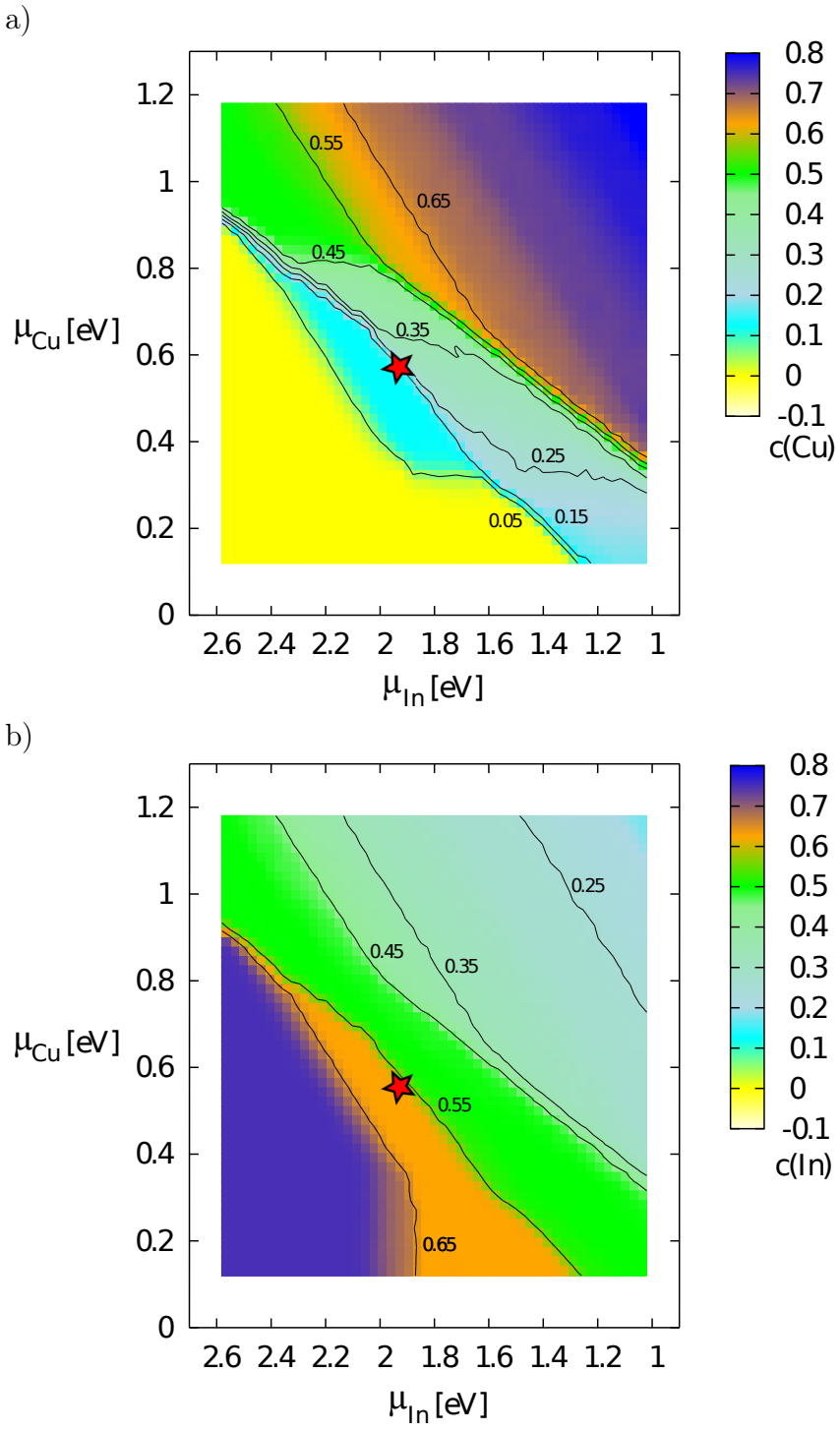

Figure 4.16: Contour plot of the a) Cu concentration and b) In concentration versus the chemical potentials at $T = 174$ K with a $CuIn_5Se_8$ starting configuration. The red star marks the equilibrium chemical potentials for $CuIn_5Se_8$ that have been determined with the particle insertion method. Chemical potential values from simulations correspond to the values measured in experiment up to a constant. Positive values do not imply instability.

of 174 K. At this low temperature, the configurational energy is dominant and structures are very sharp. Blurring effects due to temperature are suppressed.

The concentration of Cu is plotted against the chemical potentials μ_{Cu} and μ_{In}. The concentration $c(\mathrm{Cu})$ denotes the fraction of cation sites occupied by Cu. The In concentration $c(\mathrm{In})$ is plotted in the same way in Figure 4.15 b). The same data are displayed in contour plots in Figures 4.16 a) (Cu) and 4.16 b) (In).

For low μ_{Cu} and high μ_{In}, a Cu-poor phase can be observed, and for high μ_{Cu} and low μ_{In}, an In-poor phase can be observed. The latter is contradictory to experiment, where Cu-rich CIS is not observed and any excess of Cu above the $CuInSe_2$ stoichiometry segregates as Cu_2Se [87, 88]. The region with $c(\mathrm{Cu}) > 0.5$ results from the restriction to the chalcopyrite-like lattice in the simulations. This prohibits the formation of Cu_2Se or similar structures.

The region of high μ_{Cu} and high μ_{In} is dominated by a plateau of $Cu_{0.5}In_{0.5}Se$ [green area in Figures 4.15 a) and 4.16 a)]. This is exactly the $CuInSe_2$ stoichiometry of the defect-free chalcopyrite. The region extends to much higher values of μ_{Cu} and μ_{In} than shown in the plot, indicating that $CuInSe_2$ is the stable phase for a wide range of experimental conditions. This resilience of $CuInSe_2$ is also observed in experiment [87, 88].

By starting in the $CuInSe_2$ region and reducing μ_{Cu} and μ_{In} simultaneously, a path is created that is displayed in Figure 4.15 a). It forms a ramp and is denoted as such in the following discussion.

Along the ramp, the Cu concentration decreases while the In concentration increases slightly (Figure 4.17). This observation shows that CIS can occur in a multitude of stoichiometries which is consistent with literature [10, 11].

The existence of the ramp proves the general tendency of the CIS material towards Cu-depletion. Cu readily leaves the system in small or large quantities, depending on the conditions. This behaviour leads to Cu-poor phases (with a slightly increased In concentration), which have been observed experimentally. All high-efficiency CIS and CIGS solar cells feature a Cu-poor bulk composition of the absorber layer [47, 89].

Cu-depletion is especially important at any kind of surface [41, 42], in particular at the interface to the buffer layer and at grain boundaries [38].

The simulations are bulk calculations and as such not suited to describe scenarios with any kind of interface. An adequate description in the formalism of a CE would require many more structures to be calculated because interactions at the interface have to be taken into account. Additionally, the structures need to be much bigger to prevent the interaction of the interface

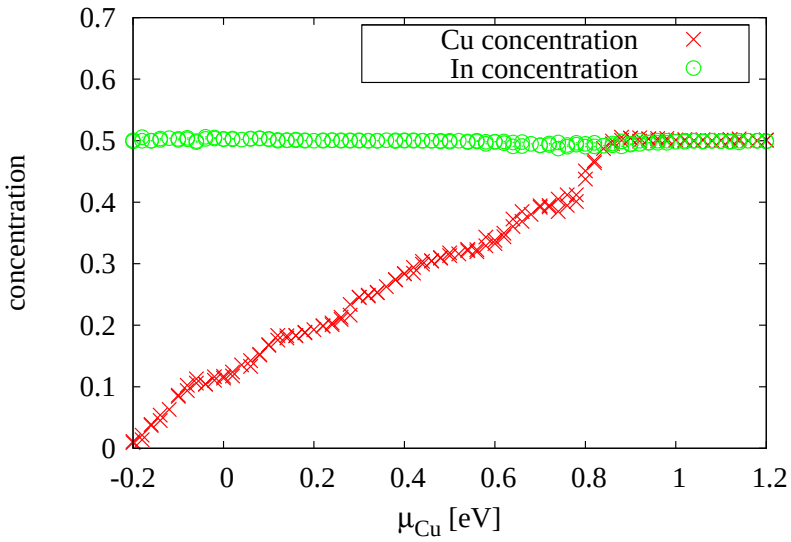

Figure 4.17: A cut of the ramp in the concentration landscape along the line through $\mu_{\mathrm{Cu}} = 0.2$ eV / $\mu_{\mathrm{In}} = 1.1$ eV and $\mu_{\mathrm{Cu}} = 1.0$ eV / $\mu_{\mathrm{In}} = 2.4$ eV. Small step-like structures are visible in the Cu concentration. Chemical potential values from simulations correspond to the values measured in experiment up to a constant. Positive values do not imply instability.

with itself due to the periodic boundary conditions. The exploration of these possibilities is up to future investigations.

The next prominent feature in the concentration landscape is a region with $CuIn_5Se_8$ stoichiometry around $\mu_{\mathrm{Cu}} = 0.5$ eV and $\mu_{\mathrm{In}} = 2.0$ eV [cyan area in Figures 4.15 a) and 4.16 a)]. The Cu concentration on this plateau is equal to 0.125. The corresponding In concentration, in the upper part of the orange region in Figures 4.15 b) and 4.16 b), is equal to 0.625. The red star in Figures 4.16 a) and b) marks the chemical potential values that have been determined for $CuIn_5Se_8$ with the particle insertion method. This resides on the extreme right side of the $CuIn_5Se_8$ plateau. Consequently, when one starts with the equilibrium chemical potential values for $CuIn_5Se_8$ and increases μ_{In} while simultaneously decreasing μ_{Cu}, the system will keep the $CuIn_5Se_8$ stoichiometry. On the other hand, if μ_{In} is decreased and μ_{Cu} is increased simultaneously, the concentration of In will drop sharply from 0.625 to 0.5 and the concentration of Cu will quickly increase from 0.125 to about 0.3.

The simulations with a $CuIn_5Se_8$ starting configuration did not reveal a distinct plateau for the $CuIn_3Se_5$ stoichiometry.

Figures 4.15 and 4.16 show data at a temperature of 174 K. The low temperature was chosen to reveal sharp structures in the landscape plots and to suppress temperature effects. Experimental devices will typically be exposed to much higher temperatures.

Figures 4.18 a) and b) show the Cu and In concentration for $T = 696$ K which is close to the typical production temperature for solar cell in a physical vapour deposition process. The plots looks similar to Figures 4.15 a) and b), but the $CuIn_5Se_8$ plateau has vanished. Instead, Figure 4.18 a) shows a continuous increase in the Cu concentration from the yellow region towards the ramp. Figure 4.18 b) exhibits a comparable behaviour of the In concentration in the corresponding (orange) region.

The $CuIn_5Se_8$ plateau is the only feature in the landscapes that vanishes at high temperatures. The $CuInSe_2$ plateau and the ramp in the Cu concentration hardly change at all. The implications of this observation are twofold: firstly, during the production process at high temperatures, the formation of a $CuIn_5Se_8$ defect phase is very unlikely. Secondly, after significantly cooling down the absorber, a $CuIn_5Se_8$ defect phase could form due to the large stability region at low temperatures. The formation of a $CuIn_5Se_8$ defect phase will then again influence the efficiency of the CIS solar cell.

$CuIn_3Se_5$ Starting Configuration

Figures 4.19 and 4.20 show the concentration landscapes and contour plots that were calculated with a $CuIn_3Se_5$ starting configuration at a temperature of 174 K.

The $CuIn_3Se_5$ starting configuration leads to a plateau with $CuIn_3Se_5$ stoichiometry around $\mu_{Cu} = 0.7$ eV and $\mu_{In} = 2.3$ eV [$c(\mathrm{Cu}) = 0.2$ and $c(\mathrm{In}) = 0.6$]. The plateau includes the chemical potential values that have been determined for $CuIn_3Se_5$ with the particle insertion method (red star in Figure 4.20).

The $CuIn_3Se_5$ plateau does not show up in the simulations with a $CuIn_5Se_8$ starting configuration. On the other hand, Figures 4.19 and 4.20 do not show a plateau for $CuIn_5Se_8$. The chemical potential regions of the two plateaus from the different simulations overlap, which is due to hysteresis. The other features in the landscape plots ($CuInSe_2$ plateau, ramp) visible in Figures 4.15 and 4.16 are also found in Figures 4.19 and 4.20.

To summarise, with the limited amount of MC sweeps, the defect phase plateaus of $CuIn_5Se_8$ and $CuIn_3Se_5$ are only found when using the corresponding starting configuration. The size of the resulting plateaus is overestimated: this can be concluded due to the overlap of the $CuIn_3Se_5$ and $CuIn_5Se_8$ regions from the different simulations. In the μ_{Cu}–μ_{In} plane, the coexistence

a) starting configuration $CuIn_5Se_8$, 696 K

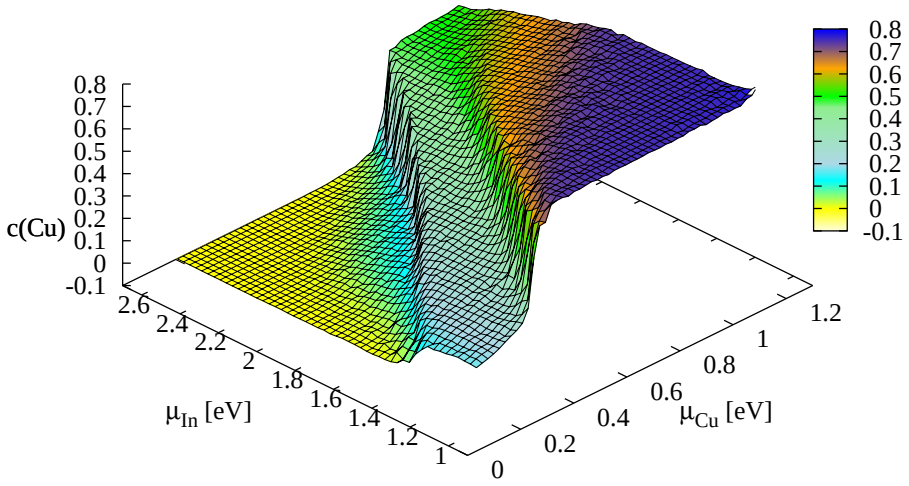

b)

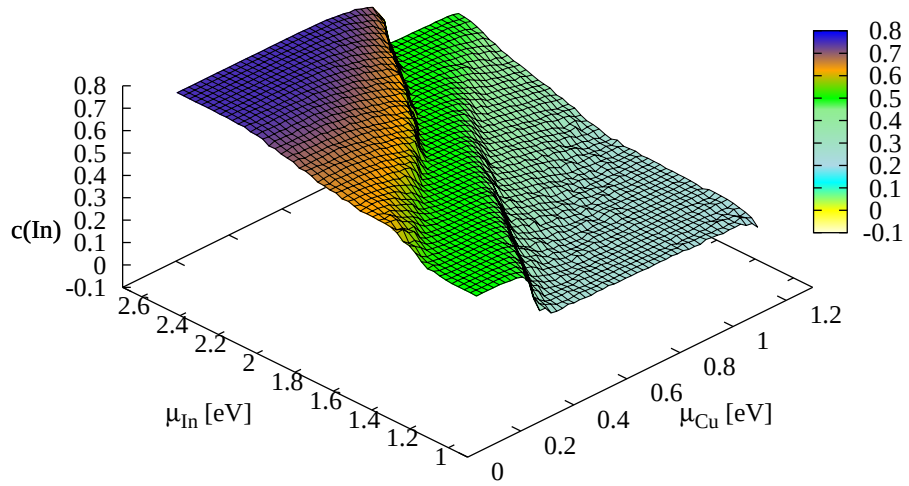

Figure 4.18: Landscape of the a) Cu concentration and b) In concentration versus the chemical potentials at $T = 696$ K with a $CuIn_5Se_8$ starting configuration. Chemical potential values from simulations correspond to the values measured in experiment up to a constant. Positive values do not imply instability.

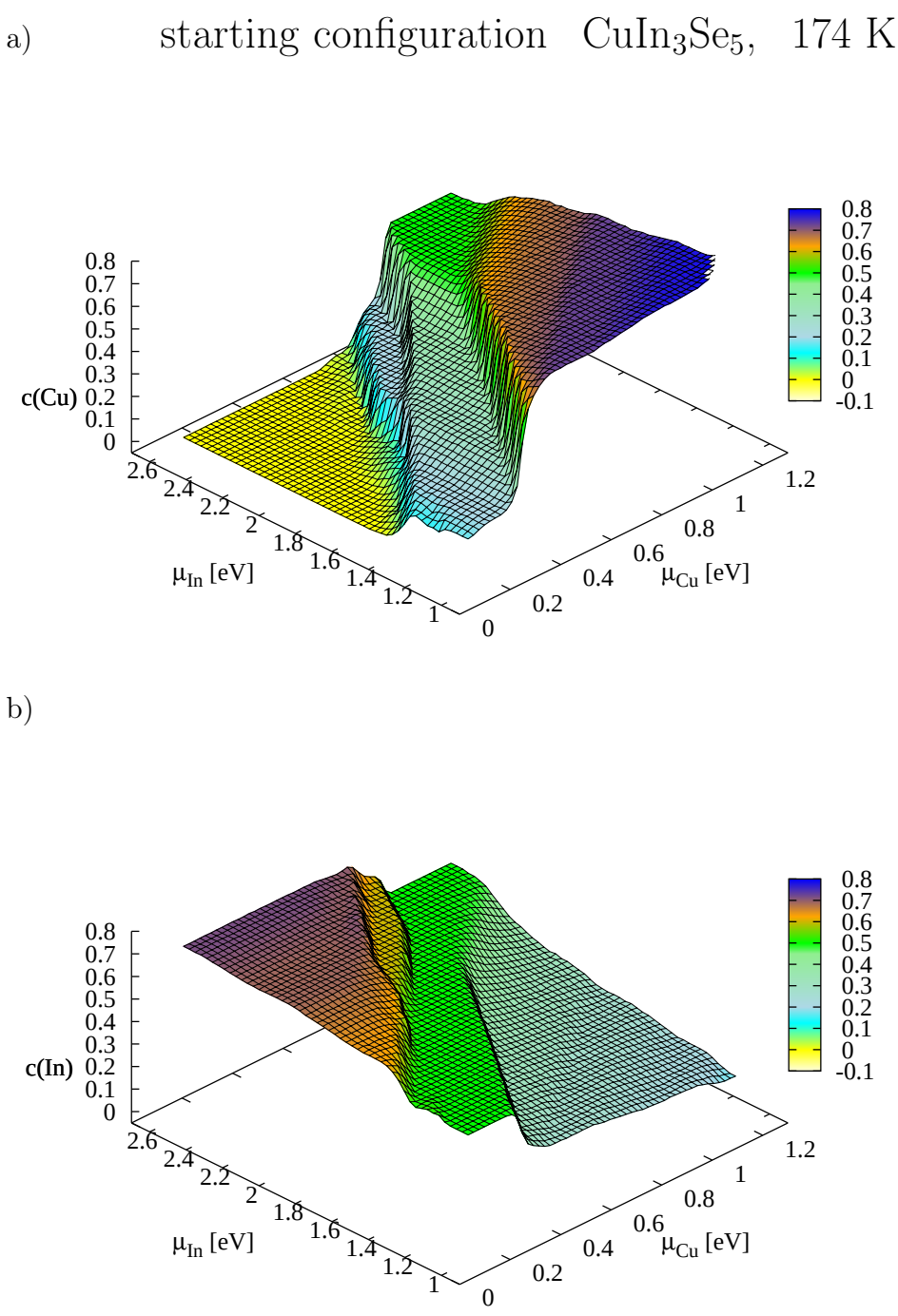

Figure 4.19: Landscape of the a) Cu concentration and b) In concentration versus the chemical potentials at $T = 174$ K with a $CuIn_3Se_5$ starting configuration. Chemical potential values from simulations correspond to the values measured in experiment up to a constant. Positive values do not imply instability.

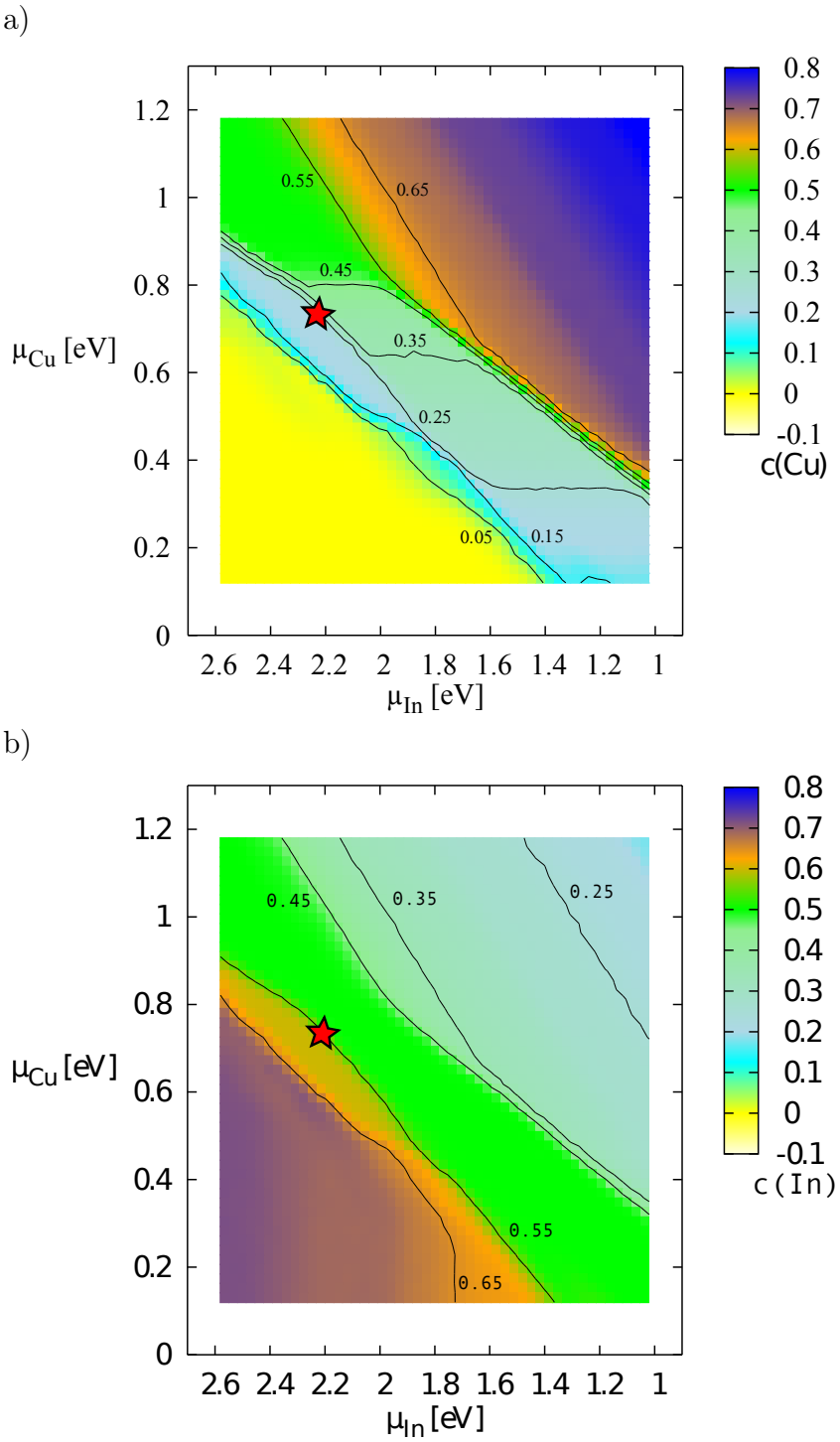

Figure 4.20: Contour plot of the a) Cu concentration and b) In concentration versus the chemical potentials at $T = 174$ K with a $CuIn_3Se_5$ starting configuration. The red star marks the equilibrium chemical potentials for $CuIn_3Se_5$ that have been determined with the particle insertion method. Chemical potential values from simulations correspond to the values measured in experiment up to a constant. Positive values do not imply instability.

region of two phases must be a line. The equilibrium transition between the $CuIn_3Se_5$ phase and the $CuIn_5Se_8$ phase lies within the overlap region. Further investigations of the transition were employed with a $CuInSe_2$ starting configuration and will be covered in the following section.

It is noteworthy that a stability region for $CuIn_3Se_5$ was found, even though the CE does not include structures with a $CuIn_3Se_5$ stoichiometry. This confirms the predictive power of the CE.

Simulations at a temperature of $T = 696$ K (Figure 4.21) reveal a picture that is similar to the simulations with a $CuIn_5Se_8$ starting configuration at the same temperature. In both cases, the plateau of the Cu-poor defect phase vanishes.

$CuInSe_2$ Starting Configuration

Figures 4.22 and 4.23 show the concentration landscapes and contour plots that were calculated with a $CuInSe_2$ starting configuration at a temperature of 174 K.

The landscapes show the $CuInSe_2$ plateau and the ramp: these features do not depend on the starting configuration. The $CuIn_5Se_8$ and $CuIn_3Se_5$ plateaus are not found due to the limited number of MC sweeps.

Calculating the landscapes with more MC sweeps (i.e. longer relaxation times) is not feasible. The simulations would take prohibitive amounts of time. Another approach needs to be used to check whether the $CuIn_5Se_8$ and $CuIn_3Se_5$ plateaus can be recovered from a $CuInSe_2$ starting configuration. The concentrations for 61 pairs of chemical potentials were calculated along a cut through both plateaus, starting with a $CuInSe_2$ configuration and relaxing for 10^6 MC sweeps with a temperature of 174 K. The line of the cut goes through $\mu_{Cu} = 0.3$ eV / $\mu_{In} = 1.7$ eV and $\mu_{Cu} = 0.9$ eV / $\mu_{In} = 2.6$ eV and is shown in Figure 4.25.

Figure 4.24 shows the Cu and In concentrations along the cut. As expected, both concentrations are 0.5 above $\mu_{Cu} = 0.8$ eV where the cut goes through the $CuInSe_2$ plateau. Between $\mu_{Cu} = 0.4$ eV and $\mu_{Cu} = 0.6$ eV, the concentrations of Cu is 0.125 and that of In is 0.625. This indicates the recovery of the $CuIn_5Se_8$ plateau and confirms the stability of $CuIn_5Se_8$ within this region. In the intermediate region where the $CuIn_3Se_5$ plateau is expected, the results are not as clear. Above $\mu_{Cu} = 0.6$ eV, the Cu concentration is higher than below $\mu_{Cu} = 0.6$ eV, yet it does not reach the expected 0.2 and some outliers are visible. This can be explained with the difficulties in forming $CuIn_3Se_5$ ground state structures that have already been discussed in Section 4.2.2.

a) starting configuration $CuIn_3Se_5$, 696 K

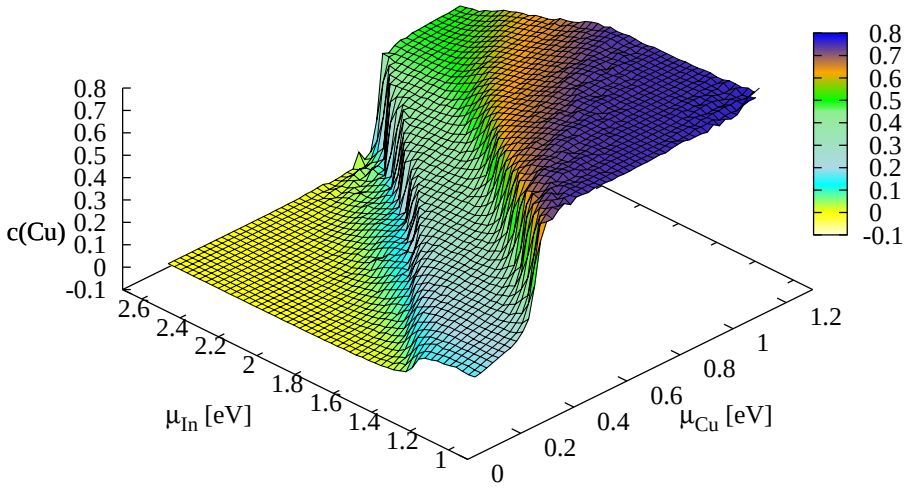

b)

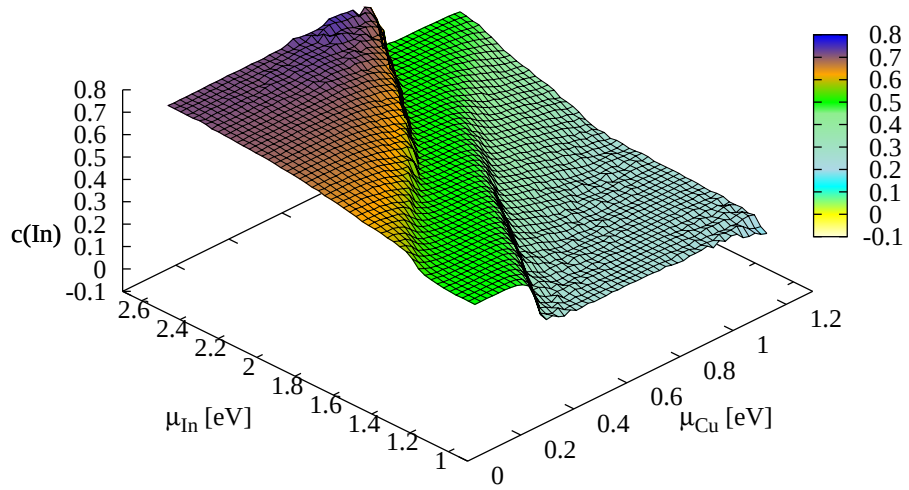

Figure 4.21: Landscape of the a) Cu concentration and b) In concentration versus the chemical potentials at $T = 696$ K with a $CuIn_3Se_5$ starting configuration. Chemical potential values from simulations correspond to the values measured in experiment up to a constant. Positive values do not imply instability.

a) starting configuration $CuInSe_2$, 174 K

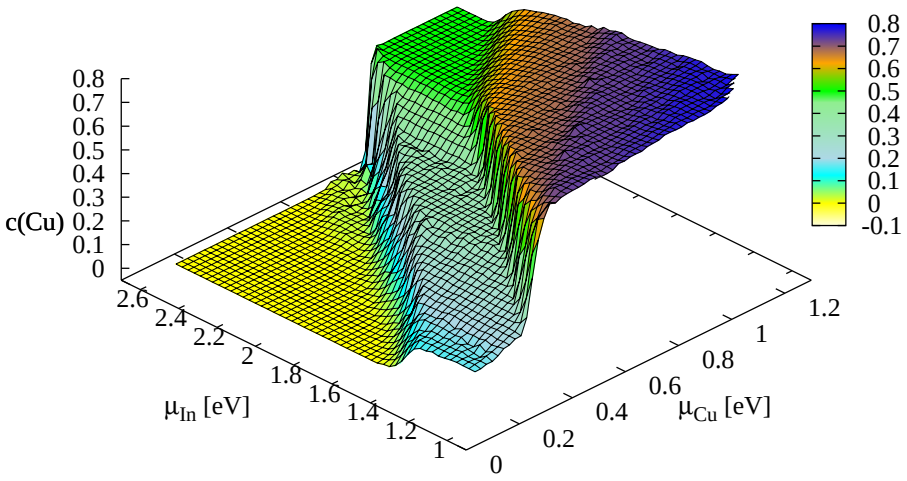

b)

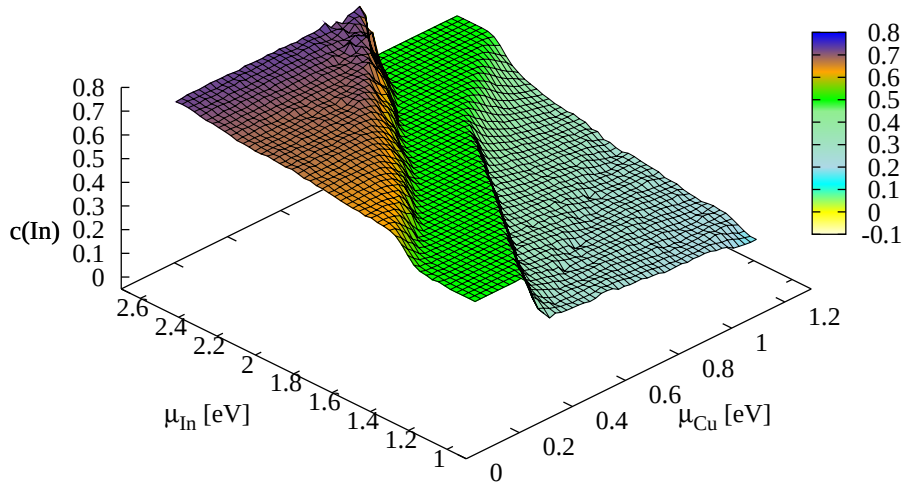

Figure 4.22: Landscape of the a) Cu concentration and b) In concentration versus the chemical potentials at $T = 174$ K with a $CuInSe_2$ starting configuration. Chemical potential values from simulations correspond to the values measured in experiment up to a constant. Positive values do not imply instability.

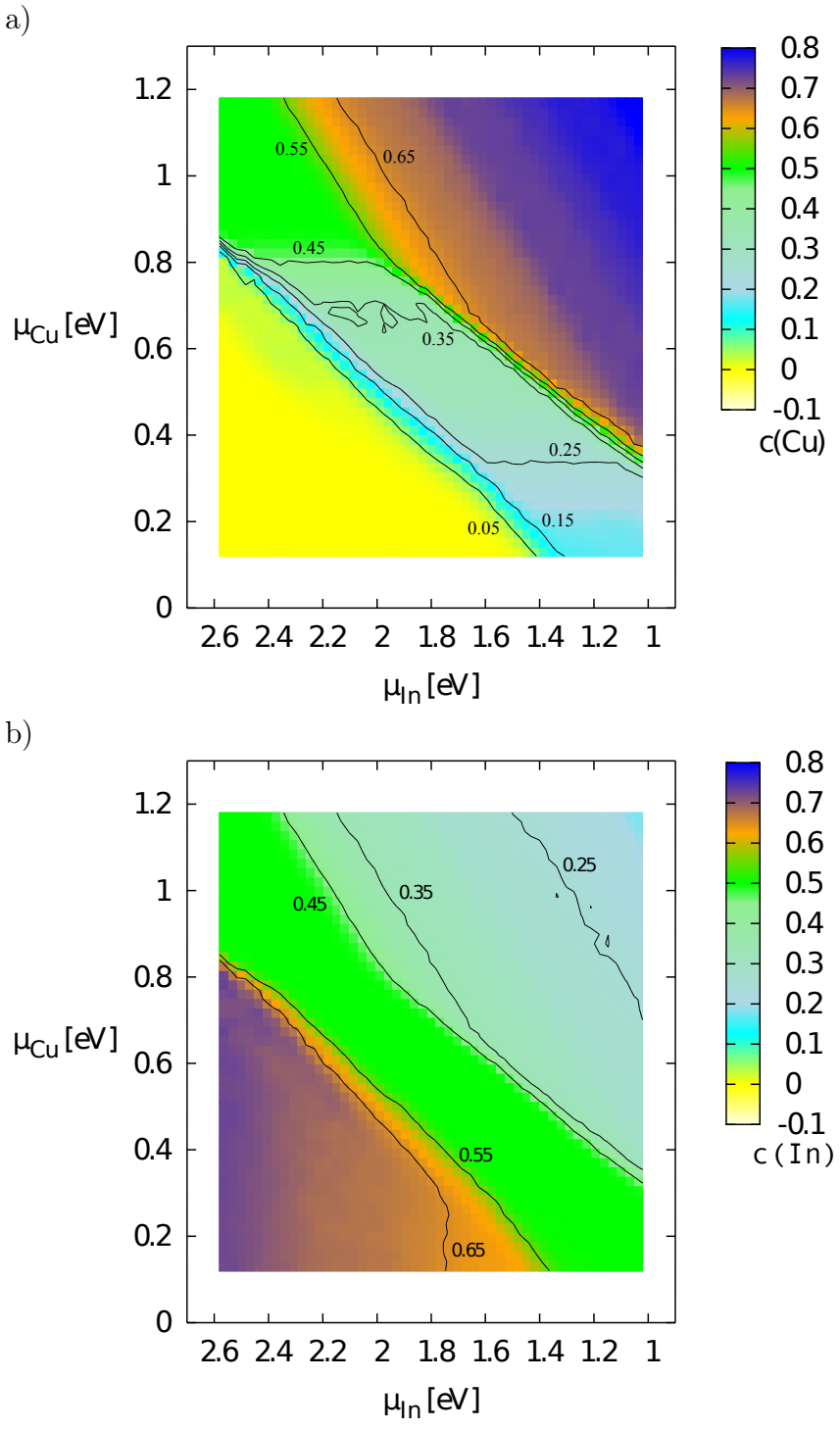

Figure 4.23: Contour plot of the a) Cu concentration and b) In concentration versus the chemical potentials at $T = 174$ K with a $CuInSe_2$ starting configuration. Chemical potential values from simulations correspond to the values measured in experiment up to a constant. Positive values do not imply instability.

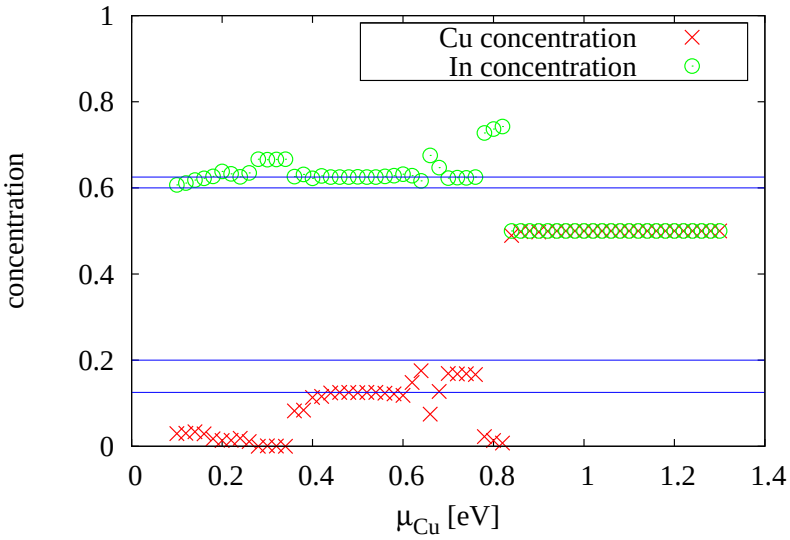

Figure 4.24: Cut through the concentration landscape along the line through $\mu_{\mathrm{Cu}} = 0.3$ eV / $\mu_{\mathrm{In}} = 1.7$ eV and $\mu_{\mathrm{Cu}} = 0.9$ eV / $\mu_{\mathrm{In}} = 2.6$ eV, calculated with $T = 174$ K and a starting configuration of $CuInSe_2$. The blue lines mark the values that correspond to specific Cu and In concentrations: 0.125, 0.625 (corresponding to $CuIn_5Se_8$) and 0.2, 0.6 (corresponding to $CuIn_3Se_5$). Chemical potential values from simulations correspond to the values measured in experiment up to a constant. Positive values do not imply instability.

Conclusion

The grand-canonical MC simulations have revealed stability regions for $CuInSe_2$, $CuIn_3Se_5$, and $CuIn_5Se_8$. These stoichiometries all lie on the Cu_2Se–In_2Se_3 tie-line and have the same total number of valence electrons.

The $CuInSe_2$ plateau is always present and large in the concentration landscape, no matter what starting configuration or simulation temperature is chosen. This implies that $CuInSe_2$ is very resilient and can form under a great variety of experimental conditions and at a wide range of temperatures. Due to this flexibility, the process parameter window for the production of CIS solar cells is quite large, thereby opening up the possibility of adjusting parameters in order to optimise the process.

The $CuIn_3Se_5$ and $CuIn_5Se_8$ plateaus are not as broad as the $CuInSe_2$ plateau and are susceptible to the starting configuration and the temperature of the simulation. At low temperatures, the plateau is only found with a starting configuration of the same stoichiometry. This reveals the difficulty of reaching thermal equilibrium in certain cases. At high temperatures, the

plateaus vanish and there is no distinct stability region for $CuIn_3Se_5$ and $CuIn_5Se_8$.

Based on our results, we constructed a schematic phase diagram. Figure 4.25 shows the approximate locations of the $CuInSe_2$ phase, the $CuIn_5Se_8$ phase, the intermediate phase, and the cut. The intermediate phase is probably $CuIn_3Se_5$, because it is positioned where a $CuIn_3Se_5$ plateau was found in the simulations with a $CuIn_3Se_5$ starting configuration.

Interestingly, the $CuIn_3Se_5$ separates the other two phases and it is not possible to reach $CuIn_5Se_8$ directly from $CuInSe_2$. It can be expected that local chemical potential values vary continuously in bulk CIS and that neighbouring phases in the material are also adjacent in the phase diagram. Since the bulk of the absorber exhibits $CuInSe_2$ stoichiometry (with a slight Cu deficiency), it is reasonable to assume that a Cu-poor region in the bulk will have $CuIn_3Se_5$ stoichiometry and not $CuIn_5Se_8$.

These insights can help to control a production process for solar cells. For instance, in a physical vapour deposition process, the chemical potentials can be influenced by adjusting the partial vapour pressures of Cu and In. This directly influences the position in the μ_{Cu}–μ_{In} concentration landscape and the formation of different phases.

High production temperatures can be used to avoid Cu-poor defect phases. However, the Cu-poor stoichiometries on the ramp are still possible. The ramp can be avoided through the regulation of the chemical potentials to provide defect-free CIS absorbers. Upon cooling down, given the right conditions, defect phases can form in the solar cells. This degradation will influence the cells' performance during their lifetime.

The ramp is a region with continuously decreasing Cu concentration and almost constant In concentration. This result allows stoichiometries with small Cu deficiency like those used in high-efficiency CIS and CIGS solar cells [47, 89]. It also shows that Cu readily leaves the system in small or large quantities, while the In concentration is hardly affected.

A further important conclusion is revealed by the relative positions of the defect phase plateaus. To get from the $CuIn_3Se_5$ to the $CuIn_5Se_8$ plateau, μ_{Cu} and μ_{In} both have to be decreased. A decrease in the chemical potential should in general lead to a decrease in the corresponding concentration which is the case for the Cu concentration. The In concentration on the other hand is higher at the $CuIn_5Se_8$ plateau than at the $CuIn_3Se_5$ plateau. The direct influence of μ_{In} on the In concentration is dominated by the influence of Cu. In other words, for a given Cu concentration on the $CuIn_5Se_8$ plateau, the In concentration will increase to a value that stabilises the defect structure despite the lower μ_{In}.

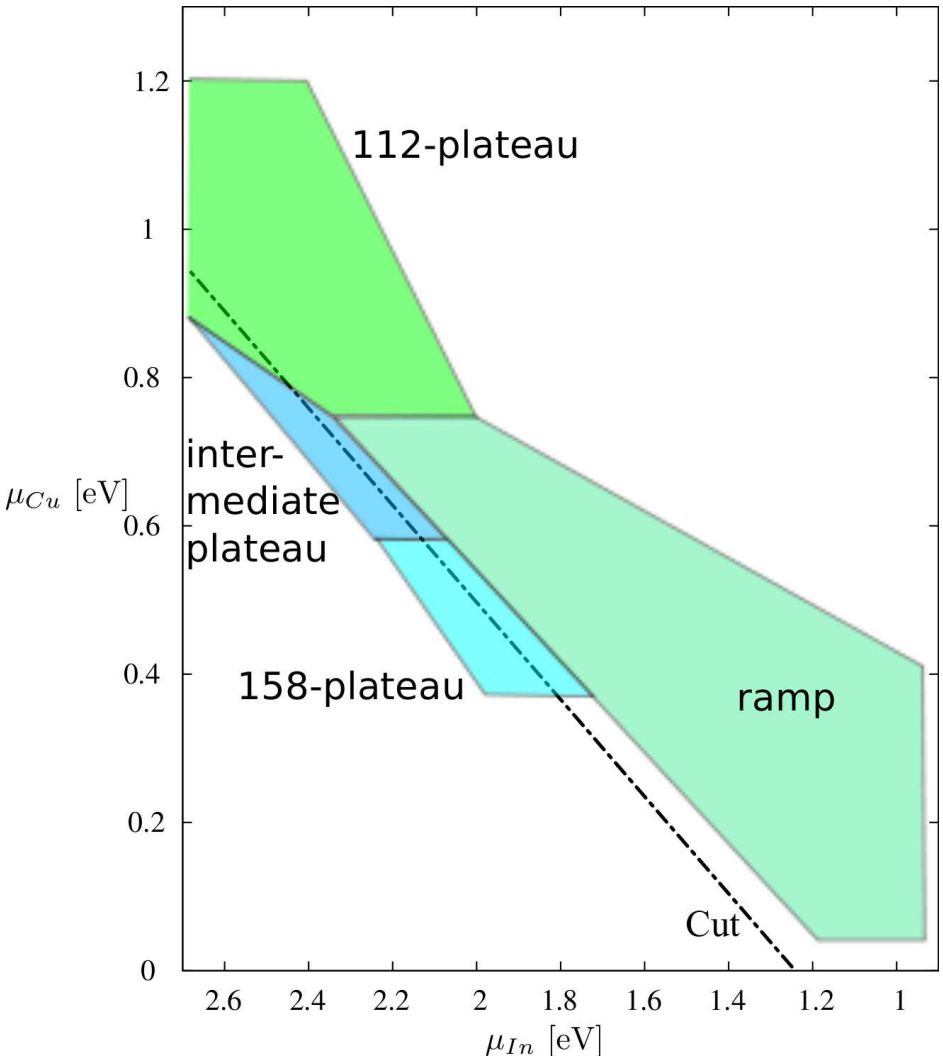

Figure 4.25: Schematic phase diagram with stability regions of $CuInSe_2$, $CuIn_5Se_8$, and an intermediate phase at $T = 174$ K. Chemical potential values from simulations correspond to the values measured in experiment up to a constant. Positive values do not imply instability.

This observation can easily be understood. The $CuIn_3Se_5$ stoichiometry is stable, which prevents additional In atoms from occupying vacancies, despite the relatively high chemical potential of In. Now, let μ_{Cu} decrease and μ_{In} stay constant. A removal of Cu from the $CuIn_3Se_5$ system breaks down the stable structure and leaves vacancies that are now readily occupied by In. In fact, the high μ_{In} leads to In forcing all other Cu atoms out of the system and the $CuIn_5Se_8$ concentration is not achieved. To prevent this, it is necessary to decrease μ_{In} and μ_{Cu} simultaneously.

4.3 In-free Absorbers

Indium and gallium are expensive elements. For this reason, potential In/Ga-free absorber materials have been investigated in the past [21, 90]. One common method of replacing the In in $CuInSe_2$ is to take out the 3-valent In and replace it with 50% of a 2-valent element (e.g. Zn) and 50% of a 4-valent element (e.g. Sn). Zn and Sn are commonly chosen because Sn is a direct neighbour of In and Zn is a direct neighbour of Ga in the periodic table. Additionally, S is used instead of Se, leading to $CuZn_{0.5}Sn_{0.5}S_2$.

Formation energies for different configurations of $CuZn_0.5Sn_0.5S_2$ have been calculated to see whether the creation of a cluster expansion and the investigation of Zn-Sn disorder analogue to Section 4.1 could be promising. Figure 4.26 shows two structures that have been calculated: they differ only by the position of one Zn and Sn atom which are swapped in Figure 4.26 b) with respect to Figure 4.26 a).

The structure in Figure 4.26 a) has the lower configurational energy. The energy difference between the two is 146 meV and, as such, 15 times higher than the typical energy difference in $Cu(In,Ga)Se_2$ of 10 meV. As a result, much higher temperatures are necessary to perturb the ordered groundstate of $CuZn_0.5Sn_0.5S_2$. In the temperature range that is relevant for solar cells, $CuZn_0.5Sn_0.5S_2$ will show no significant Zn-Sn disorder. For this reason, no further investigations were undertaken.

a)

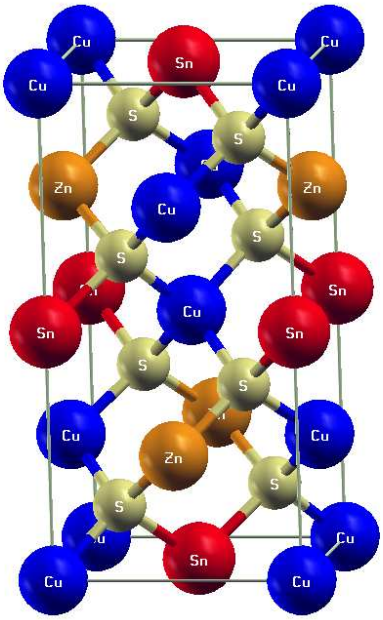

b)

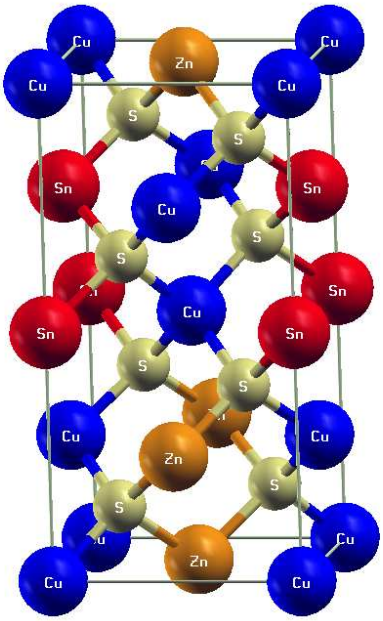

Figure 4.26: Two possible structures for $CuZn_{0.5}Sn_{0.5}S_2$.

Chapter 5

Summary and Outlook

Computer simulations are a suitable tool to improve the understanding of the solar cell absorber material CIGS. For a comprehensive description, it is necessary to combine several methods, because no single method alone can accurately describe the complex CIGS system. In this thesis, computer simulation results have been presented and compared with experimental data. Additionally, the implications for industrial CIGS solar cell production processes have been discussed.

The employed method is a combination of Monte Carlo (MC) simulations and density functional theory (DFT). The latter is used to generate a cluster expansion (CE) of the configurational energy which is in turn used to calculate the energies in the MC simulations. Two CEs were constructed for this thesis.

The first one yields configurational energies for $CuIn_xGa_{1-x}Se_2$ in which Cu and Se are kept fixed and In and Ga are distributed arbitrarily on the remaining lattice sites. The In concentration x can assume values between 0 and 1.

The second CE describes the configurational energy of Cu-poor (Cu,In,Vac)Se structures. For this creation, only structures that are part of the Cu_2Se–In_2Se_3 tie-line were used. The structures can be generated from $CuInSe_2$ by adding $(2Vac_{Cu} + In_{Cu})$ defect complexes.

The MC simulations of $CuIn_xGa_{1-x}Se_2$ reveal that In and Ga do not form a well-ordered structure in the material. Below a demixing transition close to room temperature, the material separates into a $CuInSe_2$ phase and a $CuGaSe_2$ phase. Above the transition temperature, In and Ga are distributed randomly and the homogeneity of the distribution increases with increasing temperature.

The distribution of In and Ga has a direct influence on the band gap of the material. Band gap fluctuations are detrimental for solar cell performance.

The homogeneity of In-rich CIGS is higher than the homogeneity of Ga-rich CIGS at all considered temperatures between room temperature and the production temperature of CIGS solar cells. This observation contributes to the relatively low efficiency of CIGS solar cells with a high Ga content.

The simulation results are compared with photoluminescence experiments by Gütay and Bauer [82]. The experimentally observed band gaps in CIGS samples follow a Gaussian distribution with a FWHM of 8 meV. The histograms of the simulation data are translated into band gap distributions and the results are extrapolated to the scan-pixel size of the experiments in Reference [82]. According to the calculations, the contribution of In-Ga disorder to the total band gap fluctuations is 2.20 meV at a temperature of 406 K and 1.01 meV at 870 K.

The results show that CIGS phase separates at low temperatures. However, no phase separation is observed experimentally. It can be concluded that the In-Ga distribution is "frozen" in a high-temperature state. Consequently, the absorber material of CIGS solar cells is not in thermal equilibrium, but in a glassy state.

The simulations with the (Cu,In,Vac)Se CE yielded equally interesting results. The focus of the investigations was on the experimentally observed stoichiometries $CuInSe_2$, $CuIn_3Se_5$, and $CuIn_5Se_8$.

$CuIn_5Se_8$ is the simplest Cu-poor structure, because the stoichiometry can be realised with a single 16-atom unit cell. The CE included 8 $CuIn_5Se_8$ structures with particularly low energy. Only 6 of these have been reported before in [18].

At low temperatures, $CuIn_5Se_8$ forms an ordered state. Above the order-disorder transition temperature of $T_0 = 279$ K, the cations become disordered. The exact value of the order-disorder transition temperature was determined by multi-histogram simulations.

Even though the system starts to become disordered above T_0, it retains a certain degree of order up to high temperatures. This can be seen in the frequencies of $k = 7$ and $k = 9$ tetrahedra around Se atoms. These decrease continuously ($k = 7$) or even stay constant ($k = 9$). k is equal to the number of valence electrons of the four nearest neighbour atoms of Se.

The canonical simulations of $CuIn_3Se_5$ find an ordered ground state at low temperatures. Additionally, they reveal a meta-stable state that exists at the same temperatures and exhibits the same frequency of $k = 7$, $k = 8$, and $k = 9$ tetrahedra around Se atoms. The meta-stable state does not relax to the stable state within as many as 3.5 million MC sweeps and the two states can evolve from the same starting configuration only by applying a different random seed. This hints at a complex free energy landscape with high barriers.

Grand-canonical MC simulations reveal regions of chemical potential values μ_{Cu} and μ_{In} that correspond to $CuInSe_2$, $CuIn_3Se_5$, and $CuIn_5Se_8$ stoichiometries. All three phases can be clearly identified and have distinct stability regions. At a high temperature (696 K), the stability regions of $CuIn_3Se_5$ and $CuIn_5Se_8$ disappear, whereas $CuInSe_2$ is still stable.

The landscape plots of the Cu concentration show a ramp: a continuous decrease of Cu content. In the same region, the In concentration is almost constant. The decrease in Cu content is not linear, but shows small step-like structures. These hint at possible stable stoichiometries that are not part of the Cu_2Se–In_2Se_3 tie-line. The ramp also illustrates that Cu readily leaves the system in small or big amounts given the right conditions. Cu vacancies can be either occupied by additional In or, close to the CdS–CIGS interface of solar cells, by Cd that diffuses into the CIGS absorber. A first indication for Cd occupying Cu vacancies is given in [91].

The results of this thesis are not only of academic interest, but also have important implications for industrial solar cell production processes. First of all, the $CuIn_xGa_{1-x}Se_2$ simulations show that the In–Ga distribution is frozen in a state that corresponds to a high temperature. Furthermore, the homogeneity of the material increases with higher temperatures. It is therefore obvious that a higher production temperature in conjunction with a reasonably fast cooling will lead to a more homogeneous absorber material and in consequence to an improved efficiency. This conclusion has recently been proved experimentally [92]. It should however be noted that the increased temperature not only affects the In–Ga distribution, and that increased homogeneity is not the only contribution to the increased cell efficiency.

A source of degradation for CIGS solar cells could be the relaxation of the frozen high-temperature state of the absorber towards thermal equilibrium. This would lead to clustering and even phase separation, resulting in a decrease of the cell efficiency. It is up to further investigations to study ways of preventing this degradation.

The (Cu,In,Vac)Se simulations revealed an order-disorder transition in $CuIn_5Se_8$ at $T_0 = 279$ K. Typically, solar cells do not operate at such low temperatures. Consequently, $CuIn_5Se_8$ defect phases that could occur in solar cells will not assume an ordered state (e.g. one of the 8 low-energy structures that have been found), but will be disordered. It is thus not sufficient to consider small unit cells of ordered structures for the theoretical description of the electronic properties of defect phases in operational solar cells.

Increasing the temperature to the production temperature of solar cells leads to the disappearance of the $CuIn_5Se_8$ and $CuIn_3Se_5$ defect phases. Con-

sequently, during the production process, the defect phases are unlikely to occur. However, experimental evidence points at grain boundaries and the buffer–absorber interface being Cu-poor. These are the locations where defect phases will preferably form after the absorber material has cooled down.

Cu-poor defect phases can form in the bulk absorber during the lifetime of a solar cell if the conditions are such that Cu leaves the absorber material. In this case, the formation of $CuIn_5Se_8$ or $CuIn_3Se_5$ in the bulk CIGS will contribute to degradation of the cell.

The production process for CIGS solar cells can be controlled by adjusting the chemical potentials μ_{Cu} and μ_{In}. In a physical vapour deposition process, this can be realised by adjusting the partial vapour pressures of Cu and In. This way, the position of the process in the μ_{Cu}–μ_{In} concentration landscape can be controlled. The $CuInSe_2$ stability region in the concentration landscape is large at all considered temperatures. This implies that it can form under a great variety of experimental conditions and at a wide range of temperatures. Due to this exceptional resilience, there is an extensive window of process parameters within which the production conditions for $CuInSe_2$ can be optimised.

The best CIGS solar cells have a slightly Cu-poor absorber layer. It is thus desirable to choose chemical potentials that guarantee $CuInSe_2$ stoichiometry with a slight Cu-deficiency. According to the simulation results, this can best be achieved at the upper end of the ramp ($\mu_{Cu} \approx 0.8$ eV and $\mu_{In} \approx 2.1$ eV). At that point, the stoichiometry is relatively insensitive to μ_{In}. It does not change significantly between $\mu_{In} = 2.0$ eV and $\mu_{In} = 2.3$ eV. On the other hand, it is crucial to accurately choose the right value for μ_{Cu}. The stoichiometry is very sensitive to changes, especially towards lower values of μ_{Cu}. This would affect the cell efficiency.

In a typical vapour deposition process, the vapour pressures are not constant. The timing of adjusting the vapour pressures of the various elements is very delicate. There is a stage where only In/Ga and Se are evaporated. After that comes a stage where In/Ga is replaced by Cu evaporation. This stage has to be stopped at the $CuInSe_2$ stoichiometric point. The measurement of this point is indirect and subject to inaccuracy. This timing issue can be avoided by choosing constant vapour pressures for all elements according to the simulation results.

There are still numerous unanswered questions that need to be investigated in future studies.

To compare experimental production conditions with the results of the grand-canonical simulations, it is necessary to translate the vapour pressures into chemical potentials. Since the vapour pressures are usually not

constant, the production process follows a path in the concentration landscape. A determination of this path will help to better improve the understanding of typical production processes (e.g. physical vapour deposition and co-evaporation). This comparison could explain why solar cells from physical vapour deposition typically yield higher efficiencies than cells from co-evaporation.

A desirable follow-up to the presented simulations would be an extension of the CE to interfaces. This would increase the computational effort, because more ab initio energies would have to be calculated and larger unit cells used. However, this would shed light on the Cu-deficiency at locations where it is most prominently observed: grain boundaries and the CdS–CIGS interface [38, 41, 42].

Another possible extension would be the inclusion of more atomic species. For instance, Se could be included. Se defects play an important role and recent experiments have shown that the vapour pressure of Se has a significant effect on the efficiency of the solar cell [93].

Additional interesting extensions would be the inclusions of Na and Cd, but their concentrations are typically low. Huge unit cells are necessary to realise the experimentally observed concentrations in the order of 1%. Within this context, one hypothesis that can be tested is, whether Cd diffuses into the CIGS absorber at the CdS–CIGS interface and forces Cu out.

The presented results show a ramp in the Cu concentration landscape, which is very resilient to changes in the starting configuration and temperature. To gain better understanding of this particular region, the corresponding stoichiometries will have to be studied with ab initio methods. This requires large unit cells. It is possible that the CIGS lattice structure with its $I\bar{4}2d$ symmetry is not the ground state structure for these stoichiometries. This possibility could be investigated with molecular dynamics simulations.

The simulations of $Cu(In,Ga)Se_2$ show that after the production process, the absorber is frozen in a state corresponding to a high temperature. This hypothesis could not be studied further within the scope of this thesis. Testing is up to future investigations.

A related issue turns up in the (Cu,In,Vac)Se simulations. At high temperatures, no regions of $CuIn_5Se_8$ and $CuIn_3Se_5$ defect phases can be observed. However, cooling down can lead to the formation of defect phases if the system reaches thermal equilibrium. Alternatively, the system could also be frozen in a state corresponding to a high temperature, which would inhibit the formation of defect phases. The question which possibility reflects reality will have to be answered by future studies.

List of Figures

List of Tables

Bibliography

[1] Nate Lewis. *A Global Energy Perspective, Caltech, The Lewis Group*, (2004).

[2] David B. Mitzi, Min Yuan, Wei Liu, Andrew J. Kellock, S. Jay Chey, Vaughn Deline, and Alex G. Schrott. A High-Efficiency Solution-Deposited Thin-Film Photovoltaic Device. *Advanced Materials*, **20**, 3657, (2008).

[3] Min Yuan, David B. Mitzi, Wei Liu, Andrew J. Kellock, S. Jay Chey, and Vaughn Deline. Optimization of CIGS-Based PV Device through Antimony Doping. *Chem. Mater.*, **22**, 285, (2010).

[4] *Zentrum für Sonnenenergie- und Wasserstoff-Forschung Baden-Württemberg, Press Release*, (2010).

[5] J.E. Jaffe and Alex Zunger. Electronic structure of the ternary chalcopyrite semiconductors CuAlS2, CuGaS2, CuInS2, CuAlSe2, CuGaSe2 and CuInSe2. *Phys. Rev. B*, **28**(10), 5822, (1983).

[6] Su-Huai Wei, L. G. Ferreira, and Alex Zunger. First-principles calculation of the order-disorder transition in chalcopyrite semiconductors. *Phys. Rev. B*, **45**(5), 2533, (1992).

[7] Su-Huai Wei, S.B. Zhang, and Alex Zunger. Band offsets at the CdS/CuInSe2 heterojunction. *Appl. Phys. Lett.*, **63**(18), 2549, (1993).

[8] Su-Huai Wei and Alex Zunger. Band offsets and optical bowings of chalcopyrites and Zn-based II-VI alloys. *J. Appl. Phys.*, **78**, 3846, (1995).

[9] M. Gloeckler and J.R. Sites. Band-gap grading in Cu(In,Ga)Se2 solar cells. *J. of Phys. and Chem. of Solids*, **66**, 1891, (2005).

[10] S. B. Zhang, Su-Huai Wei, and Alex Zunger. Stabilization of ternary Compounds via Ordered Arrays of Defect Pairs. *Phys. Rev. Lett.*, **78**, 4059, (1997).

[11] S.B. Zhang, Su-Huai Wei, Alex Zunger, and H. Katayama-Yoshida. Defect physics of the CuInSe2 chalcopyrite semiconductor. *Phys. Rev. B*, **57**(16), 9642, (1998).

[12] Su-Huai Wei, S. B. Zhang, and Alex Zunger. Effects of Na on the electrical and structural properties of CuInSe2. *J. Appl. Phys.*, **85**(10), 7214, (1999).

[13] Su-Huai Wei, S.B. Zhang, and Alex Zunger. Effects of Ga addition to CuInSe2 on its electronic, structural and defect properties. *Appl. Phys. Lett.*, **72**(24), 3199, (1998).

[14] Chia-Hua Huang. Effects of Ga content on Cu(In,Ga)Se2 solar cells studied by numerical modeling. *J. of Phys. and Chem. of Solids*, **69**, 330, (2008).

[15] John E. Jaffe and Alex Zunger. Defect-induced nonpolar-to-polar transition at the surface of chalcopyrite semiconductors. *Phys. Rev. B*, **64**, 241304, (2001).

[16] Stephan Lany and Alex Zunger. Anion vacancies as a source of persistent photoconductivity in II-VI and chalcopyrite semiconductors. *Phys. Rev. B*, **72**, 035215, (2005).

[17] Clas Persson, Yu-Jun Zhao, Stephan Lany, and Alex Zunger. n-type doping of CuInSe2 and CuGaSe2. *Phys. Rev. B*, **72**, 035211, (2005).

[18] C.-H. Chang, Su-Huai Wei, J. W. Johnson, S. B. Zhang, N. Leyarovska, Grant Bunker, and T. J. Anderson. Local structure of $CuIn_3Se_5$: X-ray absorption fine structure study and first-principles calculations. *Phys. Rev. B*, **68**, 054108, (2003).

[19] Z. A. Shukri, L. S. Yip, C. X. Qiu, I. Shih, and C. H. Champness. Preliminary photovoltaic cells with single crystal CIS substrates. *Solar Energy Materials and Solar Cells*, **37**, 395, (1995).

[20] Markus Gloeckler, James R. Sites, and Wyatt K. Metzger. Grain-boundary recombination in Cu(In,Ga)Se2 solar cells. *J. Appl. Phys*, **98**, 113704, (2005).

[21] J.M. Raulot, C. Domain, and J.F. Guillemoles. Ab initio investigation of potential indium and gallium free chalcopyrite compounds for photovoltaic application. *J. of Phys. and Chem. of Solids*, **66**, 2019, (2005).

[22] A. Bouloufa, K. Djessas, and A. Zegadi. Numerical simulation of CuIn(x)Ga(1-x)Se2 solar cells by AMPS-1D. *Thin Solid Films*, **515**, 6285, (2007).

[23] J.H. Werner, Julian Mattheis, and Uwe Rau. Efficiency limitations of polycrystalline thin film solar cells: case of Cu(In,Ga)Se2. *Thin Solid Films*, **480**, 399, (2005).

[24] Thomas Gruhn. Comparatice ab initio study of half-Heusler compounds for optoelectronic applications. *Phys. Rev. B*, **82**, 125210, (2010).

[25] W. Andreoni, A. Baldereschi, and R. Car. Effects of Cation Order on the Energy Bands of GaAs-AlAs Heterostructures. *Solid State Commun.*, **27**, 821, (1978).

[26] P.E. Blöchl, E. Smargiassi, R. Car, D.B. Laks, W. Andreoni, and S.T. Pantelides. First-principles Calculations of Self-Diffusion Constants in Silicon. *Phys. Rev. Lett.*, **70**, 2435, (1993).

[27] E.I. Haskal, A. Curioni, P.F. Seidler, and W. Andreoni. Lithium-aluminium contacts for organic light-emitting devices. *Appl. Phys. Lett.*, **71**, 1151, (1997).

[28] Razvan A. Nistor, Dennis M. Newns, and Glenn J. Martyna. The Role of Chemistry in Graphene Doping for Carbon-Based Electronics. *ACS Nano, accepted for publication*, **5**, 3096, (2011).

[29] Amal Kasry, Marcelo A. Kuroda, Glenn J. Martyna, George S. Tulevski, and Ageeth A. Bol. Chemical doping of large-area stacked graphene films for use as transparent conducting electrodes. *ACS Nano*, **4**, 3839, (2010).

[30] Philippe Chatelain, Alessandro Curioni, Michael bergdorf, Diego Rossinelli, Wanda Andreoni, and Petros Koumoutsakos. Billion vortex particle direct numerical simulation of aircraft wakes. *Comput. Methods Appl. Mech. Engrg.*, **197**, 1296, (2008).

[31] Wanda Andreoni. Computational approach to the physical chemistry of fullerenes and their derivatives. *Annual Rev. Phys. Chem.*, **49**, 405, (1998).

[32] P. Hohenberg and W. Kohn. Inhomogeneous Electron Gas. *Phys. Rev.*, **136**, 864, (1964).

[33] W. Kohn and L.J. Sham. Self-Consistent Equations Including Exchange and Correlation Effects. *Phys. Rev.*, **140**, 1133, (1965).

[34] Nicholas Metropolis, Arianna W. Rosenbluth, Marshall N. Rosenbluth, Augusta H. Teller, and Edward Teller. Equation of State Calculations by Fast Computing Machines. *J. Chem. Phys.*, **21**, 1087, (1953).

[35] J.M. Sanchez, F. Ducastelle, and D. Gratias. Generalized cluster description of multicomponent systems. *Physica A*, **128**, 334, (1984).

[36] S. Müller. Bulk and surface ordering phenomena in binary metal alloys. *J. Phys. Condens. Matter*, **15**, R1429, (2003).

[37] David B. Laks, L.G. Ferreira, Sverre Froyen, and Alex Zunger. Efficient cluster expansion for substitutional systems. *Phys. Rev. B*, **46**, 12587, (1992).

[38] M.J. Hetzer, Y.M. Strzhemechny, M. Gao, M.A. Contreras, A. Zunger, and L.J. Brillson. Direct observation of copper depletion and potential changes at copper indium gallium diselenide grain boundaries. *Appl. Phys. Lett.*, **86**, 162105, (2005).

[39] Takashi Minemoto, Takuya Matsui, Hideyuki Takakura, Yoshihiro Hamakawa, Takayuki Negami, Yasushiro Hashimoto, Takeshi Uenoyama, and Masatoshi Kitagawa. Theoretical analysis of the effect of conduction band offset of window/CIS layers on performance of CIS solar cells using device simulation. *Solar Energy Materials and Solar Cells*, **67**, 83, (2001).

[40] M. Turowski, M.K. Kelly, and G. Margaritondo. Direct confirmation of the conduction-band lineup in the CuInSe2-CdS heterojunction solar cell. *Appl. Phys. Lett.*, **44**(8), 768, (1984).

[41] H.Mönig, Ch.-H. Fischer, A. Grimm, B. Johnson, C.A. Kaufmann, R. Caballero, I. Lauermann, and M.Ch. Lux-Steiner. Surface Cu-depletion of Cu(In,Ga)Se_2 thin films: Further experimental evidence for a defect-induced surface reconstruction. *J. Appl. Phys.*, **107**, 113540, (2010).

[42] Dongxiang Liao and Angus Rockett. Cu depletion at the $CuInSe_2$ surface. *Appl. Phys. Lett.*, **82**, 2829, (2003).

[43] H.W. Spiess, U. Haeberlen, G. Brandt, A. Räuber, and J. Schneider. Nuclear Magnetic Resonance in I_B-III-VI_2 Semiconductors. *Phys. Status Solidi B*, **62**, 183, (1974).

[44] D. Schmid, M. Ruckh, F. Grunwald, and H.W. Schock. Chalcopyrite/defect chalcopyrite heterojunctions on the basis of $CuInSe_2$. *J. Appl. Phys.*, **73**, 2902, (1993).

[45] M. Souilah, A. Lafond, C. Guillot-Deudon, S. Harel, and M. Evain. Structural investigation of the Cu_2Se-In_2Se_3-Ga_2Se_3 phase diagram, X-ray photoemission and optical properties of the $Cu_{1-z}(In_{0.5}Ga_{0.5})_{1+z/3}Se2$ compounds. *J. Solid State Chem.*, **183**, 2274, (2010).

[46] S.B. Zhang and S.-H. Wei. Reconstruction and energetics of the polar (112) and $(\bar{1}\bar{1}\bar{2})$ versus the nonpolar (220) surfaces of $CuInSe_2$. *Phys. Rev. B*, **65**, 081402, (2002).

[47] D. Liao and A. Rockett. Epitaxial growth of Cu(In,Ga)Se_2 on GaAs(110). *J. Appl. Phys.*, **91**, 1978, (2002).

[48] J. M. Merino, S. Mahanty, M. Leon, R. Diaz, F. Rueda, and J. L. Martin de Vidales. Structural characterization of $CuIn_2Se_{3.5}$, $CuIn_3Se_5$ and $CuIn_5Se_8$ compounds. *Thin Solid Films*, **361**, 70, (2000).

[49] T. Hanada, A. Yamana, Y. Nakamura, O. Nittono, and T. Wada. *Jpn. J. Appl. Phys.*, **36**, L1494, (1997).

[50] D. S. Su, W. Neumann, and M. Giersig. *Thin Solid Films*, **361**, 218, (2000).

[51] S. Nomura and S. Endo. *J. Phys. Chem. Solids*, **64**, 1891, (2003).

[52] M. Souilah, A. Lafond, N. Barreau, C. Guillot-Deudon, and J. Kessler. Evidence for a modified-stannite crystal structure in wide band gap Cu-poor $CuIn_{1-x}Ga_xSe_2$: Impact on the optical properties. *Appl. Phys. Lett.*, **92**, 241923, (2008).

[53] Sebastian Lehmann, David Fuertes Marrón, Michael Tovar, Yvonne Tomm, Christian Wolf, Susan Schorr, Thomas Schedel-Niedrig, Ernest Arushanov, and Martha Christina Lux-Steiner. A structural study on the $CuGaSe_2$-related copper-poor materials $CuGa_3Se_5$ and $CuGa_5Se_8$:thin-film vs. bulk material. *Phys. Status Solidi A*, **206**, 1009, (2009).

[54] Sebastian Lehmann, David Fuertes Marrón, M. León, R. Feyerherm, E. Dudzik, E. J. Friedrich, Michael Tovar, Yvonne Tomm, Christian Wolf, Susan Schorr, Thomas Schedel-Niedrig, Martha Christina Lux-Steiner, and J. M. Merino. Long-range structure of $Cu(In_xGa_{1-x})_3Se_5$. *J. Appl. Phys.*, **109**, 013518, (2011).

[55] I. V. Bodnar, A. A. Vaipolin, V. Yu. Rud, and Yu. V. Rud. Crystal Structure of $CuIn_3Se_5$ and $CuIn_5Se_8$ Ternary Compounds. *Technical Physics Letters*, **32**(12), 1003, (2006).

[56] A.V. Novoselova and V.B. Lazarev. *Physicochemical properties of Semiconductors.* Nauka, Moscow, (1979).

[57] L. Durán, C. Guerrero, E. Hernández, J.M. Delgado, J. Contreras, S.M. Wasim, and C.A. Durante Ricón. Structural, optical and electrical properties of $CuIn_5Se_8$ and $CuGa_5Se_8$. *J. Phys. Chem. Solids*, **64**, 1907, (2003).

[58] M. Born and R. Oppenheimer. Zur Quantentheorie der Molekeln. *Ann. Phys.*, **389**, 457, (1927).

[59] Robert G. Parr and Weitao Yang. *Density-Functional Theory of Atoms and Molecules.* Oxford University Press, (1989).

[60] D. M. Ceperley and B. J. Alder. Ground State of the Electron Gas by a Stochastic Method. *Phys. Rev. Lett.*, **45**, 566, (1980).

[61] Daan Frenkel and Berend Smit. *Understanding Molecular Simulation.* Academic Press, (2002).

[62] W. Zhang, J.R. Smith, and X.-G. Wang. Thermodynamics from ab initio computations. *Phys. Rev. B*, **70**, 024103, (2004).

[63] G.M. Torrie and J.P. Valleau. Nonphysical sampling distributions in Monte Carlo free-energy estimation: Umbrella sampling. *J. Comp. Phys.*, **23**, 187, (1977).

[64] Joseph E. Mayer and Elliott Montroll. Molecular Distribution. *J. Chem. Phys.*, **9**, 2, (1941).

[65] Ernst Ising. Beitrag zur Theorie des Ferromagnetismus. *Z. Phys. A: Hadrons Nucl.*, **31**, 253, (1925).

[66] A. van de Walle and G. Ceder. Automating First-Principles Phase Diagram Calculations. *J. of Phase Equilibria*, **23**, 348, (2002).

[67] A. van de Walle, M. Asta, and G. Ceder. The Alloy Theoretic Automated Toolkit: A User Guide. *CALPHAD Journal*, **26**, 539, (2002).

[68] X. Gonze, J.-M. Beuken, R. Caracas, F. Detraux, M. Fuchs, G.-M. Rignanese, L. Sindic, M. Verstraete, G. Zerah, F. Jollet, M. Torrent, A. Roy, M. Mikami, Ph. Ghosez, J.-Y. Raty, and D. C. Allan. First-principles computation of material properties: the ABINIT software project. *Computational Materials Science*, **25**, 478, (2002).

[69] X. Gonze, G.-M. Rignanese, M. Verstraete, J.-M. Beuken, Y. Pouillon, R. Caracas, F. Jollet, M. Torrent, G. Zerah, M. Mikami, Ph. Ghosez, M. Veithen, J.-Y. Raty, V. Olevano, F.Bruneval, L.Reining, R.Godby, G. Onida, D. R. Hamann, and D. C. Allan. A brief introduction to the ABINIT software package. *Zeit. Kristallogr*, **220**, 558, (2005).

[70] The ABINIT code is a common project of the Université Catholique de Louvain, Corning Incorporated, and other contributors (URL http://www.abinit.org).

[71] P. Blaha, K. Schwarz, G.K.H. Madsen, D. Kvasnicka, and J. Luitz. *Wien2k, An Augmented Plane Wave + Local Orbitals Program for Calculating Crystal Properties, (Karlheinz Schwarz, Techn. Universität Wien, Austria),*, (2001).

[72] N. Troullier and José Luís Martins. Efficient pseudopotentials for plane-wave calculations. *Phys. Rev. B*, **43**, 1993, (1991).

[73] John P. Perdew, Kieron Burke, and Matthias Ernzerhof. Generalized Gradient Approximation Made Simple. *Phys. Rev. Lett.*, **77**(18), 3865, (1996).

[74] Paolo Giannozzi, Stefano Baroni, Nicola Bonini, Matteo Calandra, Roberto Car, Carlo Cavazzoni, Davide Ceresoli, Guido L Chiarotti, Matteo Cococcioni, Ismaila Dabo, Andrea Dal Corso, Stefano de Gironcoli, Stefano Fabris, Guido Fratesi, Ralph Gebauer, Uwe Gerstmann, Christos Gougoussis, Anton Kokalj, Michele Lazzeri, Layla Martin-Samos, Nicola Marzari, Francesco Mauri, Riccardo Mazzarello, Stefano Paolini, Alfredo Pasquarello, Lorenzo Paulatto, Carlo Sbraccia, Sandro Scandolo, Gabriele Sclauzero, Ari P Seitsonen, Alexander Smogunov, Paolo Umari, and Renata M Wentzcovitch. QUANTUM ESPRESSO: a modular and open-source software project for quantum simulations of materials. *J.Phys.:Condens. Mater*, **21**, 395502, (2009).

[75] David Vanderbilt. Soft self-consistent pseudopotentials in a generalized eigenvalue formalism. *Phys. Rev. B*, **41**, 7892, (1990).

[76] Makoto Matsumoto and Takuji Nishimura. Mersenne twister. A 623-dimensionally equidistributed uniform pseudorandom number generator. *ACM Transactions on Modeling and Computer Simulation*, **8**, 3, (1998).

[77] Kurt Binder. Finite Size Scaling Analysis of Ising Model Block Distribution Functions. *Z. Phys. B: Condens. Matter*, **43**, 119, (1981).

[78] B. Fierro, F. Bachmann, and E.E. Vogel. Phase transition in 2D and 3D Ising model by time-series analysis. *Physica B*, **384**, 215, (2006).

[79] Christian D. R. Ludwig, Thomas Gruhn, Tanja Schilling, Peter Kratzer, Claudia Felser, and Johannes Windeln. Indium-Gallium Segregation in $CuIn_xGa_{1-x}Se_2$: An Ab Initio–Based Monte Carlo Study. *Phys. Rev. Lett.*, **105**, 025702, (2010).

[80] M. Belhadj, A. Tadjer, B. Abbar, Z. Bousahla, B. Bouhafs, and H. Aourag. Structural, electronic and optical calculations of Cu(In,Ga)Se_2 ternary chalcopyrites. *Phys. Status Solidi*, **241**, 2516, (2004).

[81] Philipp Haas, Fabien Tran, and Peter Blaha. Calculation of the lattice constant of solids with semilocal functionals. *Phys. Rev. B*, **79**, 085104, (2009).

[82] L. Gütay and G.H. Bauer. Non-uniformities of opto-electronic properties in Cu(In,Ga)Se_2 thin films and their influence on cell performance studied with confocal photoluminescence. In *IEEE Photov. Spec. Conf.*, (2009).

[83] L. Gütay and G.H. Bauer. Spectrally resolved photoluminescence studies on Cu(In,Ga)Se2 solar cells with lateral submicron resolution. *Thin Solid Films*, **515**, 6212, (2007).

[84] J. Haarstrich, H. Metzner, M. Oertel, C. Ronning, T. Rissom, C. A. Kaufmann, T. Unold, H.-W. Schock, J. Windeln, W. Mannstadt, and E. Rudigier-Voigt. Increased homogeneity and open-circuit voltage of Cu(In,Ga)Se2 due to higher deposition temperature. *Solar Energy Materials and Solar Cells*, **95**, 1028, (2011).

[85] Christian D. R. Ludwig, Thomas Gruhn, Claudia Felser, and Johannes Windeln. Defect structures in $CuInSe_2$: A combination of Monte Carlo

simulations and density functional theory. *Phys. Rev. B*, **83**, 174112, (2011).

[86] B. Widom. Some topics in the theory of fluids. *J. Chem. Phys.*, **39**, 2802, (1963).

[87] R. Herberholz, H.W. Schock, U. Rau, J.H. Werner, T. Haalboom, T. Gödecke, F. Ernst, C. Beilharz, K.W. Benz, and D. Cahen. New Aspects of Phase Segregation and Junction Formation in $CuInSe_2$. In *26th PVSC, Anaheim, CA*, (1997).

[88] T.Goedecke, T. Haalboom, and F. Ernst. Phase Equilibria of Cu-In-Se I. Stable States and Nonequilibrium States of the In_2Se_3-Cu_2Se Subsystem. *Z. Metallkd.*, **91**, 622, (2000).

[89] Y. Yan, R. Noufi, K.M. Jones, K. Ramanathan, M.M. Al-Jassim, and B.J. Stanbery. Chemical fluctuation-induced nanodomains in Cu(In,Ga)Se2 films. *Appl. Phys. Lett.*, **87**, 121904, (2005).

[90] Teodor K. Todorov, Kathleen B. Reuter, and David B. Mitzi. High-Efficiency Solar Cell with Earth-Abundant Liquid-Processed Absorber. *Advanced Materials*, **22**, E156, (2010).

[91] Ioan Kiss and Thomas Gruhn. *Annual report of the comCIGS project: JGU Mainz*, (2010).

[92] J. Windeln, H.-W. Schock, C. Felser, H. Metzner, W. Mannstadt, R. Klenk, T. Gruhn, C. Kaufmann, E. Rudigier-Voigt, B. Speit, M. Haag, T. Rissom, D. Kieven, C. Ludwig, J. Haarstrich, and M. Oertel. comCIGS - Integrative Framework of Experimental and Virtual Lab. In *24th Eur. Photov. Solar Energy Conf.*, page 2443, (2009).

[93] Thorsten Rissom, Christian A. Kaufmann, and Hans-Werner Schock. *Annual report of the comCIGS project: HZ Berlin*, (2010).